

DIPLOMARBEIT

Simulation and optimization of a proton computed tomography setup at MedAustron

Supervisors:

Univ.Prof. civ.ing. tekn.lic. tekn.dr. Lembit Sihver
Dipl.-Ing. Dr.techn. Albert Hirtl

Atominstitut
Technische Universität Wien

conducted by:

Felix K. V. Ulrich-Pur BSc.
felix.ulrich-pur@tuwien.ac.at
Kremsergasse 5/1/7
A-1130 Wien

Technische Physik
E066 461

Vienna, June 13, 2018

Abstract

Proton therapy is a precise method to treat deep-seated tumours, using accelerator-produced proton beams. However, for valid predictions of the proton range and dose deposition due to the depth-dose characteristics of the ion beam, it is necessary to know the stopping power inside the patient. One method to achieve this goal is Proton Computed Tomography (pCT), which measures the energy loss of protons at the plateau of the Bragg curve. The main advantage of pCT is that the same type of particles used for therapy is used to measure the stopping power distribution.

A pCT setup basically consists of a tracker, which should be able to reconstruct the particle trajectory through the patient and a calorimeter to measure the deposited energy in the patient.

The tracker should be able to achieve single particle counting, which requires low particle fluxes. Therefore three different particle flux reduction methods, provided by MedAustron had to be tested experimentally. For this purpose a VME based particle counting and trigger system (PCTS) was developed within this thesis. With this PCTS system, fluxes down to 1×10^4 p/s were measured.

In order to calculate the stopping power in the patient correctly, the path of the traversing proton has to be estimated. For this purpose a tracking telescope, consisting of four double-sided silicon strip detectors was designed, simulated with Geant4, optimized and tested experimentally. The scattering power of a plastic phantom, mounted on an in-house made rotary table, was measured and compared to the Geant4 Monte Carlo simulation.

The results showed that a functioning beam telescope, which is able to perform particle tracking could be installed. Also the experimentally obtained distorted beam profiles showed similarities to the simulated beam profiles.

This tracker combined with a suitable calorimeter would form together a full pCT setup.

Zusammenfassung

Protonen Therapie verwendet hochenergetische Protonen um tiefsitzende Tumore zu bestrahlen. Diese Bestrahlungstherapie verlangt die Kenntnis des Bremsvermögens der Protonen im Patienten um eine genaue Vorhersage der Reichweite und der deponierten Dosis der Protonen im Patienten zu treffen. Proton Computed Tomography (pCT) ist eine präzise Methode zur Bestimmung des Bremsvermögens für Ionentherapie. Diese Methode verwendet im Gegensatz zu herkömmlichen Methoden den Ionenstrahl direkt um das Bremsvermögen zu bestimmen.

Ein pCT Versuchsaufbau besteht aus zwei Komponenten. Eine Komponente ist ein Tracker, mit dem der Pfad des Ions durch den Patienten bestimmt werden kann. Zusätzlich wird auch ein Kalorimeter gebraucht um die abgegebene Energie der Teilchen im Patienten zu bestimmen.

Damit der Tracker die Einzelpfade der Teilchen aufzeichnen können, sollten die Teilchenraten niedrig gehalten werden. Aus diesem Grund sind drei neue Teilchenratenreduktionsmethoden am MedAustron entwickelt worden. Diese neuen Raten sind mit einem particle counting und trigger system (PCTS) analysiert worden. Es basiert auf VME Logik und wurde im Rahmen dieser Arbeit entwickelt. Teilchenraten bis zu 1×10^4 p/s konnten gemessen werden.

Um das Bremsvermögen im Patienten korrekt abzuschätzen muss der Pfad der Teilchen durch den Patienten bekannt sein. Deswegen wurde im Rahmen dieser Arbeit ein Tracking-Teleskop, welches aus vier doppelseitigen Silizium Streifendetektoren besteht, designed, in Geant4 simuliert und experimentell getestet. Das fertige Tracking setup wurde verwendet um die Streuung von Protonen an zwei verschiedenen Plastikphantomen zu messen. Die Phantome konnten über einen selbst entwickelten Drehtisch gedreht werden. Die Ergebnisse der Streuversuche wurden mit einer Monte Carlo Simulation verglichen. Die Ergebnisse dieser Versuche haben gezeigt, dass das Beam Teleskop als Tracker für pCT geeignet ist. Auch die experimentell bestimmte Streuverteilungen der Protonen zeigen Ähnlichkeiten mit der in Geant4 simulierten Streuverteilungen. Für ein komplettes pCT Setup müsste man ein geeignetes Kalorimeter mit dem Tracker verbinden.

Contents

1	Introduction	4
2	Physical background	7
2.1	Particle therapy	7
2.2	Principles of proton Computed Tomography	8
2.3	Interaction of heavy charged particles with matter	11
2.4	Scintillators	14
2.5	Gaseous radiation detectors	17
2.6	Silicon strip detectors	18
2.7	Monte Carlo method for particle transport	23
3	Materials and methods	25
3.1	The MedAustron particle accelerator	25
3.2	VME based particle counting and trigger system (PCTS)	29
3.3	Plateau Curve measurement	34
3.4	Beam geometry measurements	37
3.5	Particle flux measurements	38
3.6	Beam telescope setup for pCT	39
4	Results and discussion	49
4.1	Particle flux reduction	49
4.2	Beam telescope for pCT	54
5	Conclusion and outlook	65
6	Acknowledgements	68
	Appendix	69
	List of Figures	70
	List of Tables	72
	List of Abbreviations	73
	References	74
	Beam telescope measurements	78

1 Introduction

Proton radiotherapy has become an important part of cancer treatment in the last 60 years. The first patient was treated with protons in 1954 at the Berkley Radiation Laboratory and since then the number of proton therapy centers has increased. Using accelerator-produced beams of protons to treat deep-seated tumors in humans, provides a precise form of radiotherapy.

The main advantage of proton radiotherapy over conventional radiotherapy is sparing normal tissue during treatment due to the depth-dose characteristics of the proton beam, exhibiting the so called Bragg-peak close to the end of the ion range (Figure 1). But also other ions, such as carbon and helium can be used since they have similar depth-dose characteristics as protons.

However, some facilities, such as MedAustron, are capable of using other ions like carbon or helium. At the moment, MedAustron uses 62.4-252.7 MeV protons for radiotherapy and will be able to use protons up to 800 MeV and carbon ions up to 400 MeV/u by the end of 2019.

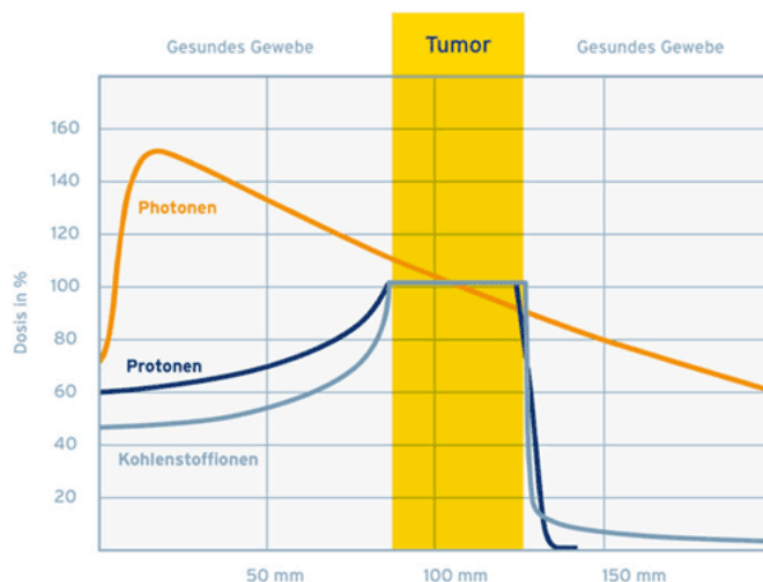


Figure 1: Depth-dose profile of photons vs. ions [1]

In contrast, conventional radiotherapy uses photons to destroy cancerous tissue. As can be seen in Figure 1, the maximum dose per penetration depth for photons is deposited near the surface of the target tissue. Since the deposited dose can not be as localized as for ion radiotherapy, unwanted regions of the patient could also receive a relatively high dose. Especially for cancers surrounding vital parts of the human body, such as the brain stem or spinal chord, conventional radiotherapy would entail a higher risk to the patient.

Therefore, the minimal exit dose of ions allows to precisely treat those types of cancer and keeps the risk of short- and long-term side effects as low as possible [2].

However, the precise methods of ion beam therapy require accurate and precise verification procedures, assuring that the patient position during treatment is correct and that

the prediction of the proton range and dose calculations are valid.

One method to achieve this goal is proton computed tomography (pCT), which uses the energy loss of the protons at the plateau of the Bragg curve. With this method, a three-dimensional map of the stopping power (energy deposition per unit path length) can be reconstructed from measurements directly. The correct knowledge of the stopping power within the patient is crucial for a precise treatment planning.

Over the last 50 years research has been done on proton computed radiography and tomography, but no pCT setup has been used for ion therapy yet [3]. This might be due to the fact that pCT setups need accelerators which are capable of producing protons with energies large enough to fully traverse the patient (230 MeV protons have a 33 cm range in water [3]). Another fact is that the proton path is not straight due to multiple coulomb scattering, which influences the image quality. In order to solve this problem, the most likely path reconstruction technique was developed by [4] and has been standardly used by the pCT community.

Because of the increasing number of suitable particle accelerators for pCT and the ongoing progress in the development of better particle detectors and image reconstruction techniques, the interest for pCT has grown over the last years. First promising pCT images of a human head phantom were taken by [5]. However, in order to develop a suitable pCT setup for routine operation, many influencing factors of the detectors and reconstruction techniques on pCT have to be analyzed.

Within this master thesis several parameters which influence the quality of proton Computed Tomography were investigated and optimized at MedAustron. This was done in two parts:

The detectors used for pCT require lower particle rates ($10^5 - 10^6 \text{ s}^{-1}$) than those which are available at MedAustron at the moment (10^9 s^{-1}). Therefore new different particle flux reduction methods had to be tested experimentally at MedAustron. For this purpose a beam monitor, consisting of plastic scintillators and a FPGA based VME logic was developed and optimized. This beam monitor was designed in a way that it can also be used as a trigger unit for other devices. In addition, the effect of the different flux reduction methods on the beam geometry was studied.

In order to calculate the stopping power in the patient correctly, the path of the traversing proton has to be estimated. For this purpose, the second part of this thesis discusses the setup of a tracking telescope, consisting of four double-sided silicon strip detectors. This beam telescope was designed, simulated with Geant4, optimized and tested experimentally. The scattering power of two plastic phantoms, mounted on a self made, remote controllable rotary table, was measured and compared to a Monte Carlo simulation.

2 Physical background

2.1 Particle therapy

The main goal of particle therapy is to control the growth and to kill cancerous cells by irreversibly damaging their DNA. This DNA damage occurs whenever an ionizing particle travels through tissue. The ionizing particle transfers part of its kinetic energy to the traversed material via ionization and excitation of the target tissue. The amount of energy deposited per unit path length can be described by the Bethe-Bloch equation.

2.1.1 Bethe-Bloch equation

The Bethe Bloch formula describes the mean energy loss per distance of fast, charged particles (protons, α -particles and heavy ions), which travel through matter. This equation reads as follows [6]

$$-\left\langle \frac{dE}{dx} \right\rangle = \frac{4\pi}{m_e c^2} \cdot \frac{\rho_{el} Z^2}{\beta^2} \cdot \left(\frac{e^2}{4\pi\epsilon_0} \right)^2 \cdot \left[\ln \left(\frac{2m_e c^2 \beta^2}{I_{mat} \cdot (1 - \beta^2)} \right) - \beta^2 - \frac{\delta}{2} - \frac{C}{Z} \right]. \quad (2.1)$$

In this equation m_e is the mass of an electron, c is the speed of light, Z the charge of the traversed material, ρ_{el} is the electron density, I_{mat} is the excitation potential of the material, β is the ratio of the velocity of the particle and the speed of light and ϵ_0 is the vacuum permittivity. The shell correction term $\frac{C}{Z}$ and the correction term for ultrarelativistic charged particles $\left(\frac{\delta}{2}\right)$ are also shown.

As can be seen in equation (2.1), the energy loss of the traveling charged particle depends on its velocity ($v = \beta \cdot c$). For small energies, the energy loss is inversely proportional to the square of the velocity of the particle ($\frac{dE}{dx} \propto \frac{1}{v^2}$). This leads to the so called Bragg Peak where a large amount of the energy of the particle is deposited at a certain range, where the particles are almost at rest (Figure 1).

The quotient of $-\frac{dE}{dx}$ is also called the linear stopping power, which is proportional to the electron density ρ_{el} . Since ρ_{el} depends on the density ρ of the traversed material, the linear stopping power is often divided by ρ , which is then called the mass stopping power $S = -\frac{dE}{dx} \cdot \frac{1}{\rho}$. In Figure 2, the mass stopping power for a plastic scintillator is shown:

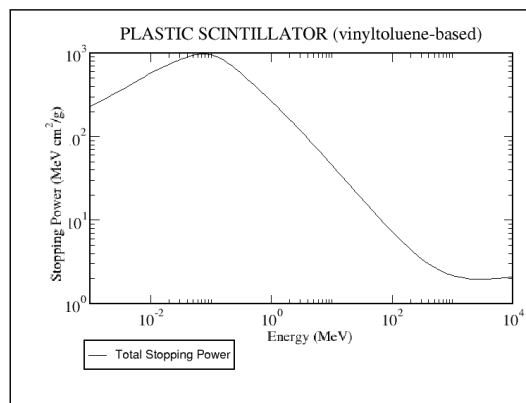


Figure 2: Total stopping power for protons in plastic scintillators [7]

2.1.2 Particle range

According to the Bethe Bloch formula (2.1), protons travelling through matter lose energy in many small steps dx , until they have lost all their energy. In order to describe the distance to this point the particle range has to be defined. This can be done by the continuous slowing down approximation (CSDA), which reads as follows

$$R_{\text{CSDA}} = \int_0^L dx = \int_{E_0}^0 \left(-\frac{dE}{dx} \right)^{-1} dE = \int_{E_0}^0 \frac{1}{S(E)} dE \quad (2.2)$$

As can be seen in equation (2.2), the particle range depends on the inverse stopping power of the traversed medium and on the particle's initial energy E_0 . However, each proton will not stop at the same CSDA range because of statistical fluctuations ($\approx 1\%$ of the CSDA range [6]). The range is smeared out (Figure 3) due to nuclear reactions in the energy-loss process (*range straggling*).

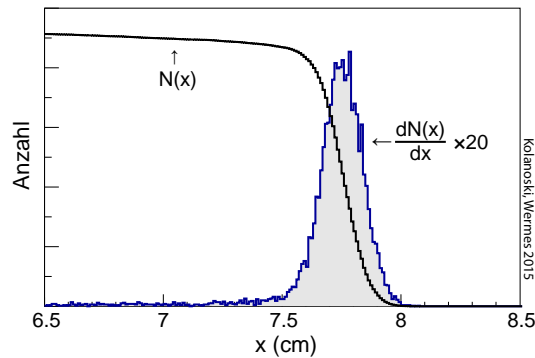


Figure 3: Geant4 Simulation of 100 MeV protons travelling through water [6]

2.2 Principles of proton Computed Tomography

For particle therapy it is important to know the stopping power at any position (x, y, z) of the treated volume of the patient in order to calculate the particle range in this tissue correctly. Any small deviation from the correct stopping power could shift the Bragg peak slightly in space which could lead to unwanted irradiation of healthy tissue.

2.2.1 Treatment planning based on computed tomography

Conventional treatment planning uses computed tomography (CT) images, which are based on the attenuation of X-ray beams in the traversed medium. The attenuation of photons in matter can be described by the Beer-Lambert law:

$$I(z) = I_0 \cdot e^{-\mu_{\text{mat}} z} \quad (2.3)$$

μ_{mat} is the linear attenuation coefficient and depends on the traversed material. In order to get a CT image, a 3D map of the linear attenuation coefficients of the target material has to be obtained and normalized to water and air. The conversion from the attenuation coefficient to the normalized attenuation coefficient (in Hounsfield units HU) is shown in equation (2.4)

$$HU = 1000 \cdot \frac{\mu_{\text{mat}} - \mu_{\text{water}}}{\mu_{\text{water}} - \mu_{\text{air}}}. \quad (2.4)$$

For conventional radiotherapy based on photons, the normalized attenuation coefficients of the target are used for treatment planning and lead to accurate results [8].

However, for ion therapy the stopping power of ions in matter has to be known. Therefore, the HU of the target material, which are based on interactions of photons with matter, have to be translated into electron densities [9]. The stopping power of ions in the target material can then be obtained by inserting the electron densities in the Bethe-Bloch equation (2.1). Because of the different interaction mechanisms for photons and heavy ions, this procedure leads to range uncertainties of several mm [10], resulting in unwanted dose deposition outside of the tumor region.

2.2.2 Treatment planning based on proton computed tomography

A pCT system uses protons to measure and calculate the stopping power directly. The basic principles for the calculation of the stopping power for pCT can be found in [11] and is summarized in the following section.

According to section 2.1.1, the Bethe-Bloch equation describes the linear energy transfer per path length dl for fast, charged particles. The linear stopping power $S(x, y, E)$ for a proton with energy E at position (x, y) was then defined according to

$$-dE = S(x, y, E)dl. \quad (2.5)$$

By multiplying equation (2.5) by the mass stopping power $\frac{S}{\rho}(x, y, E_0) = -\frac{dE}{dx} \cdot \frac{1}{\rho}$ for a certain reference energy E_0 , for which the stopping power needs to be calculated and extending the right side of the equation by $\frac{\rho(x, y)}{\rho(x, y)}$, one obtains

$$-\frac{S}{\rho}(x, y, E_0)dE = \frac{S}{\rho}(x, y, E_0)\frac{S}{\rho}(x, y, E)\rho(x, y)dl. \quad (2.6)$$

Equation (2.6) can then be divided by the mass stopping power $\frac{S}{\rho}(x, y, E)$:

$$-\frac{\frac{S}{\rho}(x, y, E_0)}{\frac{S}{\rho}(x, y, E)}dE = S(x, y, E_0)dl. \quad (2.7)$$

The ratio of the mass stopping powers on the left side of equation (2.7) was found to only have a negligibly small dependence on the density ρ ($< 6 \cdot 10^{-3}$ [11]). Therefore it can be replaced by the known stopping power ratio for water [12]

$$-\left[\frac{S}{\rho}(H_2O)\right]_E^{E_0} = S(x, y, E_0)dl, \quad (2.8)$$

$$\text{with } \left[\frac{S}{\rho}(H_2O)\right]_E^{E_0} \cong \left[\frac{S}{\rho}(x, y)\right]_E^{E_0} = \frac{\frac{S}{\rho}(x, y, E_0)}{\frac{S}{\rho}(x, y, E)}. \quad (2.9)$$

Equation (2.8) can then be integrated over the whole proton path through the phantom. Since protons do not pass straight through the phantom, due to multiple Coulomb

scattering, this path has to be estimated. One possibility is the most likely path (MLP [4]) estimation.

$$-\int_{E_{\text{in}}}^{E_{\text{out}}} \left[\frac{S}{\rho}(H_2O) \right]_E^{E_0} dE = \int_{\text{path}} S(x, y, E_0) dl. \quad (2.10)$$

In equation (2.10), E_{in} and E_{out} are the energies of the proton entering and exiting the phantom. E_{in} is given by the accelerator and the materials in the beam line in front of the phantom and E_{out} can be measured with a calorimeter. This equation can then be discretized, by dividing the phantom in N pixels and is given by

$$p_i \equiv -\int_{E_{\text{in}}}^{E_{\text{out}}} \left[\frac{S}{\rho}(H_2O) \right]_E^{E_0} dE = \sum_{j=i}^N w_{ij} S_j(E_0). \quad (2.11)$$

This leads to a set of linear equations (equation (2.11)) with N_p linear equations with N unknowns. N_p is the number of protons passing the phantom, w_{ij} is the path length of proton i in pixel j and $S_j(E_0)$ is the stopping power for a proton with energy E_0 in pixel j .

However, since equation (2.11) contains a large set of equations ($N_p \times N$), iterative, numerical reconstruction methods, such as the algebraic reconstruction technique (ART) have to be used to solve a system of linear equations of the form $Ax = b$. The iteration is performed by

$$x^{k+1} = x^k + \lambda^k \cdot \frac{b_i - \langle a_i, x^k \rangle}{\|a_i\|^2} a_i^T. \quad (2.12)$$

In equation (2.12), x^k is the “k-th” iteration of the solution vector x , λ is an relaxation constant, a_i is the “i-th” row of the coefficient matrix a_{ij} ($\triangleq w_{ij}$) and $b_i \triangleq p_i$. The ART method uses an estimate of the solution $S_j(E_0) \triangleq x^{k=0}$ and iteratively projects it on the set of equation (2.11) which should converge to the real solution eventually [13].

2.2.3 Schematic pCT setup

In order to solve equation (2.11) the path of the proton traveling through the phantom and the energy of the proton entering and exiting the phantom have to be measured experimentally.

The path of the proton can be estimated using the MLP approach. This method requires the knowledge of the entry and exit position of the proton as well as the entry and exit momentum of the proton. This can be measured with two beam telescopes. One beam telescope is mounted in front of the patient and the other one closely behind the patient. Each of the telescopes should consist of at least 2 position sensitive detectors, which measure the x and y coordinates of the traversing particle.

A calorimeter to measure the residual energy E_{out} of the proton after passing the patient has to be mounted behind the last beam telescope. The energy of the proton entering the patient is given by the accelerator.

A schematic drawing of a whole pCT setup, as described above, is depicted in Figure 4.

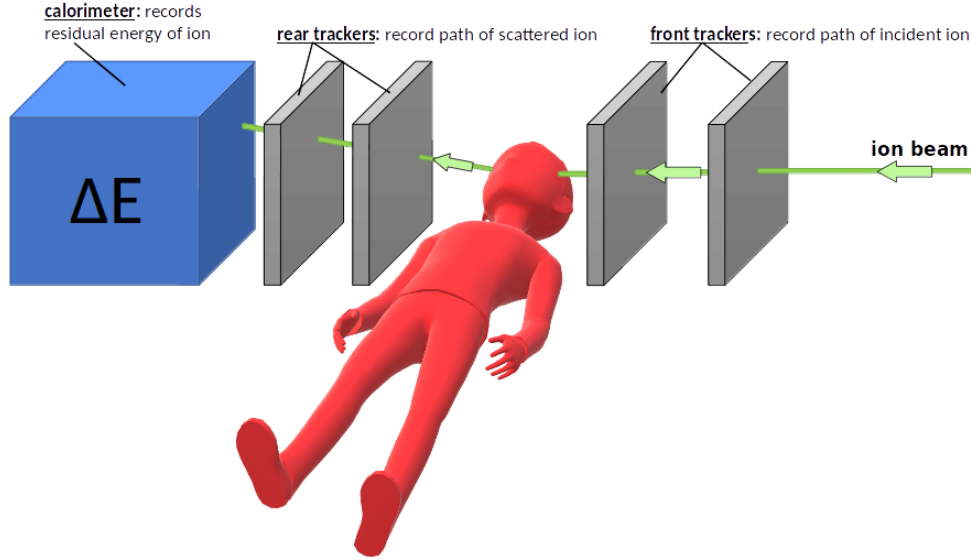


Figure 4: Setup of a proton computed tomography

2.3 Interaction of heavy charged particles with matter

When heavy charged particles travel through a detector they transfer energy to the detector component through various processes. To get a good understanding of the physics behind the particle detectors needed for pCT, the main interactions of charged particles with matter will be discussed briefly in this section.

2.3.1 Main interactions

Heavy charged particles mainly lose energy and get deflected by Coulomb interactions with the traversed material. This happens predominantly through two different processes. The charged particle can either undergo an inelastic collision with the atomic electrons of the target material or it can scatter elastically from the nuclei (Figure 5).

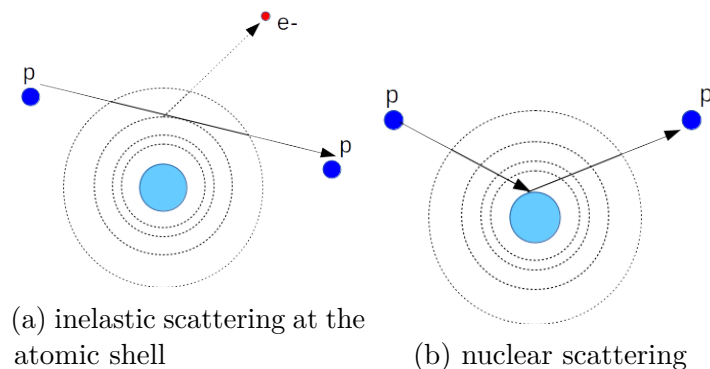


Figure 5: Interaction of protons with matter

2.3.2 Inelastic scattering at the atomic shell

Within an inelastic collision at the atomic electron (Figure 5a), the charged particle transfers a small amount of its kinetic energy to the electrons of the atomic shell, causing

excitation or ionization of the target atom. Since the energy loss per interaction is small, the direction of the proton will not change significantly. Nonetheless, this interaction is mainly responsible for the total energy loss in the target material, because of the high occurrence of inelastic collisions.

The energy of some secondary electrons can be sufficiently high to ionize other particles. Those secondary ionizing electrons are then called δ -electrons.

2.3.3 Elastic nuclear scattering

In addition to inelastic collisions with the atomic electrons, protons passing through matter undergo repeated elastic Coulomb scattering with the nuclei (Figure 5b), but with a smaller probability than inelastic collisions with the atomic electrons.

Usually the mass of the target nucleus is greater than the mass of the incoming proton so that the energy loss is negligible, but the direction of the proton can change significantly in each collision. However, even if the change of the trajectory of every elastic collision is small, the sum of all the collisions result in a zig-zag path leading to a scattering angle θ (Figure 6).

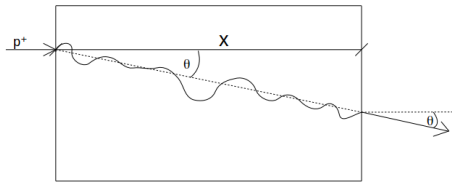


Figure 6: Zig-zag path of a proton through a material of thickness x , undergoing multiple Coulomb scattering with a total scattering angle θ

Single Coulomb Scattering:

If the thickness x of the medium is very small and Coulomb scattering occurs only once, one can describe the process by Rutherford's equation [14], which reads as follows

$$\frac{d\sigma}{d\Omega} = \left(\frac{m_e c}{\beta p} \right)^2 \cdot \frac{Z_1^2 Z_2^2 r_e^2}{\sin^4(\theta/2)}. \quad (2.13)$$

This formula for single Coulomb scattering (2.13) depends on the differential cross section $\frac{d\sigma}{d\Omega}$, which is an indicator for the probability of an interaction happening for a certain angle Θ . It depends on the mass of the electron m_e , the electron radius r_e , the charge of the incident ion Z_1 , the charge of the target nucleus Z_2 , the ratio $\beta = \frac{v}{c}$, with v being the velocity of the ion and c the speed of light and p being the momentum of the incident ion.

Multiple Coulomb Scattering (MCS):

For an increasing number of Coulomb scatterings, but still under a few tens of interactions (< 20), it can be described by *Plural Coulomb Scattering*. This is difficult to model and will not be described here, but details can be found in [15].

However if the thickness is relatively large, so that a large number of elastic Coulomb scatterings occur, the situation can be described by Multiple Coulomb Scattering. A complete analytical theory of MCS was proposed by Molière [16]. His theory is based on single scattering with a small deflection angle approximation ($\sin(\theta) \approx \theta$).

The resulting angular distribution for MCS according to Molière can be approximated as a Gaussian distribution for small net deflection angles and behaves like Rutherford scattering at large angles ($\propto \frac{1}{\sin^4(\theta/2)}$) [16]. The Gaussian approximation for small angles reads as follows

$$P(\theta)d\Omega = \frac{1}{2\pi\theta_0^2} \exp\left[-\frac{\theta^2}{2\theta_0^2}\right] d\Omega, \quad (2.14)$$

$$\text{with } \theta_0 = \frac{13.6 \text{ MeV}}{\beta pc} Z \sqrt{\frac{x}{X_0}} \left[1 + 0.038 \ln\left(\frac{x}{X_0}\right)\right]. \quad (2.15)$$

The angle θ_0 in equation (2.15), which corresponds to the standard deviation of this Gaussian distribution, was introduced by Highland [17]. In this equation, x is the thickness of the material and X_0 is the radiation length of the material, which is a material constant. Z is the charge of the target material.

The cumulative effect of all the small angle scatterings is a net deflection from the original particle direction. But Molière's theory does not show the spatial displacement of the particle, it only gives the scattering angle distribution. In order to get the lateral displacement and the true path length one has to consider Lewis theory [18] which is a solution of the diffusion equation for MCS. The MCS model used in GEANT4 [19] uses the Lewis theory to simulate the transport of charged particles.

2.3.4 Inelastic nuclear reaction

An inelastic collision is an interaction between two particles where the total kinetic energy of them is not conserved. In an inelastic nuclear reaction, the incident proton interacts with the target nucleus. This excites the nucleus which subsequently decays by emitting nucleons or radiation. The target nucleus, after emitting a large number of particles is called target fragment. This heavy residue has a range of a few μm and is low energetic. If the incident particle collides with one single nucleon and one of the two partners leaves the nucleus without interfering with the other nucleons, the interaction can be referred to as a "direct knock-out". However, inelastic nuclear interactions are less frequent.

2.3.5 Cherenkov radiation

Whenever a charged particle travels in a medium faster than the speed of light in that medium, Cherenkov radiation occurs. This is due to the fact that the electric field of the charged particle polarises the medium and the medium depolarises when the particle has passed. This change of polarisation in the medium causes electromagnetic perturbances in the medium which propagate with the speed of light. If the particle travels faster than the speed of light in this medium, those perturbances add up together in one wave front. The angle of this Cherenkov radiation depends on the particle speed and the speed of light in the medium.

2.3.6 Bremsstrahlung

Bremsstrahlung occurs whenever a charged particle is decelerated. The lost kinetic energy is converted into photons.

2.4 Scintillators

A scintillator is a luminescent material which emits photons after being excited by ionizing radiation. It is commonly used for calorimetry or as a particle counter in particle physics experiments.

2.4.1 Luminescence

Luminescence describes the emission of photons by a substance after energy absorption. Depending on the time delay of the emission, luminescence can be classified into two subtypes. When a photon is emitted relatively promptly after the substance has absorbed energy (\sim ns), the process is called fluorescence.

When the molecule or electron gets excited, it can also return to a state of lower energy, which is, due to the selection rule of electromagnetic transitions, a relatively long-lived excited state (\sim ms – h). Subsequently, a photon is emitted when the molecule or electron returns to a lower energy level than the metastable state. This process is called phosphorescence.

2.4.2 Scintillating material

Depending on the scintillating material, the mechanisms which generate light differ and can be divided in three different types of scintillators:

- I) **Inorganic Scintillator:** The efficiency of luminescent emission in inorganic crystals is drastically improved by adding additional energy levels in the band gap of the crystal. This is done by adding impurity atoms (activators). Those scintillators are rather slow compared to gaseous or organic scintillators, but their light yield is often linear to the absorbed energy. Therefore those scintillators can be used as calorimeters.
- II) **Organic Scintillator:** Organic scintillators can be subdivided into organic crystals, plastic scintillators or organic fluids. Their light yield often cannot be approximated linearly to the absorbed energy, but they are relatively fast (\leq ns, or few ns). Because of this, those scintillators are often used as particle counters, or as a trigger.
- III) **Gaseous Scintillator:** Mostly noble gases, such as helium, xenon or argon are used for gaseous scintillators, but also nitrogen is used. The scintillation process is due to the de-excitation of the single atoms. The emitted light is mostly in the UV-region, which many photomultipliers are not responding well to. Therefore additional wavelength shifter, which absorb the emitted light of the scintillator and re-emit light of a lower frequency (Stokes shift) have to be used.

Since during this thesis only plastic scintillators were used, only those will be discussed in detail.

2.4.3 Plastic scintillator

A plastic scintillator is an organic material which consists of aromatic hydrocarbon compounds (benzene ring structure). These are hydrocarbons with σ -bonds and delocalized π -electrons (Figure 7a). Luminescence is due to electron transitions from the π -orbitals [6].

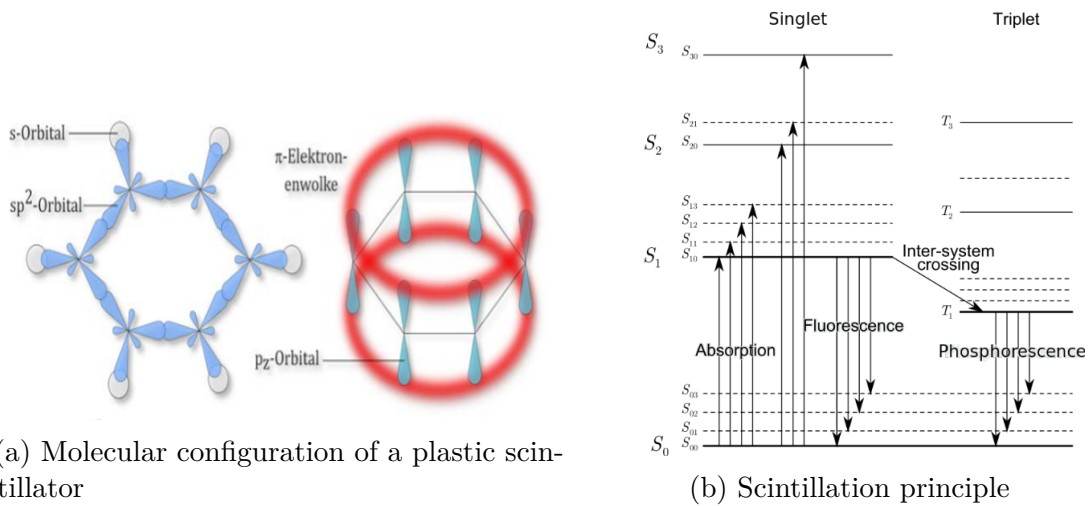


Figure 7: Electron configuration of a plastic scintillator

In Figure 7b, the energy levels of the π -electrons in a singlet (spin = 0) and a triplet (spin = 1) configuration are depicted. The main energy levels $S_0, S_1, \dots, T_1, \dots$ are split into vibrational energy levels $S_{00}, S_{01}, \dots, S_{10}, \dots$. Transitions from higher vibrational energy levels S_{ij} to the ground level of the same main energy level S_{i0} are non-radiative and only take ps. Subsequent transitions to the ground states of the main energy level occur in ns and a photon is emitted (fluorescence).

Transitions from excited triplet states to the ground triplet state, which is metastable, are non-radiative. Also according to the selection rule of electromagnetic transitions, transitions from the singlet to the triplet state are forbidden.

However, with a low probability, non-radiative intersystem crossing occurs. This means that mostly two triplet ground states interact and decay to an excited singlet, a singlet ground state and phonons ($T_0 + T_0 \rightarrow S_{10} + S_{00} + \text{phonons}$). Since the triplet states are metastable, the subsequent transitions to the ground state ($S_{10} \rightarrow S_{00}$) by emitting a photon are in the range of ms (phosphorescence).

2.4.4 Stokes shift

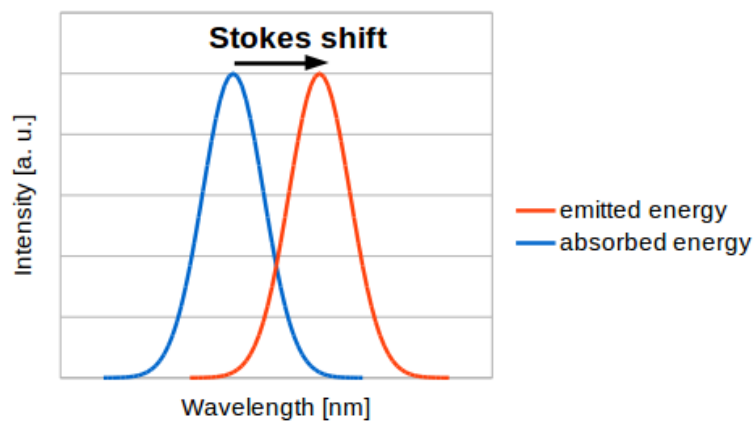


Figure 8: Stokes Shift

The energy of the emitted photon is smaller or equal to the absorbed energy. This

so called “Stokes shift” is based on non-radiative transitions from higher vibrational energy levels to the ground state of the same main energy level. This means that part of the absorbed energy is transferred into vibrational energy of the molecule. Therefore, the energy of the emitted photon is decreased which is depicted in Figure 8.

2.4.5 Scintillator detector setup

In order to use a scintillator as a detector, the light produced in the scintillator has to be converted into an electrical signal. A schematic drawing of such a scintillator setup is shown in Figure 9.

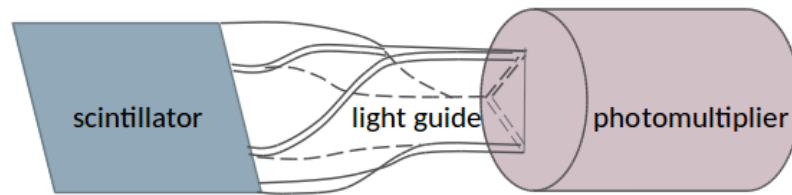


Figure 9: Scintillator setup

A scintillator detector setup mainly consists of three parts:

- **scintillator:** converts ionizing radiation into light
- **light guide:** couples light from the scintillator to the photocathode of the photomultiplier (PMT)
- **photomultiplier:** converts photons into electrons and amplifies the electric signal

Sometimes the geometry of the photocathode of the PMT differs from the geometry of the scintillator. Therefore, a light guide, usually made of plexiglas, is used to couple the light via total reflection from the scintillator to the PMT.

In order to ensure the best light collection, the light guide and the scintillator are coupled via optical grease, which should match the refractive index of the scintillator. In addition the scintillator and the light guide have to be covered with a reflector. For this purpose doubled sided optical duct tape is used, which should have a lower refractive index than the scintillator.

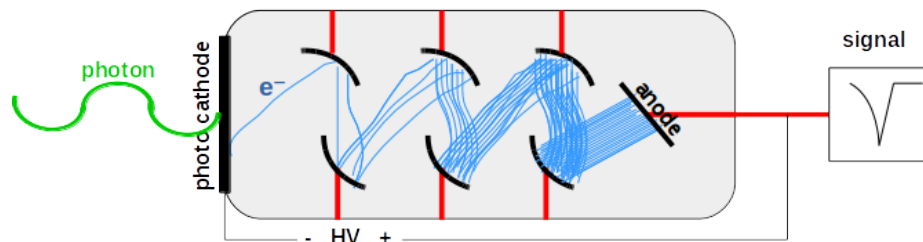


Figure 10: Photomultiplier

As can be seen in Figure 10, when the photon hits the photocathode, an electron is knocked out due to the photoeffect. This electron gets accelerated towards the first dynode via high voltage. A dynode is an electrode which multiplies the incoming electrons through secondary emission. Therefore, after hitting several dynodes, the number of electrons which enter the anode at the very end of the PMT has multiplied significantly. This resulting signal can then be amplified and analysed.

2.5 Gaseous radiation detectors

A gaseous radiation detector is a gas-filled detector, which produces a measurable electric current when it interacts with ionizing radiation. Depending on its operation mode, such a detector can be used for beam monitoring or position detection.

Those gaseous detectors basically consist of two electrodes between which a voltage is applied. This voltage difference sets up an electric field through the gaseous detector. Whenever ionizing, charged particles travel through such a detector, they can ionize the atoms in the gas. This produces electron hole pairs which then drift to the electrodes according to the polarity of the applied electric field. This signal can then be amplified and measured.

The arrangement of the two electrodes may differ for different detectors, however the basic principle of a gaseous detector stays the same. A schematic drawing of a gaseous detector is shown in Figure 11:

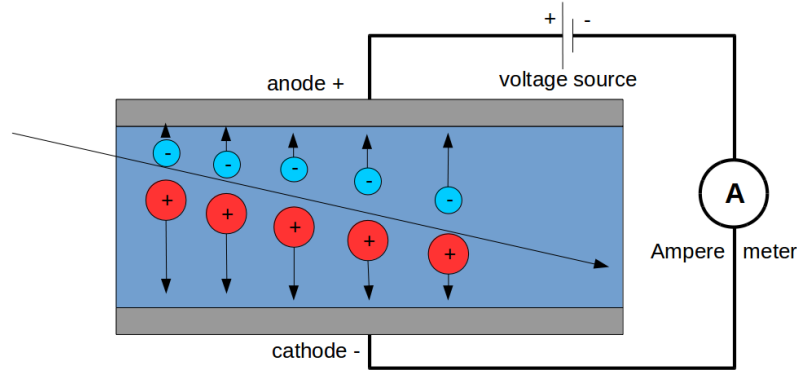


Figure 11: Operation principle of a gaseous detector

2.5.1 Operational modes

Depending on the applied voltage, the gaseous detector can be used in different operational modes (different output signals). The three most important ones are the ionization chamber, the proportional chamber and the Geiger-Müller counter (Figure 12).

If the applied electric field is high enough to cause secondary ionization, the additional electrons gain enough energy through acceleration, so that they can ionize other gas atoms. This leads to an avalanche like amplification of the primary signal.

Below a threshold such amplification does not take place. This operational mode can then be referred to as “ionization chamber”. The resulting signal from the produced electron-ion pairs in an ionization chamber is independent of the applied voltage, but strongly depends on the used gas. The signal of one primary ionizing particle is relatively small, so it can not be used for single particle counting. But it is proportional to the deposited energy of the primary ionizing particle. Therefore an ionization chamber is often used for dosimetry.

Above a certain threshold, each ion pair produces an electron avalanche, which is proportional to the deposited energy. This operational mode can be referred to as

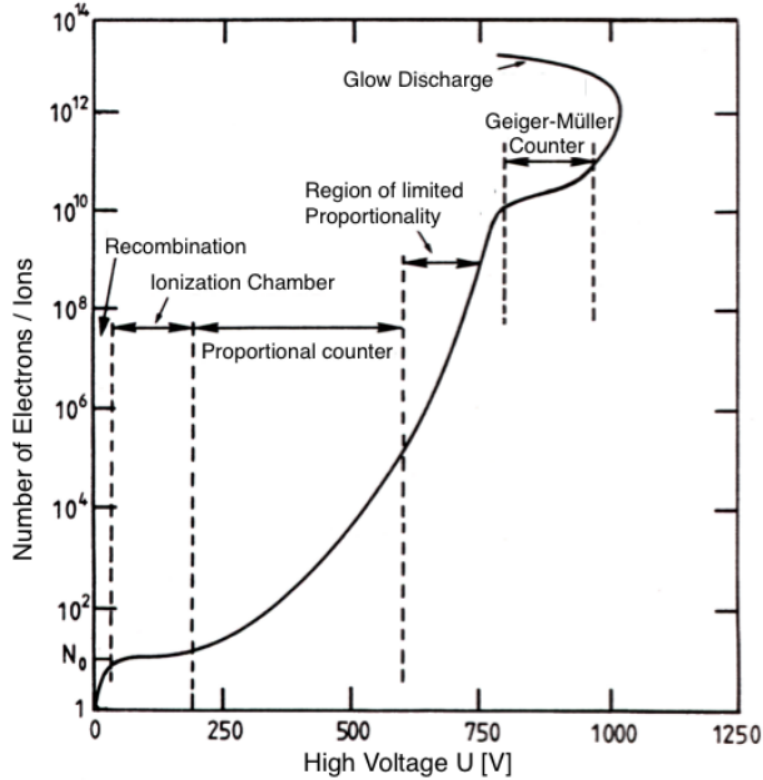


Figure 12: Different operational modes of a gaseous detector [20]

“proportional counters”. However, the efficiency of this detector also depends on the applied voltage.

If the applied voltage gets too high, additional avalanches are created, due to the production of UV-photons in the primary avalanches. Those UV-photons are not affected by the electric field and can travel freely through the detector, causing additional avalanches through ionization. The overall signal is not proportional to the primary ionization anymore. However, those “Geiger-Müller counters” produce a large output signal and are suitable for particle counting.

2.6 Silicon strip detectors

A silicon strip detector (SSD) is a semiconductor detector, which consists of many pn-junction diodes operated in reverse direction. Due to its spatial resolution of a few $100 \mu\text{m}$, it can be used as a position detector for pCT.

2.6.1 pn-junction diode

A pn-junction describes the interface of a p-type and a n-type semiconductor. By replacing atoms of the Silicon crystal with foreign atoms (“dopants”), the electron density can be increased (“donor” atoms) or decreased (“acceptor” atoms). A p-type semiconductor has less electrons (more $+h$ “holes”) and a n-type semiconductor has more electrons than the undoped material. Therefore the p-type material is positively charged and the n-type negatively.

The combination of a p-type and a n-type semiconductor is called a diode. Due to thermal fluctuations and concentration gradients, holes and electrons diffuse in both

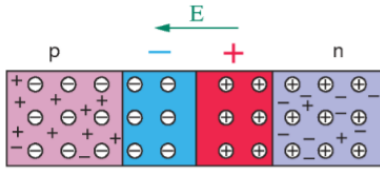


Figure 13: pn-junction diode [21]

directions and recombine. The electric field caused by the potential difference of the positive p-type and the negative n-type limits the diffusion and prevents a total recombination. In an area located around the interface almost no free charge carriers can be found. This zone is called the depletion zone (Figure 13).

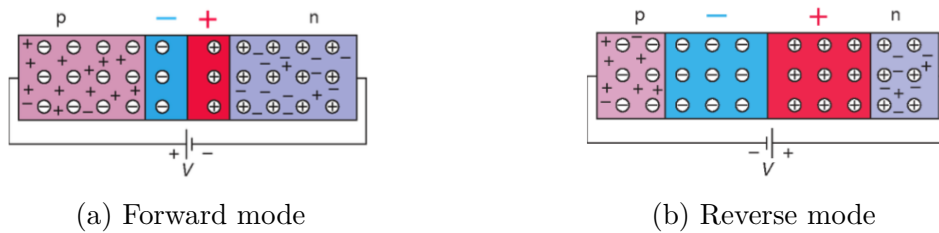


Figure 14: Diode Operating Modes [21]

When applying voltage to the diode, with a positive potential on the p-type and a negative potential on the n-type, the diode is operated in forward mode (Figure 14a). This means that electrons and holes are pulled out of the depletion zone, narrowing the depletion zone. With a certain potential difference the charges can overcome the depletion zone leading to a sudden increase of current flowing.

A diode is operated in reverse mode when the negative potential is applied to the p-type and the positive potential to the n-type. This leads to a broadening of the depletion zone and diffusion is suppressed by the increased electric field (Figure 14b). No current is flowing until a very high electric field is applied leading to a breakthrough.

2.6.2 Particle detection with Si-strip detectors

In order to use a diode as particle detector, the diode has to be operated in reverse mode. The depletion zone has to cover the whole semiconductor so that no free charge carriers can be found in the material. Only when an ionizing particle passes the detector, electron-hole pairs are produced. Those charge carriers are separated by the applied potential difference and drift to the electrodes (Figure 15). This produces a signal which can be amplified and measured.

A Si-strip detector can be modeled as a parallel alignment of a p-type semiconductor mounted on an n-type semiconductor. The p-type detector elements are long, small (few $10\ \mu\text{m}$ thick) strips, which are aligned parallel to each other on the n-type semiconductor. The length of each strip extends over the whole length of the sensor, which enables a 1D measurement of the particle's position. The distance between the strips, which is also called "pitch", ranges from a few $10\ \mu\text{m}$ to a few $100\ \mu\text{m}$. Depending on the position of the hitting particle, the signal of one of the strips is higher than the others, leading to a lateral 1D information of the particles position. In order to get a 2D image of the particles position, two Si-strip detectors rotated by a 90° angle against each other have to be used.

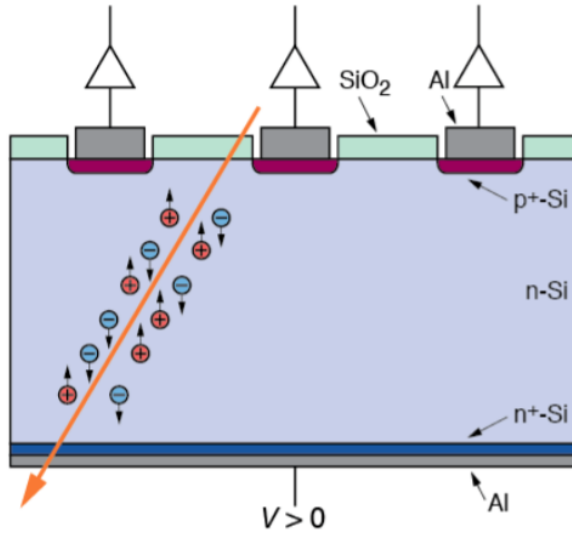


Figure 15: Cross section of a single-sided Si-strip detector [21]

2.6.3 Double sided Silicon strip detector

Another way to use the principle of a Silicon strip detectors to measure the two dimensional position of the particle, is by segmenting both sides of the SSD with strips. The strips of each side are arranged perpendicular to the strips of the other side. One side should have p-type strips, whereas the other side should have a stronger n-type doping on its strips (n^+) than the n-type silicon in the middle (Figure 16).

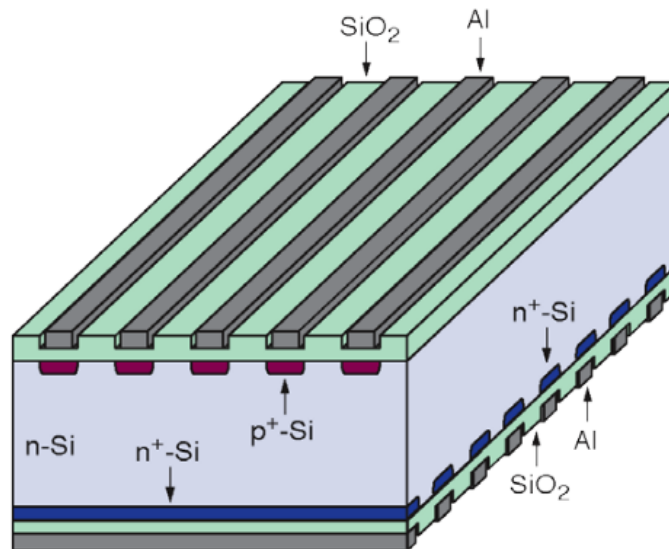


Figure 16: Double sided silicon strip detector [21]

However there is no depletion zone between the n^+ -type and the n-type substrate, which leads to an accumulation of electrons between the individual strips. The depletion zone isolates each strip electrically from each other. A lack of isolation between the strips short-circuits the strips, which makes a position determination impossible [6].

One way to circumvent this problem is by adding p^+ strips (“p-stop”) between the n^+ strips. The combination of the p-stops and the n-substrate can be considered as diodes, which prevent the accumulation of the electrons between the strips (not shown

in Figure 16).

Apart from the technical complex manufacturing of the double sided SSD, those detectors are ideal for particle position detection for pCT, since they offer high spatial resolution ($> \text{few } 10 \mu\text{m}$).

2.6.4 Charged particle in the electric field of a Silicon strip detector

In an SSD, a voltage U is applied between the strips of the p- and n-side. Depending on the geometry and doping of this semiconductor detector, an electric field is formed. The electric field \vec{E} is a vectorfield, which is the negative gradient of the electric potential Φ ($\vec{E} = -\nabla\Phi$). The electric potential can be calculated according to the Poission equation:

$$\Delta\Phi = \frac{\rho}{\epsilon} \quad (2.16)$$

As shown in equation (2.16), the electric potential depends on the dielectric constant ϵ and the charge density $\rho = Nq$, with N being the concentration of doping and q being the electric charge of the free charge carriers.

In order to solve the poission equation for an SSD, the boundary conditions have to be defined. The potential on each strip should be set to the corresponding applied potential ($\Phi|_{\text{p-strip}} = -\frac{U}{2}$ and $\Phi|_{\text{n-strip}} = +\frac{U}{2}$). Assuming that the border of the the detector is perfectly isolating, if the diode is operated in reverse bias, one can use the homogeneous Neumann boundary conditions on the surface ∂S of the detector. This means that the normal component of the electric field vanishes at the borders, so that no charge from outside can enter the detector and no charge from the inside can leave the detector ($\vec{n} \cdot \nabla\Phi|_{\partial S} = 0$).

After calculating the electric field in an SSD, the influence of the electric field on a traversing charged particle can be studied. When a moving charged particle travels through an electric field \vec{E} , it gets deflected according to the Lorentz-force (equation (2.17):

$$\vec{F} = m \cdot \vec{a} = q \cdot \vec{E} \quad (2.17)$$

q is the charge of the traversing particle and \vec{E} is the electric field.

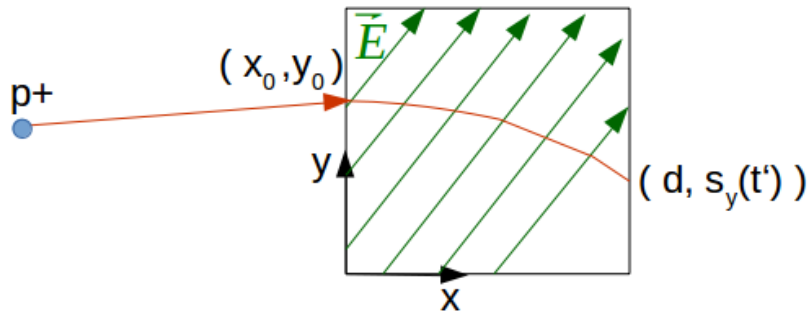


Figure 17: proton passing a homogeneous electric field

If the electric field stays homogeneous ($\vec{E} = \text{constant}$) in a certain distance $x = d$, the

two dimensional representation of the Lorentz-force reads as follows:

$$\begin{pmatrix} a_x \\ a_y \end{pmatrix} = \frac{q}{m} \cdot \begin{pmatrix} E_x \\ E_y \end{pmatrix} \quad (2.18)$$

Since $\vec{a} = \frac{d\vec{v}}{dt}$, equation (2.18) can be integrated using $\vec{v}(t=0) = \begin{pmatrix} v_{x0} \\ v_{y0} \end{pmatrix} = \text{constant}$ as the initial condition.

$$\begin{pmatrix} v_x(t) \\ v_y(t) \end{pmatrix} = \frac{q}{m} \cdot \begin{pmatrix} E_x \\ E_y \end{pmatrix} \cdot t + \begin{pmatrix} v_{x0} \\ v_{y0} \end{pmatrix} \quad (2.19)$$

Because of $\vec{a} = \frac{d^2\vec{s}}{dt^2}$, equation (2.19) can be integrated with the initial condition $\vec{s}(t=0) = \begin{pmatrix} x_0 \\ y_0 \end{pmatrix} = \text{const}$, leading to the equation of motion for a charged particle in a homogeneous electric field

$$\begin{pmatrix} s_x(t) \\ s_y(t) \end{pmatrix} = \frac{q}{m} \cdot \begin{pmatrix} E_x \\ E_y \end{pmatrix} \cdot \frac{t^2}{2} + \begin{pmatrix} v_{x0} \\ v_{y0} \end{pmatrix} \cdot t + \begin{pmatrix} x_0 \\ y_0 \end{pmatrix}. \quad (2.20)$$

In order to get the offset in y -direction, after the particle has passed the distance $x = d$, the time t' , which the particle needs to get from $x = 0$ to $x = d$, has to be calculated according to:

$$d = \frac{q}{m} \cdot E_x \frac{t'^2}{2} + v_{x0} \cdot t' + x_0 \quad (2.21)$$

The solution of this quadratic equation (2.21) reads as follows (with $(x_0 - d) < 0$):

$$t'_{1,2} = -\frac{mv_{x0}}{qE_x} \pm \sqrt{\left(\frac{mv_{x0}}{qE_x}\right)^2 - 2\frac{m(x_0 - d)}{qE_x}} \quad (2.22)$$

If the electric field in x -direction has the same sign as the charge of the particle, only the positive solution of equation (2.22) can be used, since time needs to be positive. The resulting offset in y -direction is obtained by inserting the solution of equation (2.22) in the y -component of equation (2.20) and yields

$$s_{y1}(t') = \frac{q}{m} \cdot E_y \cdot \frac{t'^2}{2} + v_{y0}t' + y_0. \quad (2.23)$$

If no electric field is applied, the proton path through a small element of thickness d can be approximated by a straight line with $d = v_{x0} \cdot t''$.

$$t'' = \frac{d}{v_{x0}}. \quad (2.24)$$

By inserting the time t'' , which the proton needs to pass the small element (equation (2.24)) in equation (2.20), the offset in y -direction without an electric field is obtained

$$s_{y2}(t'') = v_{y0}t'' + y_0. \quad (2.25)$$

The difference of the proton path in y -direction, as a result of the applied electric field reads

$$\Delta y = s_{y2}(t'') - s_{y1}(t') = -\frac{q}{m} \cdot E_y \cdot \frac{t'^2}{2} + v_{y0} \cdot (t'' - t'). \quad (2.26)$$

2.7 Monte Carlo method for particle transport

The Monte Carlo Method is a statistical method to solve different mathematical problems by statistical sampling using random numbers. It is based on the law of large numbers, which states that by conducting the same experiment over and over again, the average of the results comes closer to the expected value. This method is used to numerically approximate integrals, or to simulate processes which follow a certain probability distribution.

2.7.1 Particle Transport

In order to simulate particle transport, a stochastic model for all physics processes needs to be established. The interaction at each step of the particle's trajectory, as well as the length of each step, is chosen randomly according to the probability of each possible physical interaction at this point.

A schematic, simplified principle of the Monte Carlo algorithm from [22] is described in the following.

Different physical interactions, X_i , such as Coulomb scattering, etc. can happen with a certain probability p_i at a certain step of the particles trajectory. The probability of each process is related to their corresponding cross section σ_i [14], with $p_i = \frac{\sigma_i}{\sigma_T}$. σ_T is the total cross section and is the sum over all cross sections of all possible interactions ($\sigma_T = \sum_i^N \sigma_i$). With this definition, the relation $\sum_i^N p_i = 1$, is fulfilled. Then a uniformly distributed random number r in the range $[0, 1]$ is generated.

Case 1 ($r < p_1$): process 1 is chosen

Case i ($\sum_j^{i-1} p_j < r < \sum_j^i p_j$): X_i is chosen

After randomly choosing a process, the average length of the particle's trajectory, without an interaction can be calculated. This is the mean free path μ , which is defined as

$$\mu = \frac{1}{n\sigma_i}. \quad (2.27)$$

In equation (2.27), n is the number of target particles per volume. After each step (with length μ), the next process is chosen randomly until the particle has moved through the whole simulated volume, resulting in a particle track.

Each track of the particle leads to a certain result for the quantity to be measured. After repeating this simulation many times, a statistic evaluation of this measurable quantity can be made. However, it is necessary to mention that the simulated output strongly depends on the theoretical models, which have to be adapted to the latest experimental data.

3 Materials and methods

3.1 The MedAustron particle accelerator

All experiments were conducted at the MedAustron particle therapy accelerator (MAPTA). The accelerator itself is capable of accelerating protons from 62.4 MeV up to 252.7 MeV and carbon ions up to 400 MeV/u for clinical purposes. For research, protons up to 800 MeV can be used.

The whole accelerator complex consists of three different ion sources, a linear accelerator (LINAC), a synchrotron and an so-called “extraction-line” to deliver the beam to the four different irradiation rooms [23] (Figure 18).



Figure 18: MedAustron facility

This accelerator has four slots for different ion sources. One of them is used to produce H_3^+ ions and the other to produce C^{4+} ions. The third slot is used as a redundant source, in case another fails. The fourth slot could be used for other ion-sources such as ^4He .

Before the ions can enter the synchrotron, they have to be pre-accelerated in a linear accelerator. A LINAC consists of many electrodes, which electric potentials are changing its polarity due to an applied alternating electric field. A positively charged particle is attracted by the negative potential of the electrode. Whenever the particle leaves a negatively charged electrode, the sign of the next electrode changes from positive to negative, so that the particle gets accelerated again. This part of the accelerator is called the “low-energy beam transfer” (LEBT) since the energy of the accelerated ions goes up to 7 MeV/u [24].

After the LINAC the ions pass a carbon stripping foil in the medium energy beam transfer (MEBT), to strip off electrons. When using H_3^+ as an ion source, protons are generated at this stage and C^{6+} when using C^{4+} .

After the MEBT, the ions are injected into the synchrotron ring with a circumfer-

ence of 77.4 m. A synchrotron is a particle accelerator where the ions travel through a circular vacuum tube. The acceleration itself only takes place in a small radio frequency cavity, which is operated with a sinusoidal electric field. The period of the electric field has to match the time which the particle needs for one revolution to guarantee the right polarity for acceleration. So it has to be modulated after each acceleration period.

In order to keep the ions on a circular track, high magnetic fields of dipole magnets are used. The higher the particle's kinetic energy, the higher the magnetic field strength has to be to keep the particles on the track.

Also quadrupole magnets are used for beam focusing. The magnetic field of a quadrupole magnet only allows focusing in one dimension. For vertical and horizontal beam focusing, two quadrupole magnets are placed after each other.

If there is a slight deviation in momentum from the particle with an ideal designed orbit, the particles start to oscillate around this orbit because of the magnetic field.

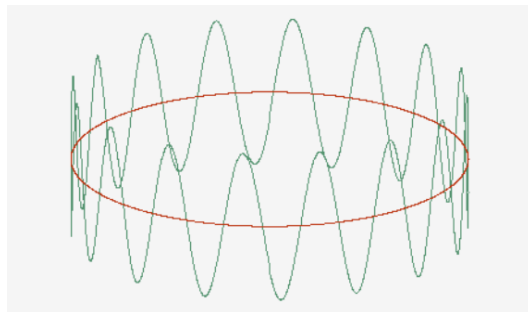


Figure 19: Betatron oscillation

This transverse oscillation is known as “Betatron oscillation” (Figure 19) for which a mathematical description can be found in [25]. The frequency of this transverse oscillation is called the particle's “tune” and its dependence on momentum is called “chromaticity”.

In the presence of an inhomogeneous magnetic field of magnetic sextupoles, an additional perturbation in momentum can be invoked on the particles. This can lead to unstable betatron oscillations or even resonances. When the particle oscillates in resonance, the amplitude of the oscillation increases continuously. When the amplitude of this transverse motion reaches a certain limit, the particle can enter a septum, which is placed at the margin of the vacuum tube. The field of the septum, which can be either electric or magnetic, deflects the incoming beam and extracts it to another beam line. MedAustron uses an electric septum for beam extraction.

Before the extraction, the particles are accelerated in the synchrotron until they reach the desired energy. Then they are extracted via the resonant extraction to the high energy beam transfer (HEBT). This HEBT connects the synchrotron to the different irradiation rooms and houses beam diagnostic hardware for quality assurance.

3.1.1 Particle flux reduction methods

MedAustron provides particle fluxes in the order of 10^9 s^{-1} for particle therapy. Those high fluxes are needed to efficiently irradiate the patient in a short amount of time.

However, for pCT lower particle fluxes are required, since single particle counting has to be achieved. Electronics which are capable of this require particle fluxes which are in the order of $10^5 - 10^6 \text{ s}^{-1}$. For this purpose MedAustron has provided three different extraction methods which entail lower particle fluxes [26]. The basic principle of those three methods will be discussed in the following

I) **EFE fast deflector:**

The EFE is mounted in the LEBT and can be used to reduce the number of particles injected in the LINAC. The EFE is a fast deflector which consists of two electrodes (as the electric septa), between which a high voltage (5 keV) can be applied [27]. When the electric field is switched on, the beam gets deflected towards the synchrotron.

So it can be considered as a gate which “allows” particles to enter the synchrotron. The longer the gate is open, the more particles accumulate in the synchrotron. The EFE can be opened between 1 and $30 \mu\text{s}$ (medical mode). So the number of injected particles can be varied up to a factor of 30 (not perfectly linear) [26].

For a constant extraction time and a lower number of injected particles, the flux is reduced.

II) **Beam scraping via chopper:**

The chopper at the MedAustron facility consists of four magnets and a beam dump, as shown in Figure 20. It is situated in the HEBT, after the synchrotron ring. Depending on the magnetic field the beam gets dumped in, or guided around the beam dump [23].

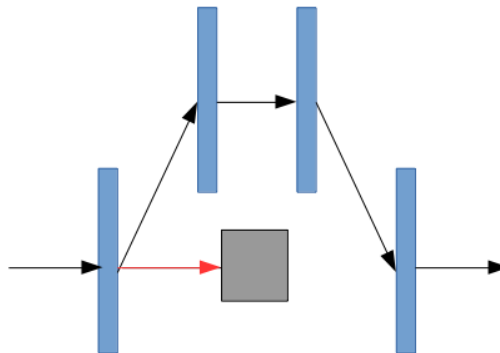


Figure 20: 4 chopper magnets (blue) with a beam dump (grey)

Normally it is used to dump the beam completely for safety reasons. However, the chopper can also be used for a lower particle flux. This is done by adjusting the magnetic field of the chopper magnets in a way that only parts of the beam (from the beam halo) are guided around the dump, whereas other particles are scraped off. This reduces the number of particles in the accelerator and again, for a constant extraction time, the particle flux is reduced.

III) **Betatron slow extraction:**

The third particle flux reduction method is based on resonant extraction as discussed in Section 3.1. Before this process, the particles are accelerated in the synchrotron to a momentum slightly too low to fulfill the resonance condition of the betatron oscillation. This condition is only true for a particle with a certain

momentum and transverse oscillation amplitude [28].

The betatron oscillation starts getting unstable when applying the inhomogeneous magnetic field of a magnetic sextupole (betatron core). This field induces an electric field, which slowly increases the momentum of the traversing particles until they are driven to resonance. Since the particles in the accelerator entail a large momentum spread, not all particles fulfill the resonance condition at the same time. The slower the particles are accelerated, the slower particles are driven into resonance and are extracted. A schematic drawing of a betatron core is shown in Figure 21.

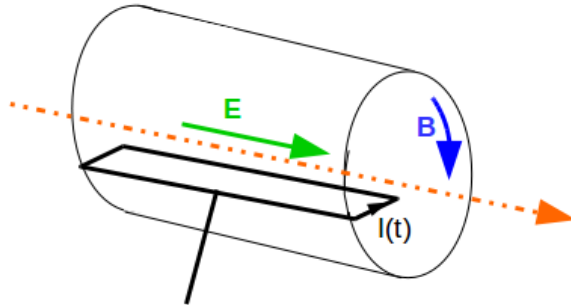


Figure 21: Schematic drawing of a betatron

An alternating current $I(t)$ going through the coils of the betatron induces a changing magnetic field due to the law of induction. A changing magnetic field induces an electric field, which, in this case, is parallel to the particle's ideal orbit. When a charged particle passes this electric field, its kinetic energy changes. Therefore, the tune of the particle is changed and the betatron oscillation changes. This can lead to resonance of the betatron oscillation and results in an increase of the amplitude of the oscillation.

The change in momentum Δp of a particle with momentum p depends on the change in magnetic flux Φ according to [28]. It also depends on the circumference C of the accelerator, the magnetic field B of the betatron and the radius of curvature ρ of the designed track (equation (3.1)). These quantities are connected as

$$\Delta\Phi = CB\rho \frac{\Delta p}{p}. \quad (3.1)$$

For a uniform (unbunched) extraction through resonance, the magnetic flux variation in time should be constant ($\frac{d\Phi}{dt} = \text{constant} = V_a$). This allows, by dividing equation (3.1) by the extraction time T_{ext} , to obtain a relationship between the induced betatron voltage V_a , the extraction time T_{ext} and the relative change in the particle's momentum and reads

$$V_a = \frac{d\Phi}{dt} = CB\rho \frac{\Delta p/p}{T_{\text{ext}}}. \quad (3.2)$$

As can be seen in equation (3.2), for a low, constant betatron voltage, the extraction time can be elongated. A longer extraction time for a constant number of particles results in a lower particle flux. According to [26], the flux can be reduced by a factor of 10 with a slower betatron extraction.

3.2 VME based particle counting and trigger system (PCTS)

The combination of the previously discussed particle flux reduction methods leads to a significant decrease of the particle rate. The MedAustron beam diagnostics were not designed to detect those low fluxes. Therefore a fast and suitable beam monitor, consisting of plastic scintillators, PMTs and a field programmable gate array (FPGA) based Versa Module Eurocard-bus (VME) logic unit had to be installed and tested. This system was also designed to serve as a trigger unit for other devices.

Before describing the experimental setup, a brief overview of the basics of VME and FPGA programming will be discussed in the following.

3.2.1 Field programmable gate array

The field programmable gate array is an integrated circuit which consists of an array of programmable logic blocks and configurable interconnects to connect the logic blocks in a desired way (Figure 22).

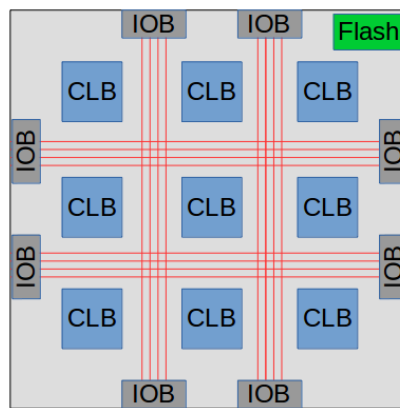


Figure 22: Schematic drawing of a FPGA with configurable logic blocks (CLB), interconnect wires, I/O blocks (IOB) and a flash memory for the circuit design.

In contrast to a processor, which has a hard wired circuit, the integrated circuit of a FPGA can be designed by a customer (therefore “field”) via a hardware description language (HDL). In each logic block any desired circuit consisting of logic gates, flip flops etc. can be configured [29].

The so called "gate-ware" is programmed in a HDL such as “Very High Speed Integrated Circuit Hardware Description Language” (VHDL) and loaded on a flash memory on the FPGA. Since the logic circuits are realized directly in hardware, fast and parallel processing is possible, whereas the actual tasks for a processor need to be coded and are executed sequentially.

The only drawbacks which have to be considered when programming FPGAs are the finite number of I/O pins and a finite number of gates. This can reduce the possible complexity of a designed circuit. Also when redesigning the circuit of a FPGA, the whole chip has to be reconfigured and cannot be used during this period.

3.2.2 VME

In nuclear and high energy physics it is common to use certain standards for measurement electronics. This means that all electronic devices are designed in modules which

are standardized in their mechanical and electrical specifications. Those modules are mounted in a crate of a specific size and are operated with a certain operating voltage. Depending on the standard, those modules can be connected analogously (Nuclear Instrument Standard (NIM)) or via a data bus (VME) [30].

A data bus is a data connection of two or more devices via multiple wires. Those wires also contain addressing information about the memory location of where the data is being send to or retrieved from. The VME-bus is a bus system based on a master/slave architecture which can have multiple masters. The master controls other devices (slaves), but it cannot be controlled by them.

Such a VME bus system can be divided into four sub buses:

- the data transfer bus is used for reading and writing operations between the modules
- the arbiter bus gives permission to each device to use the bus and notifies requesting devices when the bus is busy
- the interrupt handler can receive and handle interrupts
- the utility bus supports a system clock which is needed for synchronisation

The main advantages of a VME system is that it can be controlled remotely from a PC through an optical link or USB. Also the data acquisition can be done remotely via a PC in contrast to NIM systems.

3.2.3 PCTS setup

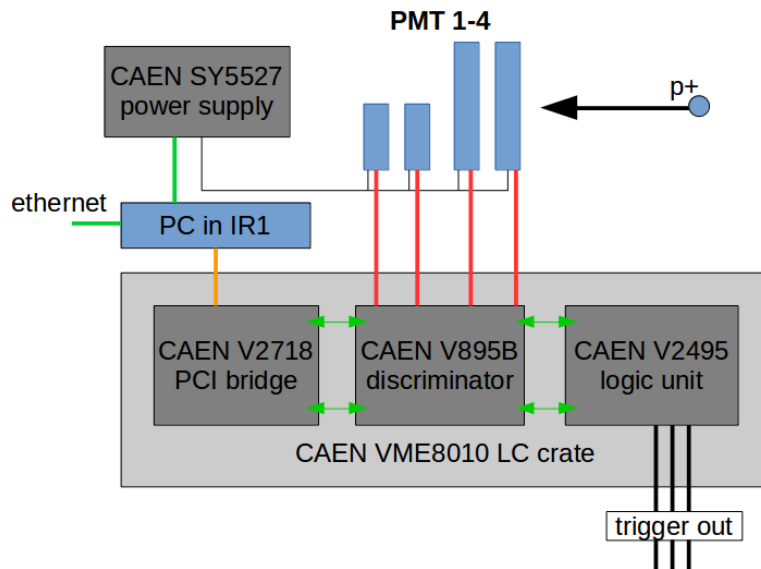


Figure 23: Particle counting and trigger setup

A schematic drawing of the whole PCTS setup is shown in Figure 23. The particle counting and trigger system consists of four plastic scintillators and a VME based

trigger and logic unit, which was programmed with VHDL. An in-house developed readout software “COSCAT_GUI” [31], written in C++ was used for data acquisition.

Scintillators:

The PCTS should be able to achieve single particle counting at low particle rates. For this purpose fast plastic scintillators were chosen, since they have a rise and fall time of a few ns.

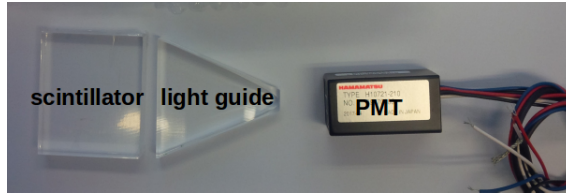


Figure 24: Scintillator

For this setup, four EJ228 plastic scintillators from Eljen [32] were used. Two of those scintillators had a total volume of $50\text{ mm} \times 50\text{ mm} \times 10\text{ mm}$ and the other two $25\text{ mm} \times 25\text{ mm} \times 10\text{ mm}$. As a light guide PMMA fish tail light guides ($50\text{ mm} \times 10\text{ mm}$) and ($25\text{ mm} \times 10\text{ mm}$) were used and connected to the photocathode ($\varnothing = 8\text{ mm}$) of a Hamamatsu H10721-210 photosensor [33] (Figure 24). The scintillators were assembled by using optical grease and double-sided optical duct tape by the Institut für Hochenergiephysik in Vienna (HEPHY).

The PMTs were powered by a CAEN SY5527 power supply [34], which was controlled remotely (via SSH). The supply voltage was set to 5 V and the control voltage could be varied between 0.5 and 1.1 V in order to adjust the gain of the PMTs.

Leading edge discriminator:

The signals of the PMTs (red lines in Figure 23) were fed into the CAEN V985B 16 channel leading edge discriminator, mounted in the CAEN VME8010 LC crate.

A discriminator is a module which converts an analogue signal into a logic signal if the analogue signal exceeds a defined threshold (Figure 25).

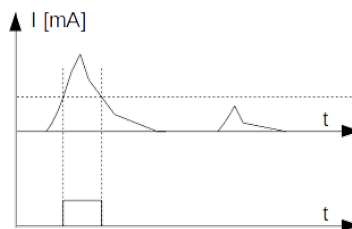


Figure 25: Leading edge discriminator

The length of the output pulse of this “leading edge discriminator” usually depends on the height and width of the input pulse. However, some discriminators feature a pulse shaping function.

The CAEN V985B leading edge discriminator contains different registers which could be addressed via the VME bus. By changing the value of a register, the output pulse length of the first eight or last eight output channels could be varied from 5 to 40 ns. Also the threshold of each channel could be set between -1 and -255 mV .

The configuration and readout software was implemented in a C++ program, which used the CAENcomm library as a C++ to VME interface (COSCAT_GUI [31]).

Coincidence scaler and trigger firmware (COSCAT):

The digitized signals from the PMTs were forwarded to the CAEN V2495 logic unit, which was operated with a 50 MHz clock. This logic unit has a programmable FPGA, which was programmed with VHDL. The design of the “Gateway” and its logic blocks is depicted in Figure 26.

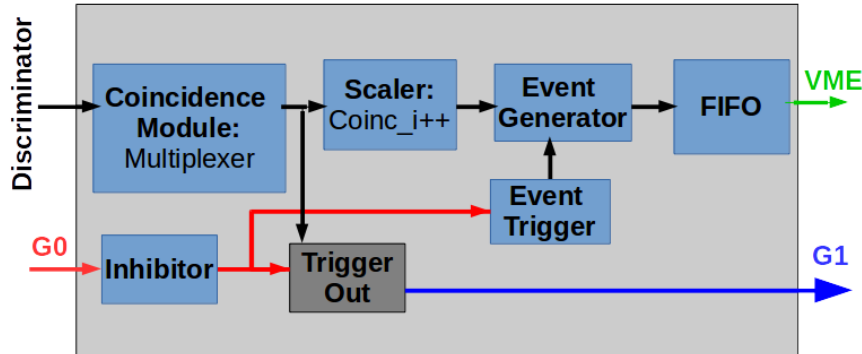


Figure 26: COSCAT FPGA design, G0, G1 are LEMO I/O ports

The purpose of this gateway is to create a trigger signal, whenever a coincidence is measured and to measure the number of coincidences per time for beam monitoring.

The functionality of each configurable logic block was tested via a simulation in ModelSim [35]. In order to use Modelsim, a so-called “testbench” with simulated input signals had to be defined. The simulated input signals were then run through the logic block and the input and output signals could be observed at any time of the simulation (Figure 27).

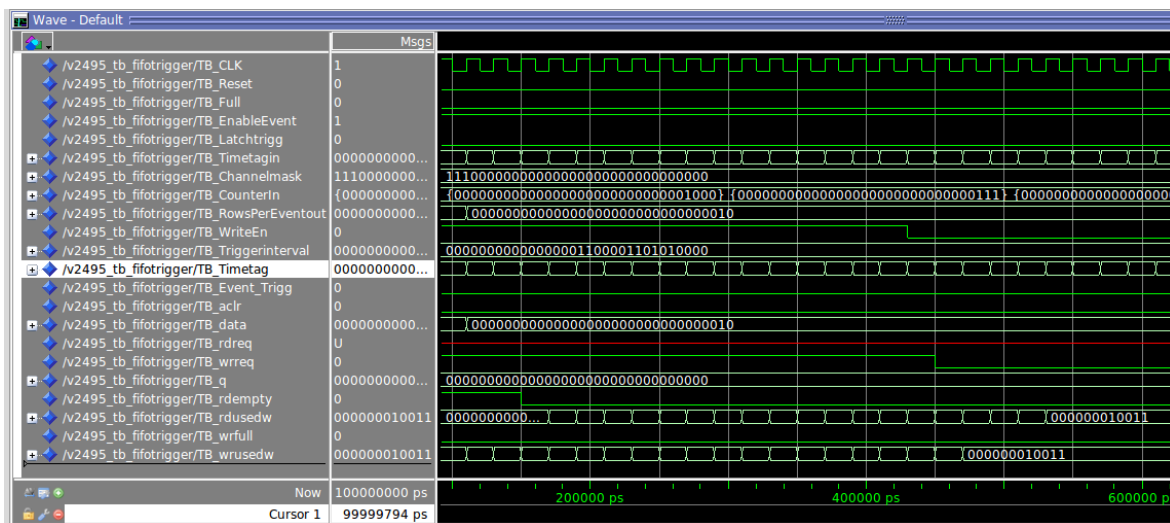


Figure 27: Example of a ModelSim-simulation of the Event Generator, Event Trigger and FIFO module

In order to allow fast particle counting and triggering, the coincidence module of the

FPGA was designed asynchronously to the system clock.

Whenever a proton passes the first scintillator, the coincidence module opens a gate for a defined time of 20 ns. When this particle goes through the next scintillator, the signal of the second PMT and the gate of the first PMT generate a pulse for a PMT1 + 2 coincidence and the gate is closed (Figure 28a). If there is no particle going through the second scintillator, the gate closes itself after 20 ns and a new particle can be detected (Figure 28b). This can happen asynchronously to the clock, since a delayed input pulse (by 20 ns) of the first PMT is used to close the gate of the not delayed input pulse.

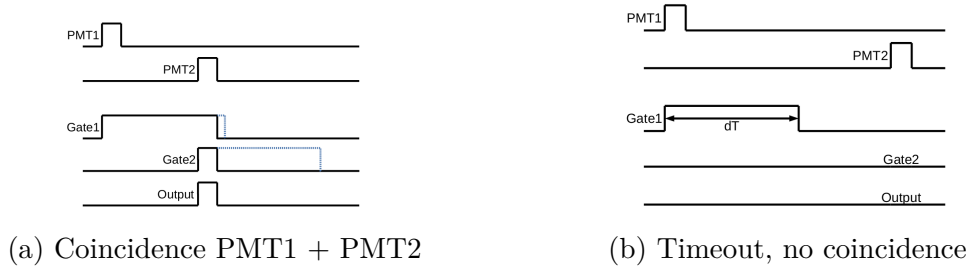


Figure 28: Asynchronous coincidence [31]

If more than two PMTs are used, the coincidence are built similar to Figure 28a. However, the direction of the particle motion has been taken into account. The gates for a certain PMT only open, when the gates of the previous PMTs have already been opened (Figure 29):

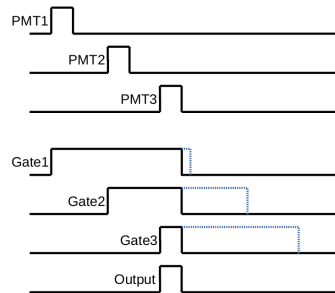


Figure 29: Coincidence PMT1 + PMT2 + PMT3 [31]

Any desired combination of coincidences could be sent from the coincidence module to the scaler logic block. The scaler logic block contains an array of 32 bit elements, with one element per possible coincidence. An element of this “coincidence array” is incremented by one, whenever the corresponding coincidence input signal switches from off to on. This also happens asynchronously to the system clock.

The events from the Scaler block are sent to the event generator, which generates events as a sequence of 32 bit data blocks (state machine in Figure 30). Each event is assigned with a certain event number and a timestamp as a header. The header is followed by an array of all possible coincidences, which contain the number of the coincidences counted since the last event. The events are forwarded to a first in first out buffer (FIFO), where they are stored until all events are read out via a block transfer.

The time between two events (“dwelltime”) can be set via the “Event Trigger” module. This module sends out a defined pulse everytime an internal counter equals the predefined dwelltime. This pulse is used to reset the scaler and to start the event building

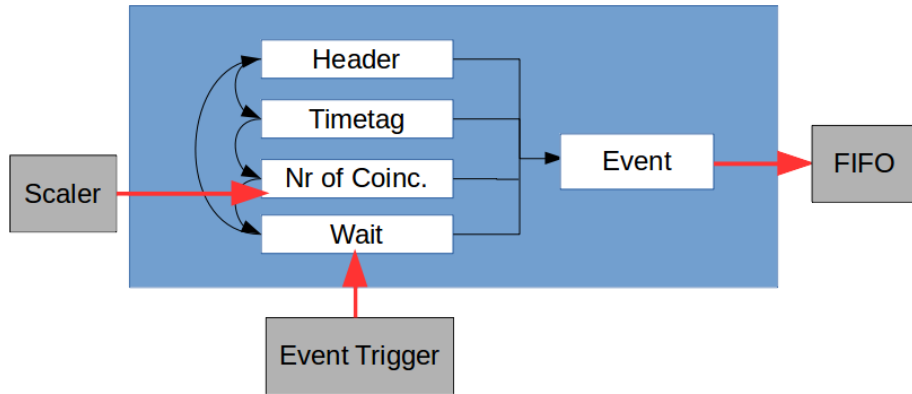


Figure 30: State machine of the Event Generator block

process. The dwelltime needs to be larger than the time one event building process takes. The less coincidences need to be read out, the faster the event generator works (few 100 ns).

By looking at the number of particles per dwelltime, the beamprofile and the particle flux can be analyzed.

This Gateway is also able to generate trigger signals for other devices. This is realized by the “Trigger Out” module, which has the coincidences as an input signal. The trigger itself can be trigger via software (COSCAT_GUI [31]) for a functionality test, or by one of the coincidences. The output length of the trigger signal can be chosen greater than 5 ns and the signal is forwarded to the G1 output of the CAEN V2495 logic unit (Figure 26).

The output pulse of the Trigger Out module follows the NIM standard. NIM logic is a current-based logic with a negative logic level. For this standard a logic '1' corresponds to a current between -12 mA and -32 mA . For a terminating resistance of $50\ \Omega$ this leads to a voltage between -0.6 V and -1.6 V . A logic '0' corresponds to 0 mA and therefore 0 V for a $50\ \Omega$ terminating resistance [36].

The output of both the Trigger Out and the Event Generator can be vetoed by the “Inhibitor” module. This module is driven by the G0 input of of the CAEN V2495 logic module (Figure 26).

Readout software

The VME setup was controlled via the CAEN V2718 PCI bridge. This bridge was connected to a PC in the irradiation room 1 (IR1) of MedAustron via an optical link. The readout software “COSCAT_GUI” [31] on this PC was used to configure and to read out the FPGA of the logic unit. This software converts the data from the FPGA to a ROOT [37] format and allows a live view of the acquired data.

3.3 Plateau Curve measurement

Before using the scintillators and PMTs for pCT experiments or beam monitoring, the gain of the PMTs had to be optimized. This was done by adjusting the control voltage V_{ctrl} of the PMTs. A higher gain amplifies the output signal of the PMTs and allows to measure particles, which would have had a signal lower than the discriminator threshold.

However, with a higher gain also noise is amplified and therefore a detection-efficiency for each PMT and each control voltage has to be defined and measured.

The detection efficiency ϵ_i (with $i \in [1, n]$) for n PMTs and a constant measurement time is defined as [14]:

$$\epsilon_i = \frac{\#\text{coinc}(1, 2, \dots, i, \dots, n)}{\#\text{coinc}(1, 2, \dots, \text{not } i, \dots, n)} \quad (3.3)$$

As can be seen in equation (3.3), the detection efficiency of a PMT is defined as the ratio between the number of events where all PMTs have a coincident signal and the number of events, where all but one PMT generate a coincident signal. Equation (3.4) shows an example for the detection efficiency of PMT1:

$$\epsilon_1 = \frac{\#\text{coinc}(1, 2, 3, 4)}{\#\text{coinc}(2, 3, 4)} \quad (3.4)$$

While changing the control voltage of one PMT and fixing V_{ctrl} for the other PMTs, the detection efficiency was measured for each PMT. Plotting the detection efficiency over the control voltage, a so-called ‘‘plateau curve’’ can be obtained.

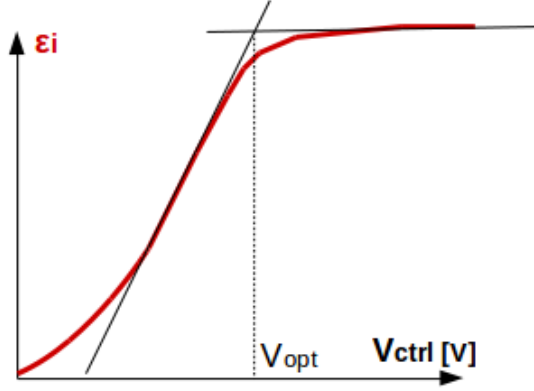


Figure 31: Plateau curve of a PMT

In Figure 31, a schematic drawing of a plateau curve is shown. The detection efficiency of a PMT rises until it reaches a plateau and saturates. This means that above a certain voltage, the efficiency cannot be increased any further and noise is drastically amplified.

There is a rule of thumb to obtain the optimum control voltage for an optimal detection efficiency, while keeping the noise amplification as low as possible. The control voltage V_{opt} at the point of intersection, where the tangent of the rising part of the plateau curve and the tangent of the plateau has to be obtained (Figure 31).

3.3.1 Experimental setup

The plateau curves of all four PMTs, as described in Section 3.2.3, were measured at the irradiation room 1 at the MedAustron facility. Protons with a kinetic energy of 252.7 MeV and a beam intensity of 1×10^8 p/s were chosen.

The PCTS setup was used to measure the number of all possible coincidences per time (singlePMT1, singlePMT2, ..., Coinc12, Coinc123, Coinc1234, ..., Coinc234).

Since the geometry of the proton beam widens due to MCS, the smaller PMTs were

chosen to be in front of the larger ones to capture the whole beam. The first small PMT was positioned at the isocentre of the beam. At this position a straight proton beam with a defined geometry can be assumed. The experimental setup is depicted in Figure 32.

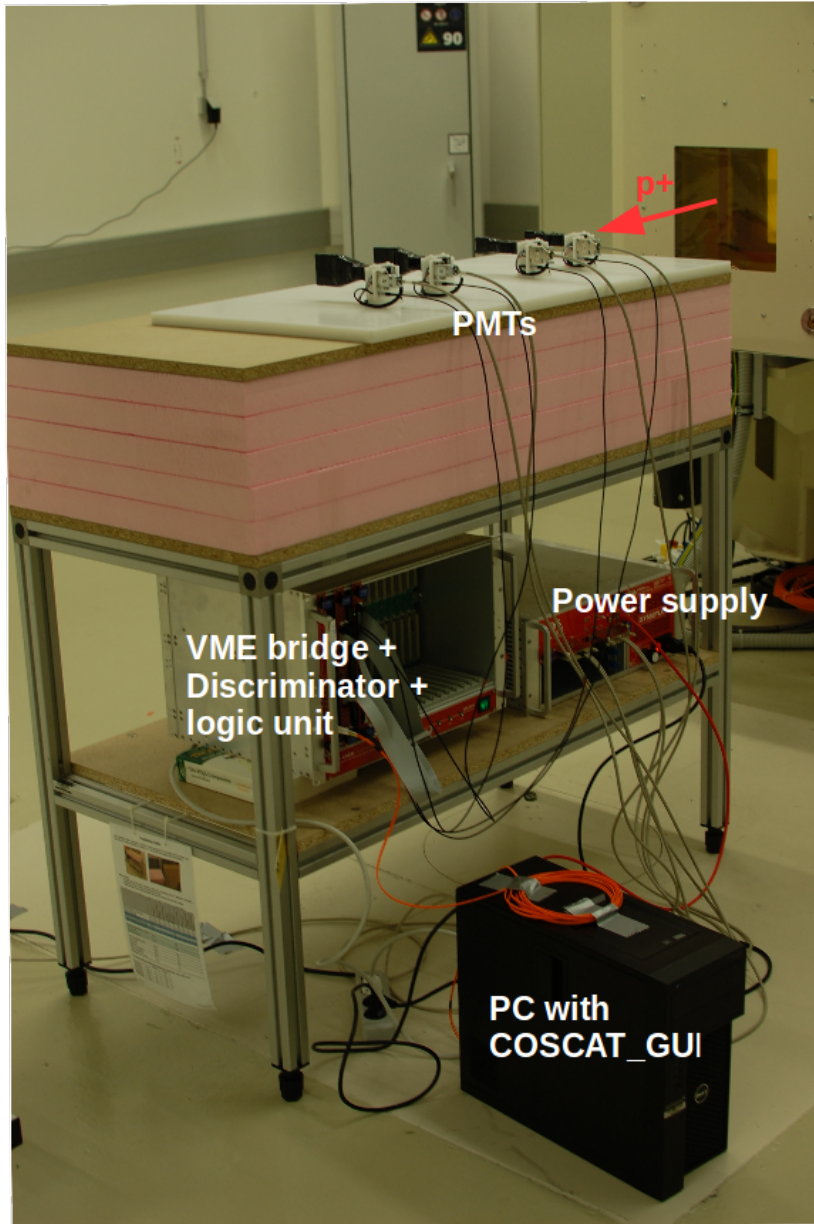


Figure 32: Plateau curve measurement setup [38]

The PMTs were powered with the CAEN SY5527 power supply, which was controlled remotely via SSH. The control voltages of the small PMTs were set to 0.85 V and to 0.9 V for the bigger ones. Those values were chosen after a previous measurement, where the dark counts (without a beam) were measured. Below those voltages hardly any false coincidences (dark counts) were measurable.

During the plateau curve measurement of one PMT, the other three PMTs were operated with a constant gain and the control voltage of the fourth PMT was varied between 0.5 V and 1.1 V.

The number of coincidences were obtained by the COSCAT firmware, which was controlled via the COSCAT_GUI [31] software. It was used to set the discriminator threshold of all four PMTs to -40 mV. The data were stored in a ROOT [37] format and then analyzed.

In order to guarantee that all protons go through all four PMTs a laser system to align the detectors was used (Figure 33):



Figure 33: Alignment of all four scintillators [38]

3.4 Beam geometry measurements

Before using the PCTS setup for particle flux measurements, the beam geometry obtained by different particle flux reduction methods has to be known. Especially the chopper, which scrapes off parts of the beam, could change the geometry, if not set properly.

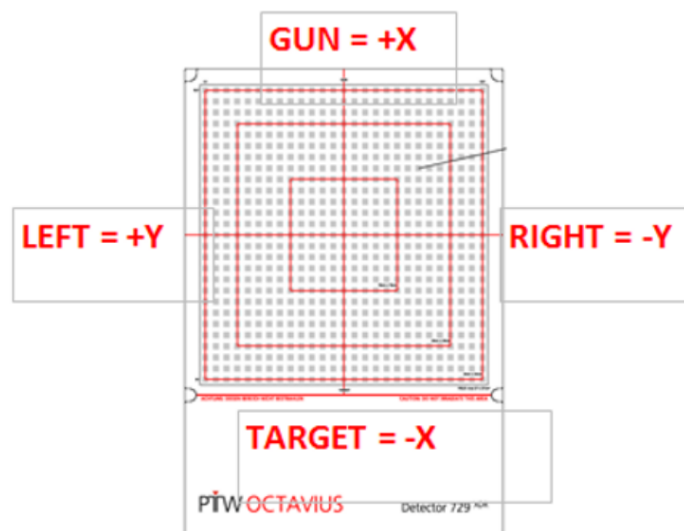


Figure 34: Octavius ionization chamber array [39]

For this purpose the Octavius ionization chamber [39] was used. The Octavius detector consists of an array of 27x27 ionization chambers, which are aligned 1 cm next to each other (Figure 34). Each chamber is filled with air and has a total active volume of of $5\text{ mm} \times 5\text{ mm} \times 5\text{ mm}$.

The Octavius detector collects the charges, produced by traversing ionizing particles, from each chamber after a defined time. Since this gaseous detector is operated in an ionization chamber mode, the signal should be proportional to the deposited energy. Because of that, the Octavius is usually used for dosimetry.

3.4.1 Experimental setup

The Octavius detector was mounted in a slab holder (Figure 35) and operated remotely via the “BeamAdjust” software, provided by PTW [40]. The dose distribution on the detector was measured for different particle flux reduction methods. The detector was also placed at two different positions along the beam direction. At first it was positioned at the isocentre of the beam and then it was placed 109.65 cm behind the isocentre.

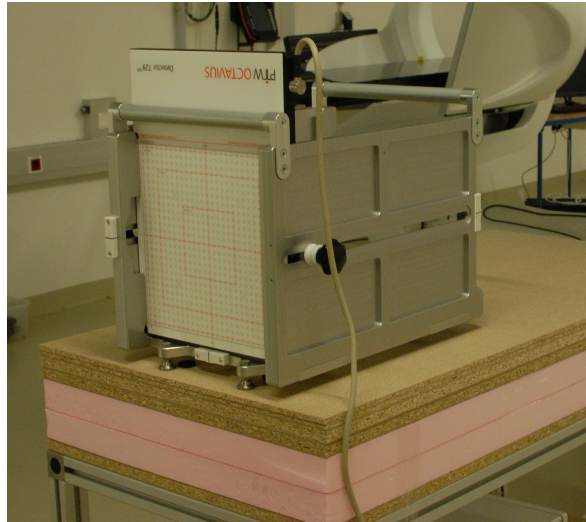


Figure 35: Octavius measurement [38]

From the normalized dose distributions, the beam profiles were obtained by using a 2D Gaus fit. The fitted beam profiles were analyzed and compared to the profiles obtained via medical mode (without any particle flux reduction).

3.5 Particle flux measurements

After looking at the beam profiles, the particle rates for different reduction methods were measured. This was done by using the PCTS setup with two of the bigger scintillators. One of the smaller scintillators was connected to a Tektronix TDS3000C oscilloscope to monitor a possible pile-up of the PMT signal.

At the same time the trigger out signal of the PCTS was connected to a Silicon strip detector from the semiconductor group from HEPHY, to test the functionality of the PCTS as a trigger module. The HEPHY group used the trigger signals to measure the stopping power of protons in Silicon. A detailed description of the SSD and their

results can be found in [41].

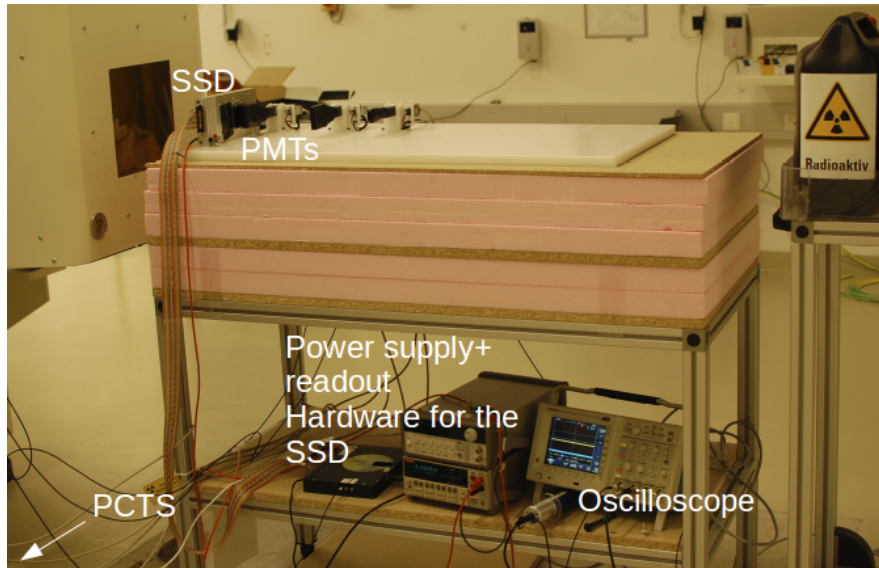


Figure 36: Particle flux measurement [38]

As can be seen in Figure 36, the PMTs were placed behind the SSD. This could be done, since the readout hardware of the SSD continuously writes the data into a buffer. Only the timing of the readout process ($\hat{=}$ buffer depth) had to be adjusted to synchronize the trigger signal with the SSD readout hardware.

3.6 Beam telescope setup for pCT

Within the second part of this thesis, a beam telescope setup for pCT was designed, simulated and tested experimentally. The telescope consists of four double sided SSDs, mounted on 4 metal bars. Six SSDs, including readout electronics and a readout software, were provided by HEPHY. The functionality of each of the SSDs was tested individually at HEPHY with a radioactive source. The four best performing SSDs were used for the final telescope. A picture of one of the double-sided SSD is shown in Figure 37a and Figure 37b:



(a) p-side

(b) n-side

Figure 37: Double sided Silicon strip detector [38]

As can be seen in Figure 37, the strips of each side of the SSD are soldered to the front-end readout electronics with four read out chips per side (golden chips in Figure 37). Those APV25 readout chips are ASICs, which have 128 channels of charge sensitive preamplifiers each and signal shapers for analogue signal processing [42]. By looking at Figure 37b, one can see that only half of the APV25 chips on the n-side of the SSD are soldered to the SSD. This is due to the fact that a p-stop is positioned between two strips of the n-side, leading to a pitch on the n-side twice as big as on the p-side (lower spatial resolution).

The most important specifications of the double-sided SSD is summarized in the following according to [43]:

- Active area: 6.76 cm^2
- Total area: 8.12 cm^2
- Number of strips on p-side: 512, no intermediate strips
- Number of strips on n-side: 256, no intermediate strips
- Pitch on p-side: $50 \mu\text{m}$
- Pitch on n-side: $100 \mu\text{m}$
- Strip implant area on p-side: $2.56 \text{ cm} \times 15 \mu\text{m}$
- Strip implant area on n-side: $2.56 \text{ cm} \times 25 \mu\text{m}$
- Silicon substrate thickness: $300 \mu\text{m}$
- Passivation thickness: 500 nm (on both sides)
- Coupling oxide thickness: 360 nm (on both sides)
- Aluminium thickness: $1.4 \mu\text{m}$ (on both sides)

The data acquisition system APVDAQ [42], which is VME based and controlled with a LabWindows/CVI software, was used for all the experiments with the telescope. The SSD was operated with $\pm 50V$ ($\cong 100V$) and the APV chips were powered with a low voltage power supply. The complete beam telescope was tested with myons before it was used at MedAustron.

In addition a rotating table for pCT experiments was designed and controlled with a Raspberry Pi 3 Model 3+ [44]. On this table two different phantoms were placed and their influence on the beam geometry was studied.

3.6.1 Electric field calculation

Before simulating and using the beam telescope, the influence of the applied electric field of each SSD on the proton path was studied. For this purpose the Poisson equation was solved for the previously described SSDs according to Section 2.6.4.

Since the potentials are symmetrically applied on each side ($-50V$ on the p-side and $50V$ on the n-side), the potential in the middle of the SSD was assumed to be

homogeneously 0 V at the whole middle plane ($\Phi|_{\text{middle}} = 0 \text{ V}$). With this assumption the Poisson equation could be solved for each side independently.

Another assumption that was made, was that for each side of the SSD the electric field does not change along the direction of the strips, since the potential and the geometry does not change along the strips.

Both of those assumptions drastically simplify the problem, so that instead of solving the 3D Poisson equation of a double sided SSD, a 2D Poisson equation had to be solved for each side individually. On the n-side the p-stops were taken into consideration.

The 2D poisson equation was discretized using the finite difference method [45]. The discretized Laplacian operator in two dimensions reads as follows:

$$\Delta\Phi = \frac{\partial^2\Phi}{\partial x^2} + \frac{\partial^2\Phi}{\partial y^2} = \frac{\Phi_{x_{i+1},y_j} - 2\Phi_{x_i,y_j} + \Phi_{x_{i-1},y_j}}{\Delta x^2} + \frac{\Phi_{x_i,y_{j+1}} - 2\Phi_{x_i,y_j} + \Phi_{x_i,y_{j-1}}}{\Delta y^2} \quad (3.5)$$

For a constant element size in x and y direction ($\Delta x = \Delta y = \Delta h = 5 \mu\text{m}$) the discretized Poisson equation simplifies to:

$$\Delta\Phi = \frac{\Phi_{x_{i+1},y_j} + \Phi_{x_{i-1},y_j} + \Phi_{x_i,y_{j+1}} + \Phi_{x_i,y_{j-1}} - 4\Phi_{x_i,y_j}}{\Delta h^2} = \frac{N_{x_i,y_j} \cdot q}{\epsilon} \quad (3.6)$$

In equation (3.6) N_{x_i,y_j} is the doping concentration and q is the charge of the free charge carrier at position x_i, y_j ($i \in [1, n_x]$ and $j \in [1, n_y]$, with n_x and n_y being the number of elements in x and y direction). q is ± 1 , depending on the free charge carriers being holes or electrons. The values for the doping concentration of each type of silicon semiconductor was taken from [21].

The boundary conditions were implemented according to Section 2.6.4. Because of the previously mentioned assumptions Dirichlet boundary conditions for the middle could be set, i.e. $\Phi|_{\text{middle}} = 0 \text{ V}$.

In order to use faster and simpler numeric algorithms for the solution of the 2D Poisson equation, the 2D grid of the cross section of the SSD was mapped on a 1D vector ($\Phi(x_i, y_j) \mapsto \Phi(u_k)$, with $k \in [1, n_x \times n_y]$) according to Figure 38.

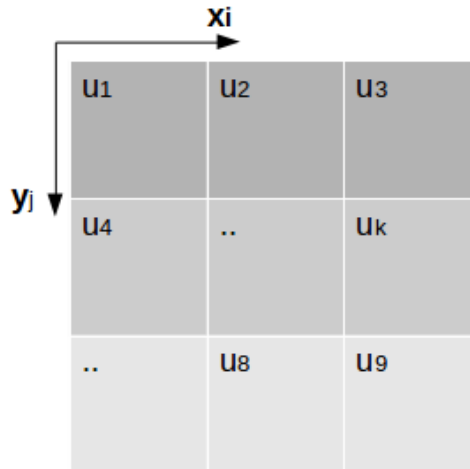


Figure 38: Mapping of the grid

The indices of the previous grid were transformed with $k = (i - 1) \cdot n_x + j$. This transformation leads to a $(n_x \times n_y) \times (n_x \times n_y)$ dimensional set of linear equations

$$A_{l,k} \cdot \Phi(u_k) = \frac{N_{u_k} \cdot q}{\epsilon} := f_l. \quad (3.7)$$

Independent on the size of the grid in x or y direction, a square matrix $A_{l,k}$ is always obtained within this transformation. Without proof, by inserting the index transformation mentioned above into equation (3.6), one can see that $A_{l,k}$ is also a sparse matrix. This means that most of the elements in $A_{l,k}$ are zero and can be neglected for certain numeric algorithms. This reduces the number of iterations needed for convergence drastically, even though the transformation leads to a system of linear equations with higher dimensions.

For the numeric solution of equation (3.7), the Jakobi iteration method [46] was chosen, while considering $A_{l,k}$ as a sparse matrix

$$\Phi(u_k)^{n+1} := \frac{1}{A_{k,k}} \left(f_k - \sum_{l \neq k} A_{l,k} \cdot \Phi(u_l)^n \right). \quad (3.8)$$

$\Phi(u_l)^n$ is the solution of the n-th iteration, so for the first iteration an arbitrary starting vector was chosen. After convergence the potential $\Phi(u_k)$ was mapped back to $\Phi(x_i, y_j)$. The electric field was then calculated via:

$$\vec{E} = -\nabla\Phi = \begin{pmatrix} E_x \\ E_y \end{pmatrix} = - \begin{pmatrix} \frac{\Phi_{x_i, y_j} - \Phi_{x_{i-1}, y_j}}{\Delta h} \\ \frac{\Phi_{x_i, y_j} - \Phi_{x_i, y_{j-1}}}{\Delta h} \end{pmatrix} \quad (3.9)$$

To obtain the deviation from a straight line path of the proton traversing the electric field of the SSD, the solution of equation (3.9) was put into equation (2.22) to solve equation (2.20).

3.6.2 Geant4 simulation

Geant4 (Geometry and tracking) is a C++-language based, object oriented toolkit, which uses the Monte Carlo method for simulating particle transport in matter for a predefined experimental setup. It is commonly used for detector simulations in high energy physics experiments as well as for simulations needed for ion therapy. A detailed mathematical description of the Monte Carlo algorithm and physics models used by Geant4 can be found in [19].

Geant4 structure

The geometry and its physical composition and properties have to be set by the user. Electric as well as magnetic fields can also be assigned to different geometries. After setting up the geometry, all the relevant physical processes have to be chosen. Geant4 provides a large amount of different physical models needed for particle transport which are summed up in “physics lists”. But it also allows the user to use or add customized physical processes to those physics lists. For all the simulations the Geant4 “QGSP_BIC” list was chosen, which is commonly used for protons below 1 GeV [47]. The particles themselves are transported according to a rejection Monte Carlo algorithm [47], which will not be discussed within this thesis. This algorithm samples the

processes and the length between two steps at each step of the particles track. This is also done for secondary particles. The history (=track) of a particle and the tracks of its secondary particles is called an event. Each event is independent of the other events. The number of events per run defines the number of particles at the start of a certain setup of the simulation. Between different runs, the geometry of the setup can be changed.

Geant4 does not save data per default, so any geometry in the simulation can be assigned as a “sensitive detector”. Whenever a particle enters a sensitive detector, it produces a “hit”. This hit can be filled with information about the current status of the traversing particle (energy, momentum, position, etc.). Each hit is saved in a “hits collection”, which can be accessed later and stored on a hard disk. The data was stored in a ROOT format [37] and analyzed.

Particle gun

Geant4 produces particles at certain spots with a certain energy and momentum predefined by the user. Since the proton beam at MedAustron has a Gaussian shaped beam profile, a particle gun for Geant4, which produces a proton beam with a beam profile according to an internal MedAustron report [48], had to be created. The full width at half maximum of the proton beam in x and y direction was given for different proton energies and is depicted in Figure 39.

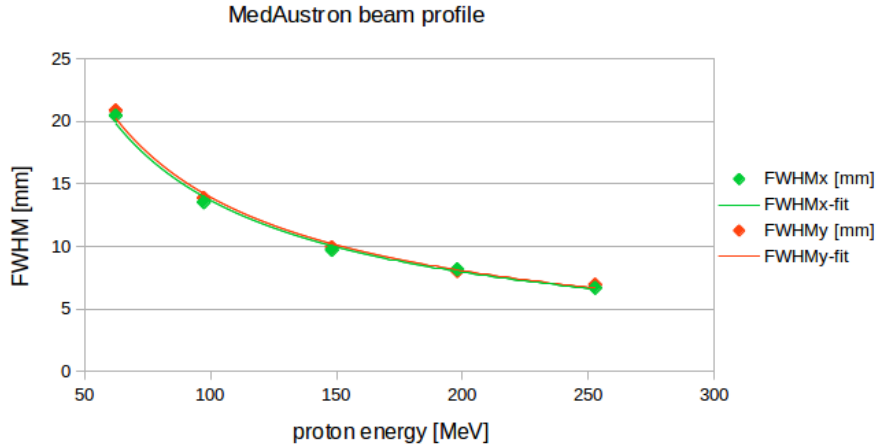


Figure 39: Beam profile at MedAustron

The particles starting position (x_i, y_i) was chosen randomly, but according to a normal distribution. For this purpose the Box–Muller transform was used [49]. This method creates two standard normally distributed random number (z_1, z_2) , using two uniformly distributed random numbers r_1, r_2 , with a mean $\mu = 0$ and a standard deviation $\sigma = 1$. The Box-Muller method reads as follows:

$$z_1 = \cos(2\pi r_2) \cdot \sqrt{-2 \ln r_1} \quad (3.10)$$

$$z_2 = \sin(2\pi r_2) \cdot \sqrt{-2 \ln r_1} \quad (3.11)$$

In order to get normal distributed numbers (x_i, y_i) with a mean μ and a standard deviation of σ , the standard normally distributed numbers z_1 and z_2 have to be transformed as

$$x_i = \mu + \sigma \cdot z_i. \quad (3.12)$$

The mean μ was chosen to be 0, since all experiments were conducted with a centered beam. The standard deviation was taken from Figure 39, with $\text{FWHM} = 2\sqrt{2\ln 2} \cdot \sigma$ for a normal distribution.

Geometry optimization of the pCT setup

Within the Geant4 simulation, the geometry of the beam telescope had to be optimized. The telescope consists of 4 SSDs, which dimensions were chosen according to Section 3.6. A 2×4 LEGO brick [50] (16 mm \times 32 mm \times 9.6 mm) was used as a phantom and placed in the middle of the telescope (Figure 40).

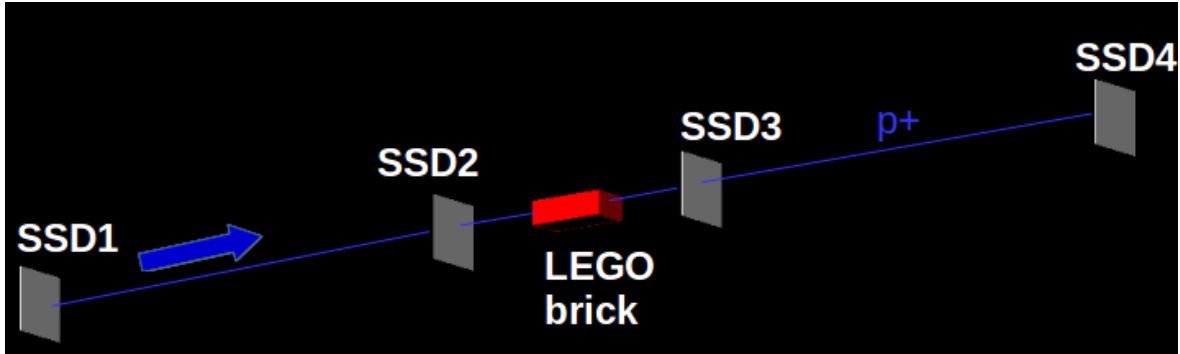


Figure 40: Geant4 simulation of a pCT setup

The first SSD (SSD1 in Figure 40) was positioned 3 cm behind the isocentre of the beam. The distance from the phantom to the adjacent SSDs was ± 6 cm and held constant. The distance z_{14} between the last and first SSD was varied between 30 and 200 cm. For each z_{14} , the number of particles detected with SSD4, in relation to the total number of particles entering a plane at $z = z_{14}$, perpendicular to the axis of the telescope, was recorded. This allowed to obtain the maximum distance z_{14} at which the whole beam could be detected with SSD4. The telescope setup was simulated for 62.4, 97.4, 148.2, 198 and 252.7 MeV.

The effect of placing one of the larger plastic scintillators (5 cm \times 5 cm \times 1 cm), described in section 3.2.3, in front of the telescope was also studied. The scintillator was placed in the isocentre of the beam and the telescope was positioned 3 cm behind the scintillator. This simulation allowed to obtain a decision whether the trigger unit had to be placed in front or behind the telescope. Again, z_{14} was varied between 30 and 200 cm. Also 62.4, 97.4, 148.2, 198 and 252.7 MeV were simulated.

3.6.3 Module testing

6 identical double-sided SSDs were provided by HEPHY. The functionality of each module had to be tested and the best four were used for the pCT telescope. To test the performance of each module, a Sr-90 source was placed on a pinhole aperture, above a module (Figure 41). Both small plastic scintillators were placed under the module. The coincident signal of both PMTs was used as a trigger signal for the APVDAQ system. A NIM trigger logic module from HEPHY was used as a trigger unit.

The circular pinhole leads to a gaussian beam profile of the Sr-90 beam. The shape of this beam was measured with each module and the quality of each measured profile was compared.

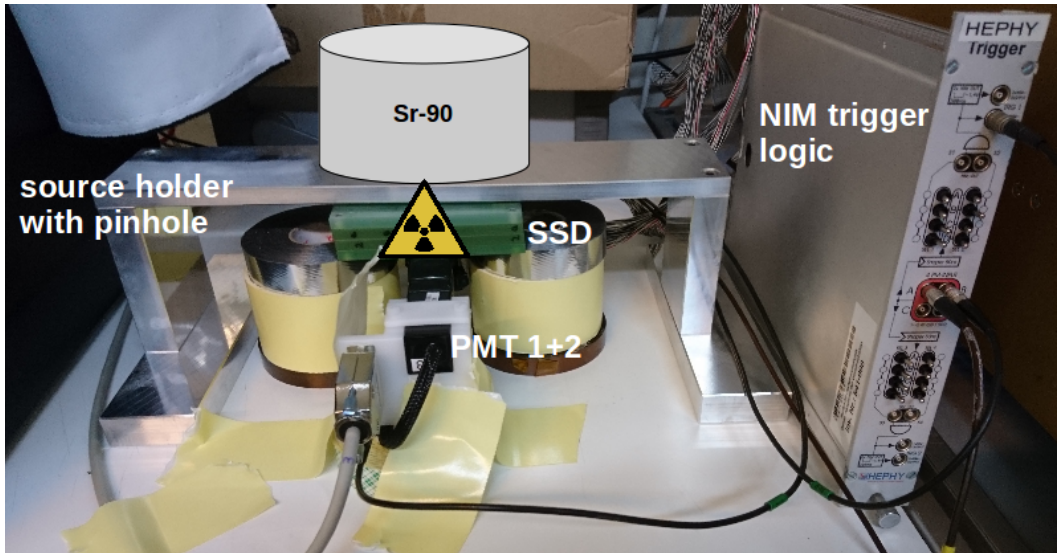


Figure 41: Module testing with Sr-90

The best four modules were then used for the pCT beam telescope. Before using all four SSDs at MedAustron, the functionality of the whole telescope was tested by measuring cosmic myons at HEPHY. For this purpose one of the PMTs was placed in front of all four modules and the second one behind the modules. This had to be done in order to have a myon, which has gone through all four modules, as a trigger signal. The telescope setup was facing towards the sky in order to measure the tracks and the beam profile of the cosmic myons. The myon setup is depicted in Figure 42.

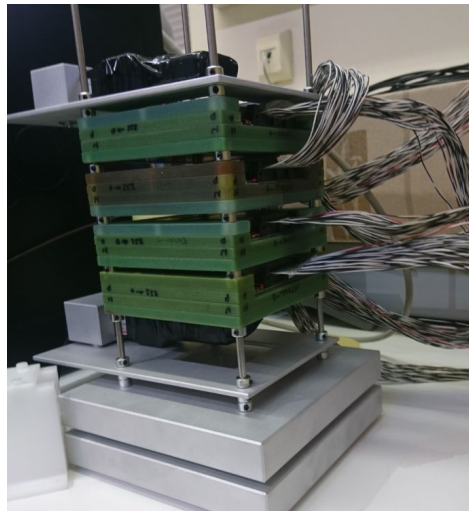


Figure 42: Telescope testing with cosmic myons

3.6.4 pCT setup at MedAustron

To test the functionality of the whole pCT beam telescope for future pCT setups, the scattering power of two different phantoms was measured with the telescope. For this purpose a rotating table, controlled with a Raspberry Pi 3+ was mounted between

the two middle SSDs. Each phantom was placed on the rotating table and irradiated separately at different rotational angles. One phantom was a 2×4 Lego brick and the second was a custom made PMMA (plexiglass) cube “PhanDuc” with holes and indentations on one side.

The distance between the first and last SSD was 52 cm. As a trigger logic unit for the APVDAQ system, the PCTS was used. For this purpose, the two bigger scintillators were placed behind the SSDs. The whole beam telescope setup is shown in Figure 43.

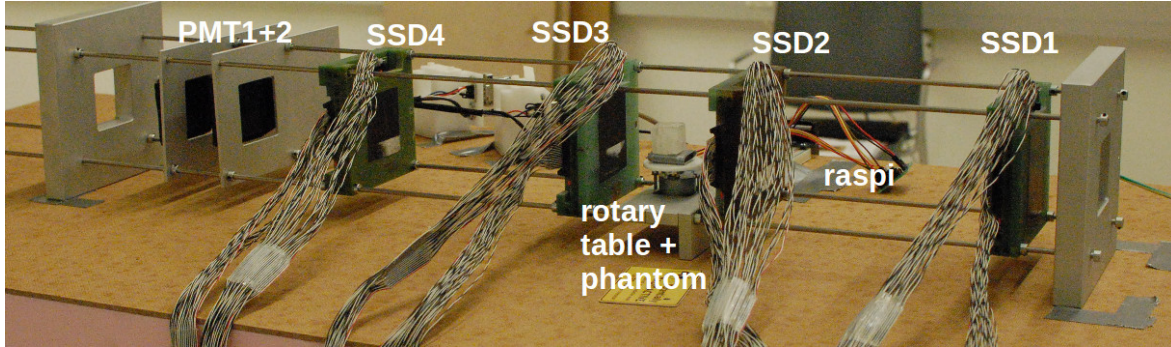


Figure 43: Beam telescope setup at MedAustron [31]

Raspberry Pi rotating table

A 28BYJ-48 stepping motor with a ULN2003 driver board were controlled remotely (SSH) via the Raspberry Pi 3+. This motor allows rotations with a stepsize down to 0.703125° . A C-based control software was written to control the rotational angle during the experiment.

PhanDuc phantom

The PhanDuc phantom was made from 5 PMMA slabs ($20 \text{ mm} \times 20 \text{ mm} \times 4 \text{ mm}$) put together, forming a $2 \text{ cm} \times 2 \text{ cm} \times 2 \text{ cm}$ cube. A 2 mm hole was drilled through all the slabs. Indentations arraigned like a stair were cut at the top of the cube. The dimensions of the PhanDuc phantom are depicted in Figure 44.

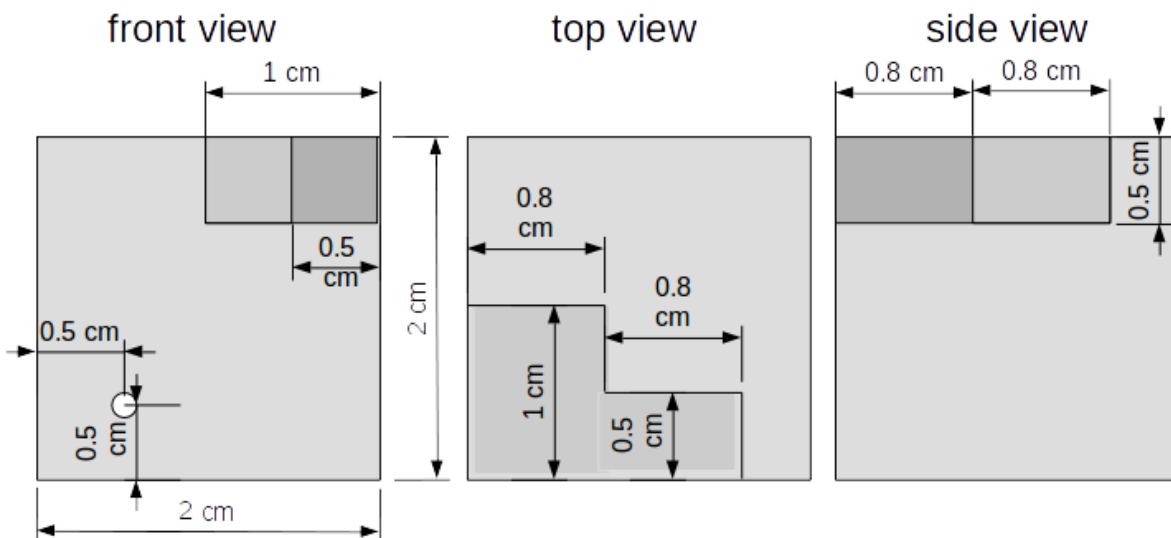


Figure 44: PhanDuc phantom

Geant4 simulation

The whole setup was also simulated in Geant4. The beam profile and the residual energy of a traversing proton was measured at every SSD within the simulation. The simulated beam profile, without a phantom and with a phantom was compared to the measured data at MedAustron.

The measurements at MedAustron and the Geant4 simulations were done for three different beam energies (100.4, 145.4 and 252.7 MeV).

4 Results and discussion

4.1 Particle flux reduction

4.1.1 Plateau curve measurements

Before using the PMTs for the PCTS setup, the optimal control voltage for each PMT had to be found. For this purpose the plateau curves for three different scintillator arrangement are shown.

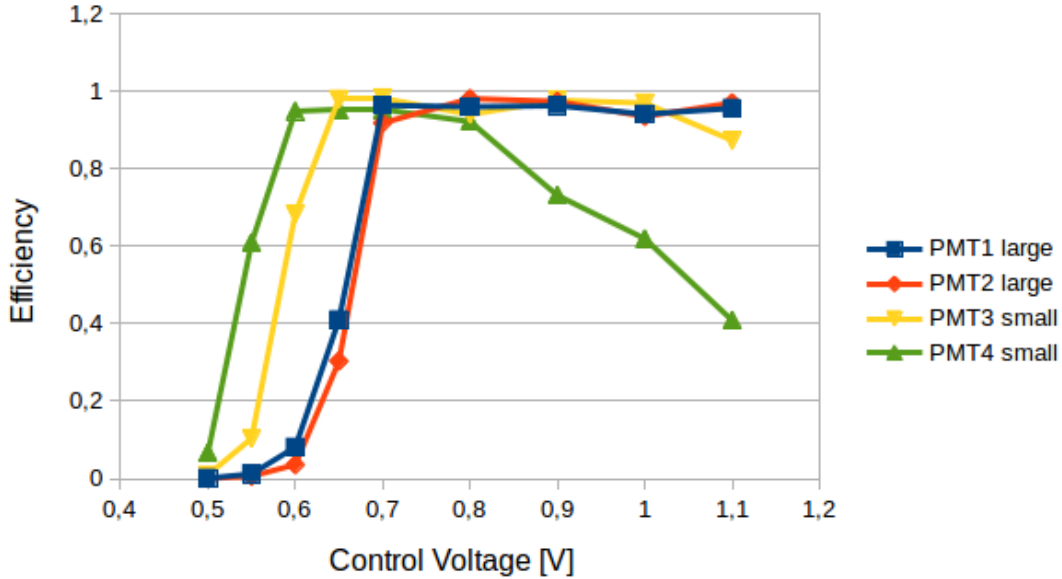


Figure 45: Plateau curve of all 4 PMTs

Figure 45 shows the plateau curve for a PCTS setup where all four PMTs are used. As can be seen, the small PMTs need lower control voltages for a higher efficiency than the bigger PMTs. The optimum control voltage for the small PMTs are 0.55 V for PMT4 and 0.65 V for PMT3. The plateau curve of the bigger PMT looks similar for PMT1 as well as for PMT2. The optimum control voltage for the bigger PMTs is 0.7 V.

By looking closer at the plateau curve of PMT4, a decrease in efficiency can be observed for higher control voltages. This is due to the fact, that at those high voltages, the power supply changed to an overcurrent state during irradiation and ramped down the supply and control voltage. This led to a decline in efficiency. It has to be mentioned, that those experiments were conducted without any flux reduction methods, so the scintillators were irradiated with a particle flux of 1×10^9 p/s. The results show that above 0.8 V PMT4 is not able to handle those high fluxes. Below those fluxes no overcurrent states appeared. Since all PMTs reached the plateau below 0.8 V, the obtained values for the optimum control voltage can be considered as valid.

Figure 46 shows the plateau curve for a PCTS setup where the two big PMTs were used. Again both plateau curves look similar. The optimum control voltages for both PMTs is 0.7 V. The decrease in efficiency due to a too high rate is only apparent above a control voltage of 1 V.

The plateau curves in Figure 47 describe the detector efficiency of the two smaller

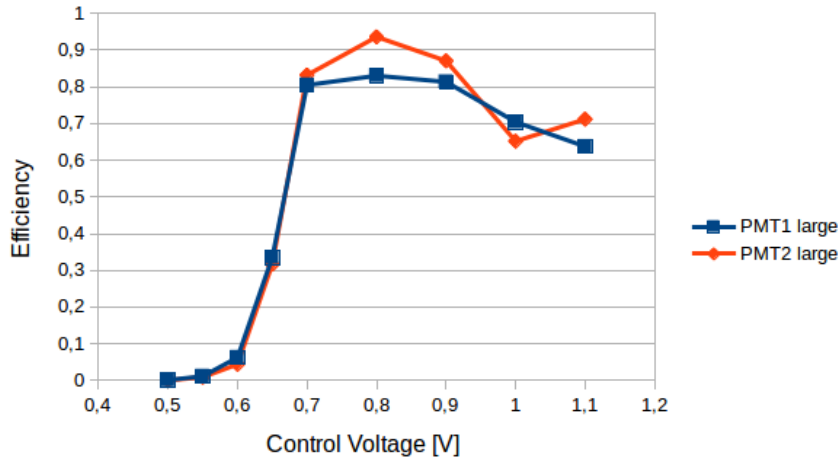


Figure 46: Plateau curve of the bigger PMTs

PMTs. The optimum control voltage for the small PMTs are 0.55 V for PMT4 and 0.65 V for PMT3.

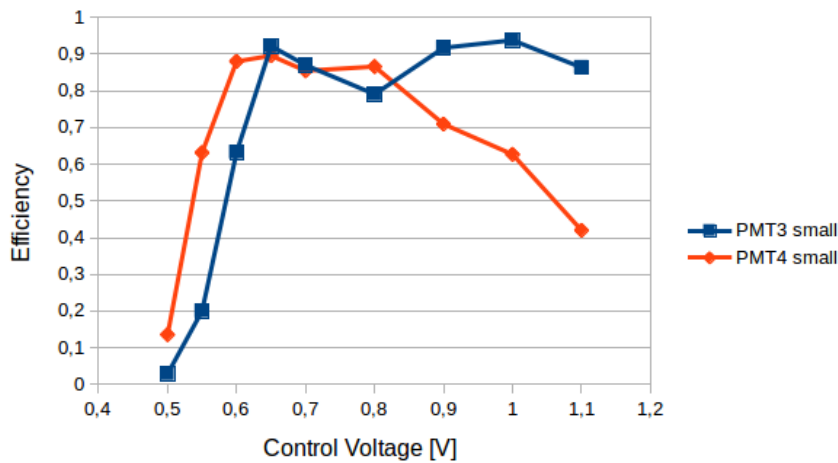


Figure 47: Plateau curve of the smaller PMTs

Since the detection efficiency of the two bigger PMTs is much more stable than the detection efficiency of the smaller PMTs and both big scintillators entail similar detection efficiency characteristics, PMT1 and PMT2 will be used for future pCT setups. The plateau curves also show, that it is important to reduce the particle flux, since the detectors needed for pCT cannot handle those high fluxes.

4.1.2 Beam geometry measurements

The beam profile was measured with the OCTAVIUS detector for three different particle flux reduction methods. In addition, two different beam energies were used (62.4 and 252.7 MeV). At 62.4 MeV, the chopper strength was varied while using the lowest rate. As an example, the obtained beam profile for the lowest rate is depicted in Figure 48a - 49b. The beam profile was measured at the isocentre and 109.65 cm behind the isocentre (=back position).

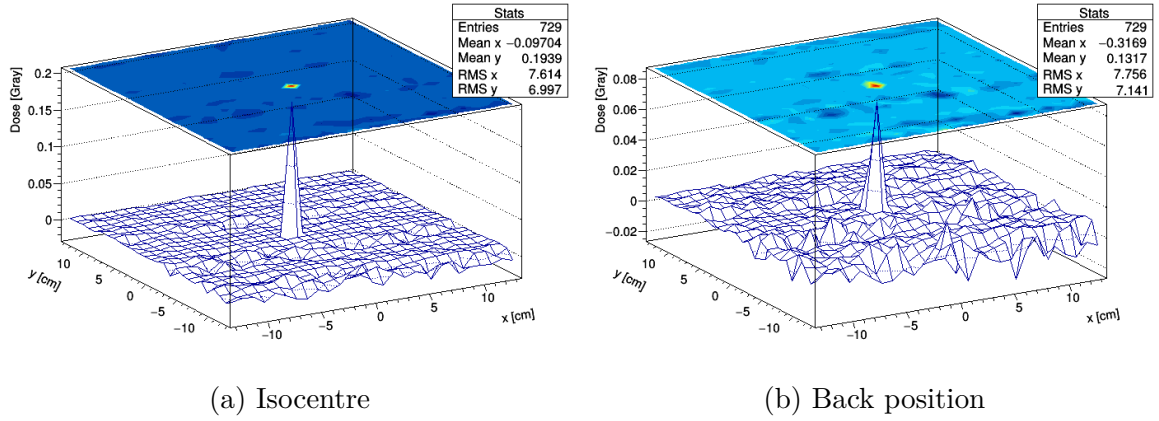


Figure 48: Beam profile at 252.7 MeV

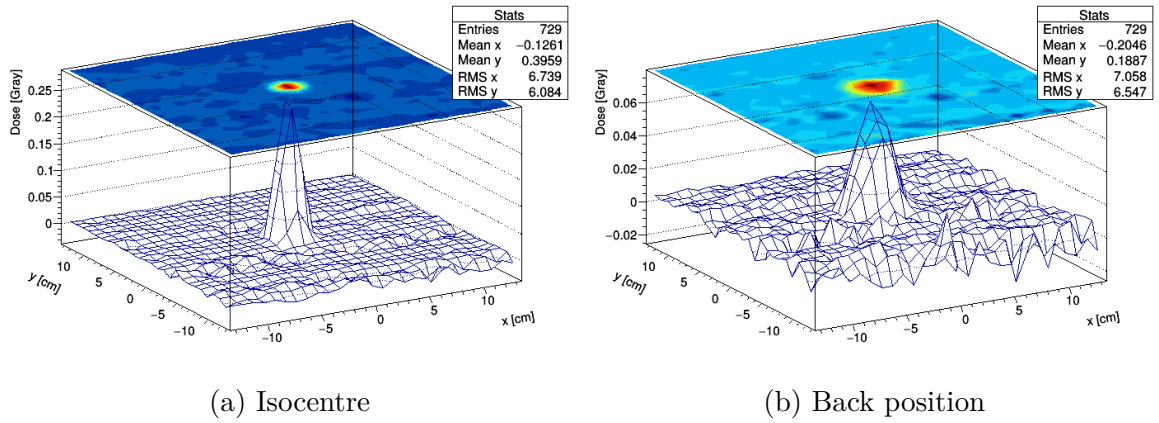


Figure 49: Beam profile at 62.4 MeV

The obtained beam profiles were analyzed in ROOT and a 2D Gaussian fit was applied to the beam profiles (Figure 50). The results of the fits are shown in Table 2 - 5 and were compared to the beam geometry without any flux reduction (Table 1).

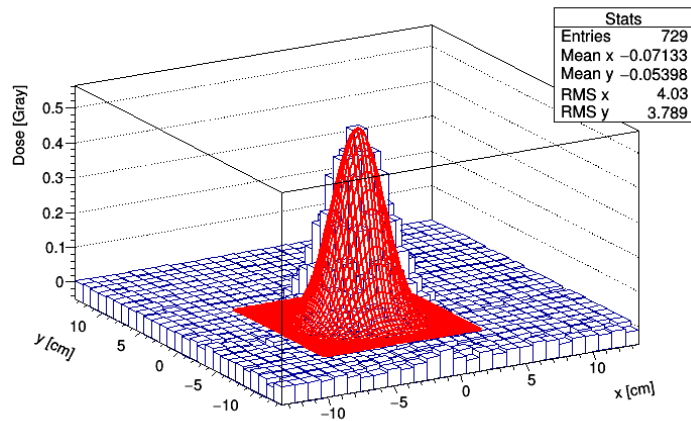


Figure 50: ROOT 2D Gaussian fit

Energy	FWHMx [cm]	FWHMy [cm]
252.7 MeV	0.668	0.693
198 MeV	0.816	0.802
148.2 MeV	0.971	0.992
97.4 MeV	1.353	1.388
62.4 MeV	2.048	2.088

Table 1: Isocentre, no flux reduction [48]

Method	FWHMx [cm]	FWHMy [cm]	Dose [Gy]
Betatron only	0.825	0.856	2.038
Beta + EFE	0.806	0,830	1.333
all 3	0.632	0.772	0.326

Table 2: Isocentre at 252.7 MeV

Method	FWHMx [cm]	FWHMy [cm]	Dose [Gy]
Betatron only	1.3	1.346	0.943
Beta + EFE	1.3	1.344	0.890
all 3	1.042	1.298	0.371

Table 3: Back Position at 252.7 MeV

Method	FWHMx [cm]	FWHMy [cm]	Dose [Gy]
Betatron only	2.178	2.232	2.331
Beta + EFE	2.082	2.15	1,540
all 3, Chopper 1.3	2.141	2.205	0.350
all 3, Chopper 1.4	2.036	1.966	0.731
all 3, Chopper 1.477	1.873	1.918	0.489

Table 4: Isocentre at 62.4 MeV

Method	FWHMx [cm]	FWHMy [cm]	Dose [Gy]
Betatron only	4.105	4.091	1.234
Beta + EFE	4.099	3,99	1.383
all 3, Chopper 1.477	3.604	3.29	0.469

Table 5: Back Position at 62.4 MeV

As can be seen in Table 4 and Table 2, the dimensions of the fitted beam profile at the isocentre are similar to the beam profile at the isocentre obtained with no flux reduction methods (Table 1). The deviation at the isocentre for 252.7 MeV is due to the fact, that the spatial resolution of the OCTAVIUS is maximum 1 cm. It can only be said, that the FWHM for 252.7 MeV at the isocentre is below 1 cm.

For a isocentre measurement at 62.4 MeV, the chopper strength was also varied, while using the lowest rate. By looking at Table 4, the effect of the chopper on the beam

geometry is clearly visible.

The measurements at the back position were taken to show, that the beam is centered and straight. It can also be said, that the beam profile stays Gaussian for all three particle flux reduction methods. The flux reduction is also apparent, when looking at the obtained dose per spill (=intensity). For a constant spilltime, the relative intensity decreases, the more particle flux reduction methods are used.

The size of the beam is always smaller than the area of the bigger scintillators (for both energies and all reduction methods). So the bigger scintillators are suitable for experiments where the flux reduction methods are used.

4.1.3 Particle flux measurements

After guaranteeing that the geometry of the beam does not change too much when using the particle flux reduction methods, the particle flux was measured for three different methods.

normal medical mode:	1×10^9 p/s
Betatron only:	1×10^7 - 1×10^8 p/s
Betatron+EFE:	1×10^6 - 1×10^7 p/s
Betatron+EFE+Chopper:	1×10^4 - 1×10^5 p/s

Table 6: Particle flux reduction methods

As can be seen in Table 6, particle fluxes down to 1×10^4 - 1×10^5 p/s could be measured.

Simultaneously to the flux measurement, the PMT signal of a smaller scintillator was monitored with an oscilloscope. For the lowest two particle flux measurements the amplitude of the PMT signal stayed relatively constant and hardly any pile-up effects and therefore no overcurrent states were observable.

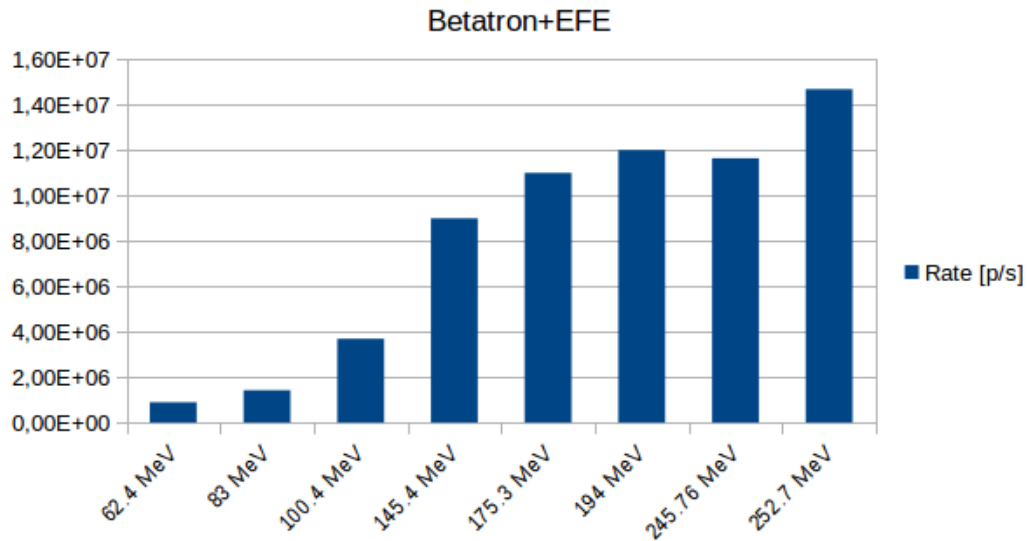


Figure 51: Energy dependence of the Betatron+EFE method

In addition, the energy dependence on the Betatron + EFE flux reduction methods was measured for 8 different energies and is depicted in Figure 51. By looking at Figure 51, a flux variation of 2 orders of magnitude can be seen. Those high fluctuations need to be further analyzed for applications which require a constant flux. However, pCT setups do not require a perfectly stable flux, but a flux with which single proton counting is manageable for the particle detectors. Those fluxes should not exceed 1×10^6 p/s, so the flux reduction method with the lowest rate entails perfect particle fluxes for pCT applications.

4.2 Beam telescope for pCT

The second part of this thesis describes the simulation and optimization of a beam telescope for pCT. The results of the simulation and conducted experiments will be shown in the following.

4.2.1 Electric field calculation

The electric field in the double-sided SSD was calculated. The electric potential of the whole p-side is depicted in Figure 52.

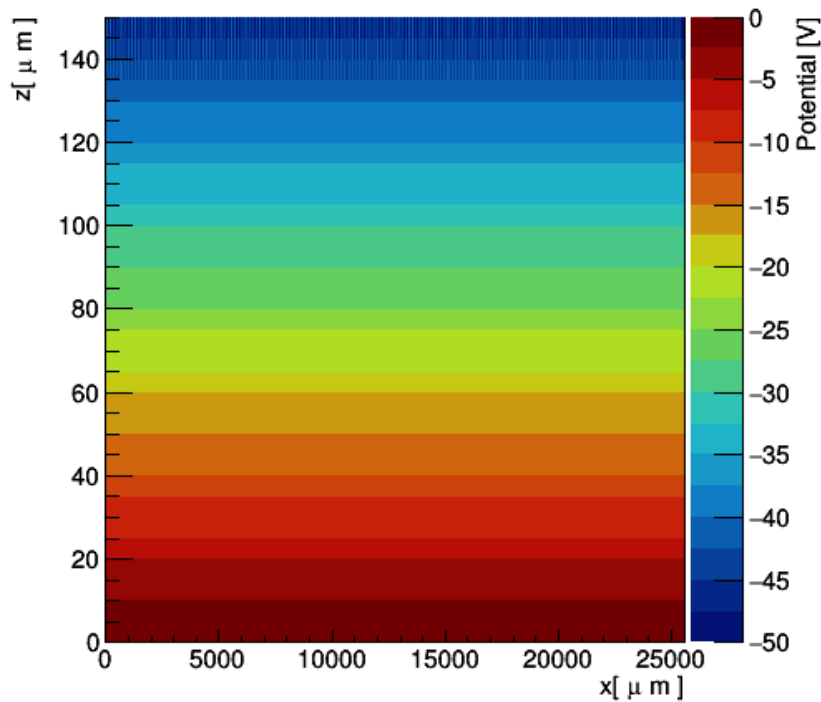


Figure 52: Calculated potential of the whole detector, p-side

By looking at Figure 52, a constant electric potential along the x -axis (horizontal), for each z -value is observable. This means that the electric field is constant along the beam telescope axis (z -axis) throughout the whole detector. Also after zooming (Figure 53a and Figure 53b) a relatively constant electric field along the z -axis can be assumed for the p-side. Only $\sim 10 \mu\text{m}$ in the surroundings of the strips, the electric field has a non-zero component in x -direction.

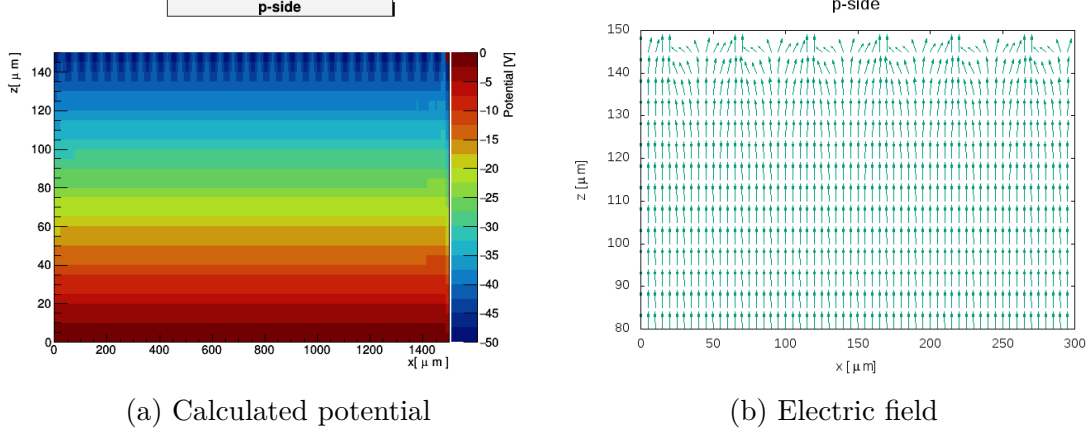


Figure 53: p-side zoom

Also by looking at Figure 54a and Figure 54b, where the n-side is shown, a constant field along the z -axis can be assumed. However, in the vicinity ($\sim 20 \mu\text{m}$) of the n-strips and p-stops, the electric field also has a non-zero component in y -direction.

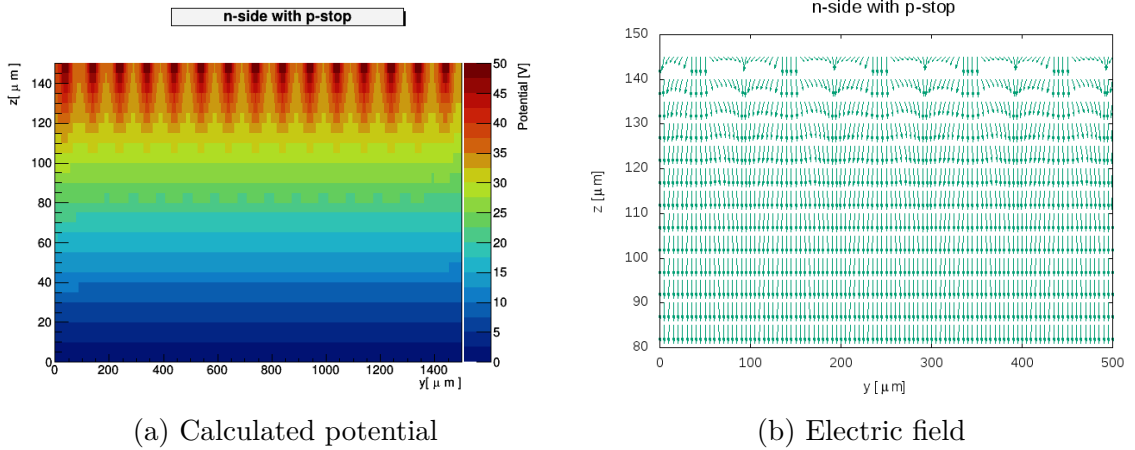


Figure 54: n-side zoom

The effect on the proton path was calculated for two scenarios. First it was calculated for a constant electric field along the z -axis and no electric field along the x - and y -axis. Since this is true for a large part of the detector, this simplification can be used as an approximation for the whole detector. For the whole SSD a mean electric field of $301.473 \frac{\text{kV}}{\text{m}}$ in the z -direction was obtained. This value is similar to the electric field of an ideal plate capacitor with $E = \frac{U}{d} = \frac{100 \text{ V}}{300 \mu\text{m}} = 333.333 \frac{\text{kV}}{\text{m}}$.

The electric field was inserted in equation (2.22) and then into equation (2.26) to obtain the proton path difference in the direction orthogonal to the z -direction. This was done for kinetic energies E_{kin} between 62.4 and 252.7 MeV. The relativistic velocity was calculated according to equation (4.1), with c as the speed of light and m_0 as the mass of the proton

$$v = c \cdot \sqrt{1 - \left(\frac{E_{kin}}{m_0 c^2} + 1 \right)^{-2}}. \quad (4.1)$$

A path difference of $\sim 1 \times 10^{-11} \text{ m}$ was obtained for all energies. This means that the electric field of the SSDs along the beam telescope axis can be neglected for pCT

simulations.

The effect of the non-zero component of the electric field in the vicinity of the strips was then calculated. Near a n-strip, a mean electric field $\vec{E} = \begin{pmatrix} E_x \\ E_z \end{pmatrix} = \begin{pmatrix} 268.075 \\ 198.107 \end{pmatrix} \frac{kV}{m}$ was calculated. This electric field was also inserted in equation (2.22) and then into equation (2.26). A path difference between $\sim 1 \times 10^{-12}$ and 1×10^{-13} m was obtained for the energies mentioned above. Also for a non-zero electric field near the strips, no significant change in the proton path was observable.

This means that the electric field of the SSDs can be neglected for pCT simulations. Only for the signal generation and signal shape in the SSDs it has to be considered, but it will not affect the proton path significantly.

4.2.2 Geometry optimization of the pCT beam telescope

The beam telescope length and particle energy was varied with Geant4. In Figure 55, the amount of particles which the last SSD could measure is depicted for different beam telescope lengths.

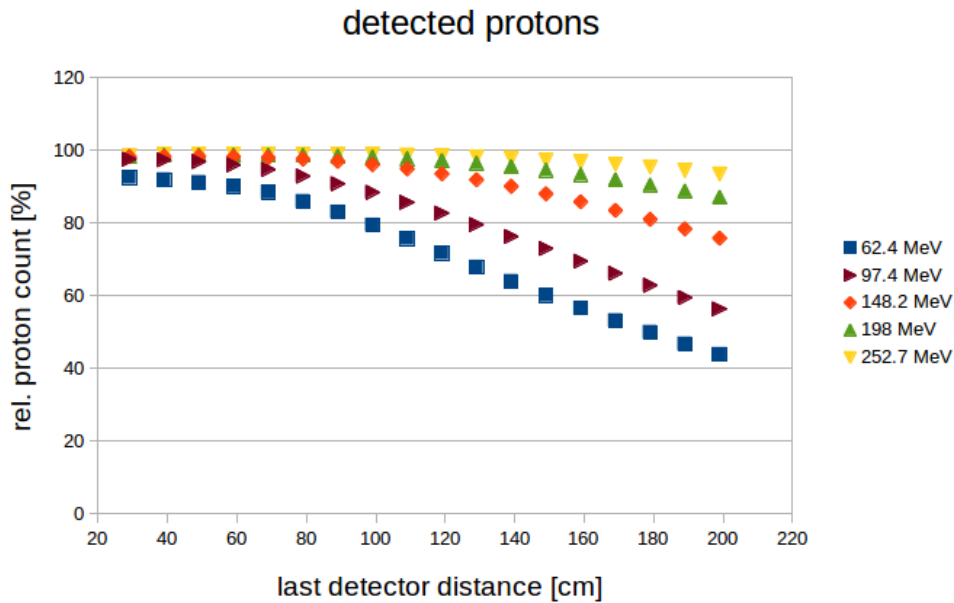


Figure 55: Beam telescope length without a scintillator in front

Figure 55 shows, that up to a beam telescope length of 80 cm, most of the proton beam can be captured. For 62.4 MeV, the size of the beam at SSD4 always seems to be bigger than the area of the SSD ($2.56 \text{ cm} \times 2.56 \text{ cm}$), therefore not all particles can be detected. This is due to the fact that lower energetic protons undergo multiple coulomb scattering with higher scattering angles on average than higher energetic protons. Also the beam size at the isocentre ($\text{FWHM} = 2.1 \text{ cm}$) is almost as big as the width of the SSD.

By looking at Figure 56, the effect of a scattering medium (1 cm of plastic scintillator) in front of the beam telescope can be seen. Especially for lower energies, the

amount of captured particles for different beam telescope lengths is much less than without a scintillator in front of the beam telescope.

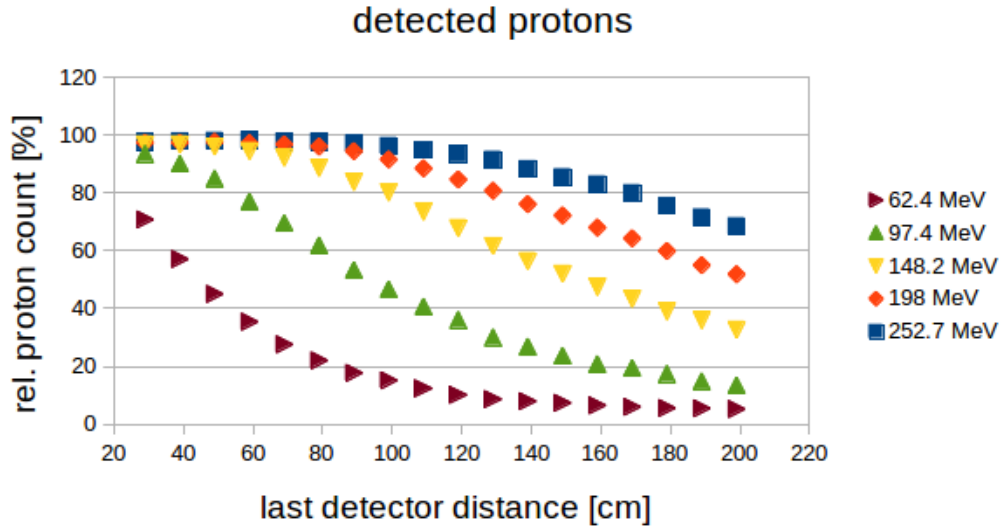


Figure 56: Beam telescope length with a scintillator in front

Those results led to the decision to put both scintillators behind the beam telescope. Since the APVDAQ system saves the hits in a buffer, this “triggering in the past” is possible. The trigger signal only has to be synchronized to the APVDAQ readout mechanism.

According to the previously mentioned results, the pCT beam telescope length was chosen to be 52 cm for the first experimental test at MedAustron to allow an optimum particle detection.

4.2.3 Module testing at HEPHY

All 6 different SSD modules ATOLL-1, ATOLL-2, COMM-1, COMM-2, COMB-1, and COMB-2 were irradiated with a Sr-90 source at HEPHY. Since the Sr-90 source was mounted above a circular pinhole, a Gaussian shaped beam profile should be obtained from each module. The hitmaps, consisting of 10000 events were recorded with the APVDAQ system and stored for each module. Those hitmaps are depicted in Figure 57a - Figure 62a:

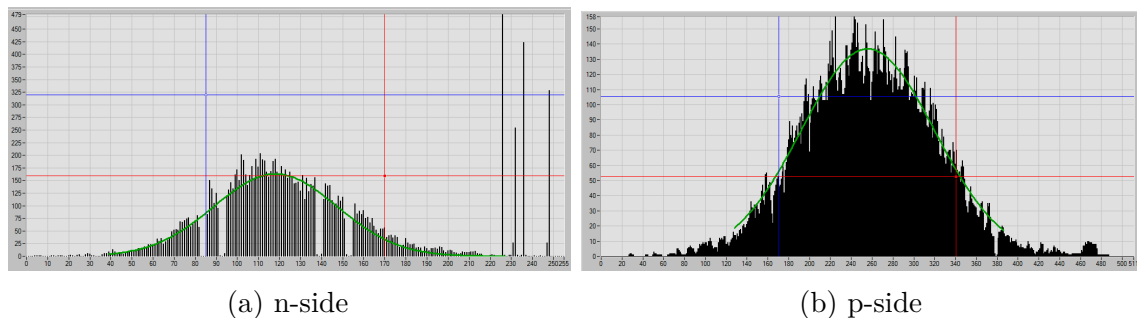
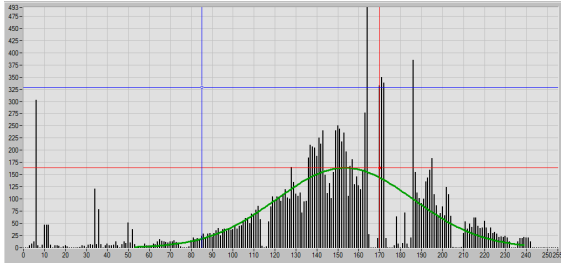
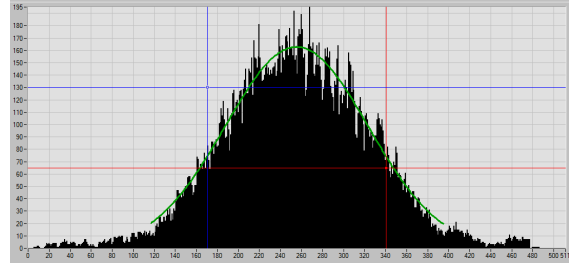


Figure 57: ATOLL-1 hitmap

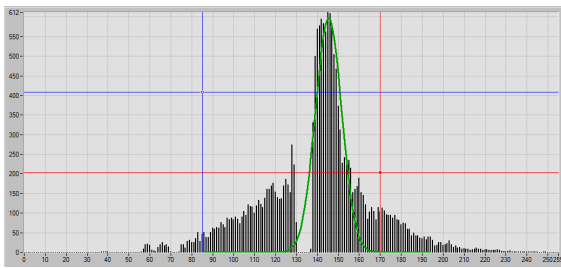


(a) n-side

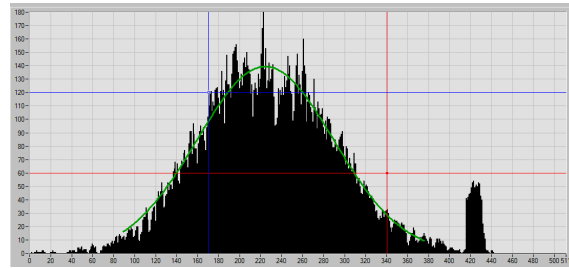


(b) p-side

Figure 58: ATOLL-2 hitmap

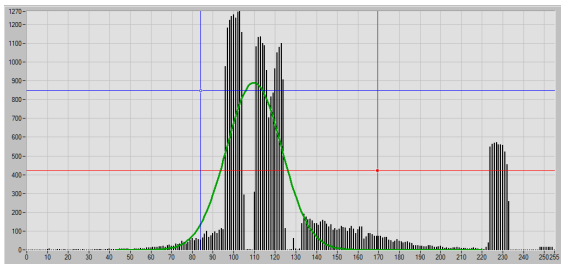


(a) n-side

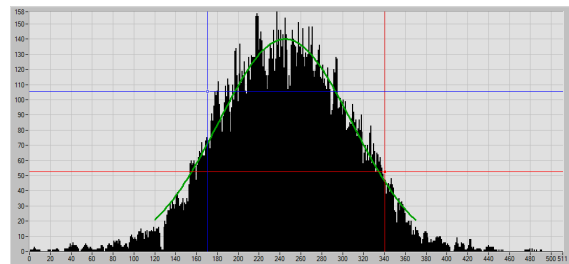


(b) p-side

Figure 59: COMB-1 hitmap

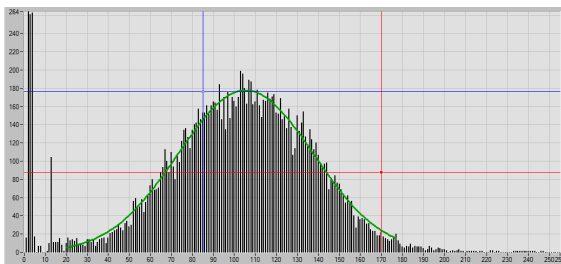


(a) n-side

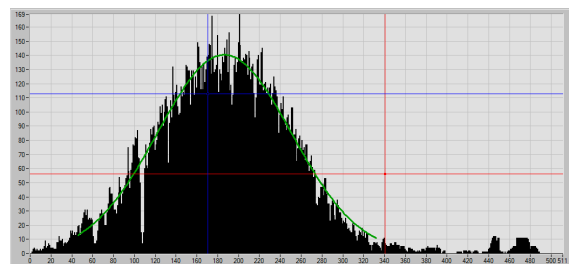


(b) p-side

Figure 60: COMB-2 hitmap



(a) n-side



(b) p-side

Figure 61: COMM-1 hitmap

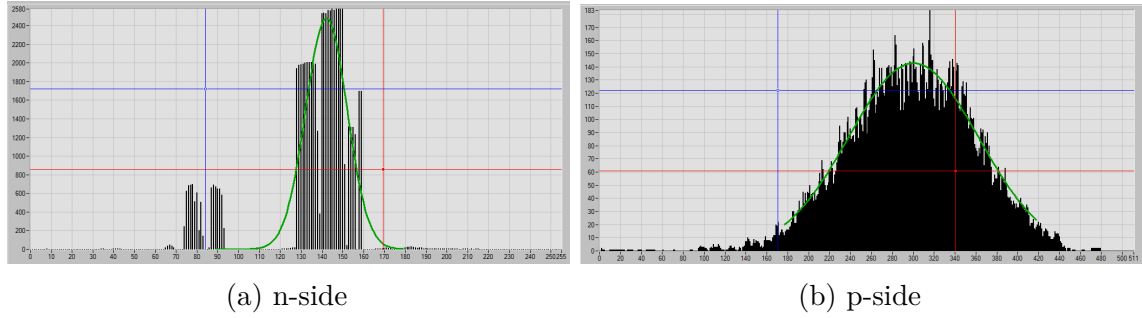


Figure 62: COMM-2 hitmap

By looking at the beam profiles of all 6 SSDs, the performance of each SSD could be evaluated. Almost all p-sides could capture a nice Gaussian shaped beam profile. Only the p-side of COMB-1 seems to have bad strips near the border.

The performance of the n-sides differed drastically from the performance of the p-sides. Only COMM-1 and ATOLL-1 could measure the full Gaussian beam profile. The Gaussian shape could almost be fully observed with ATOLL-2. This SSD however had bad strips near its center.

Since the performances of the n-sides of COMM-2 and COMB-2 were significantly worse in comparison to the other four SSDs, COMB-1 was chosen as the fourth best SSD.

Therefore COMM-1, ATOLL-1, ATOLL-2 and COMB-1 were chosen for the pCT beam telescope.

Myon-run at HEPHY:

Those four SSDs were used to measure cosmic myons with the small scintillators as a trigger unit. A captured myon track is depicted in Figure 63 to demonstrate a proof of principle.



Figure 63: Track of a cosmic myon

4.2.4 pCT beam telescope measurements at MedAustron

After simulating, optimizing and testing the beam telescope setup, the scattering power of the PhanDuc phantom and a LEGO brick were measured with the beam telescope

setup. This should serve as a proof of principle that the beam telescope setup can be used for future pCT setups. All three phantoms were irradiated with protons with 145.4 MeV at MedAustron. In addition the experimental setup was simulated in Geant4 and the obtained beam profiles were compared to the experimental results.

The phantoms were rotated with the Raspberry Pi rotary table and irradiated at different angles. The results will only be shown for a rotational angle of 0° since no calorimeter could be used and therefore a full pCT reconstruction was not possible.

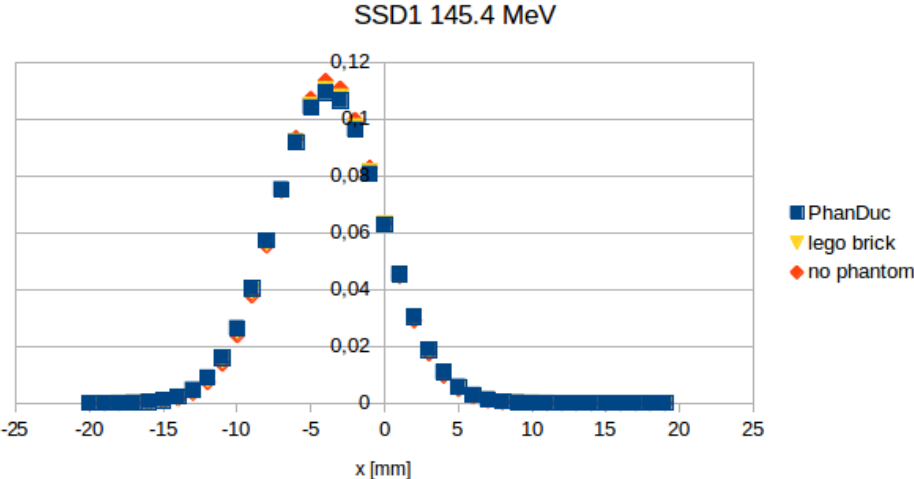


Figure 64: Fitted beam profiles for different phantoms at SSD1

Figure 64 shows the beam profile obtained with SSD1 at the isocentre. Since the phantom was placed behind SSD2, the beam profile did not change for all three runs at this position. A slight offset in x-direction is apparent even though the setup was aligned with the help of positioning lasers. This slight deviation has to be taken into consideration for future pCT reconstruction methods. Therefore a suitable alignment algorithm for the beam telescope should be developed.

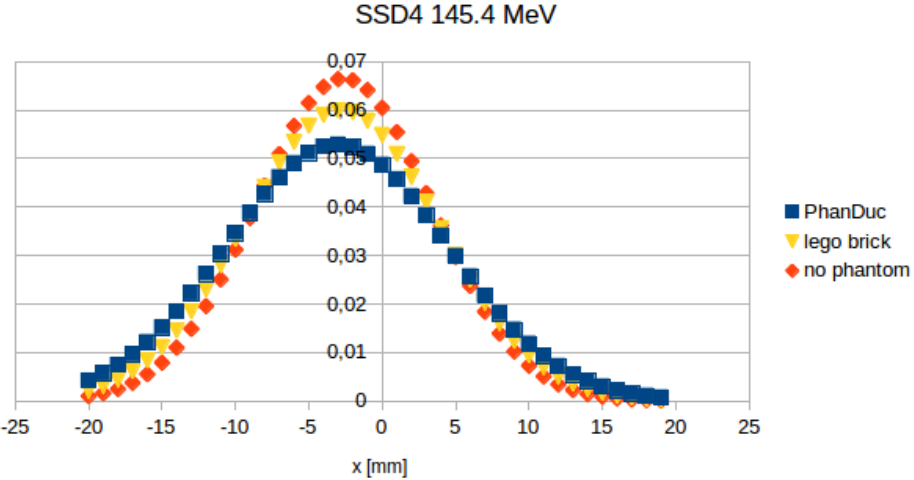


Figure 65: Fitted beam profiles for different phantoms at SSD4

By looking at Figure 65, beam broadening due to multiple Coulomb scattering in matter is apparent. Since the PhanDuc phantom consists of much more material than the LEGO brick, the effect of MCS is more obvious. As expected, the beam is the narrowest when no phantom is used.

Since the phantoms consist of more than one material, a distortion of the Gaussian shaped beam profile should be expected. For this purpose the experimental setup was simulated in Geant4 and compared to the measured beam profiles.

Figure 66a shows the simulated distorted beam profile at SSD3, after the beam has passed the LEGO brick. A big indentation, due to the top layer of the LEGO brick, is apparent at 0.4 cm. This indentation can also be seen at the measured beam profile (Figure 66b). Here, the indentation is not as clear as for the simulation. This might be due to the fact, that 1×10^6 particles were used for the simulation, whereas only 1×10^4 events were recorded for each configuration at MedAustron (APVDAQ readout rate < 100 Hz).

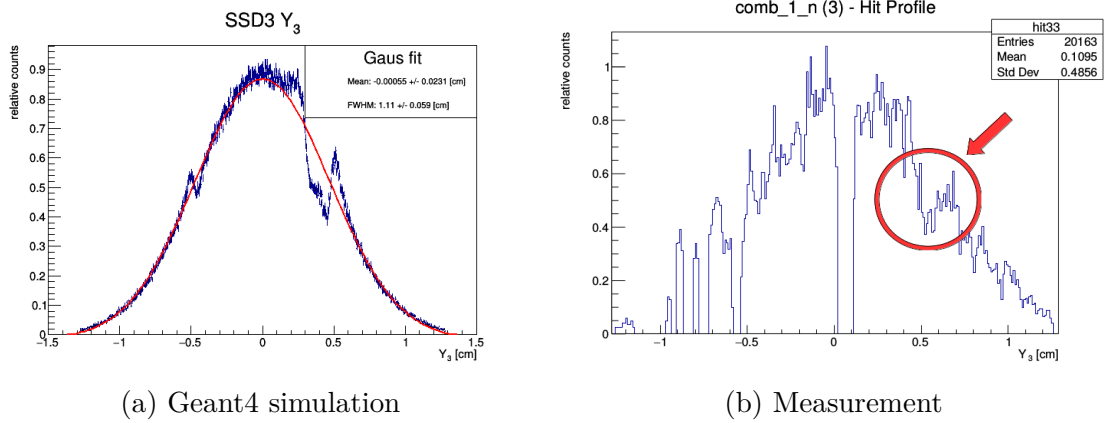


Figure 66: LEGO brick, y3 SSD3, 145.4 MeV

This distortion completely vanishes when the phantom is removed. By looking at Figure 67a and Figure 67b, an undistorted Gaussian beam profile can be seen.

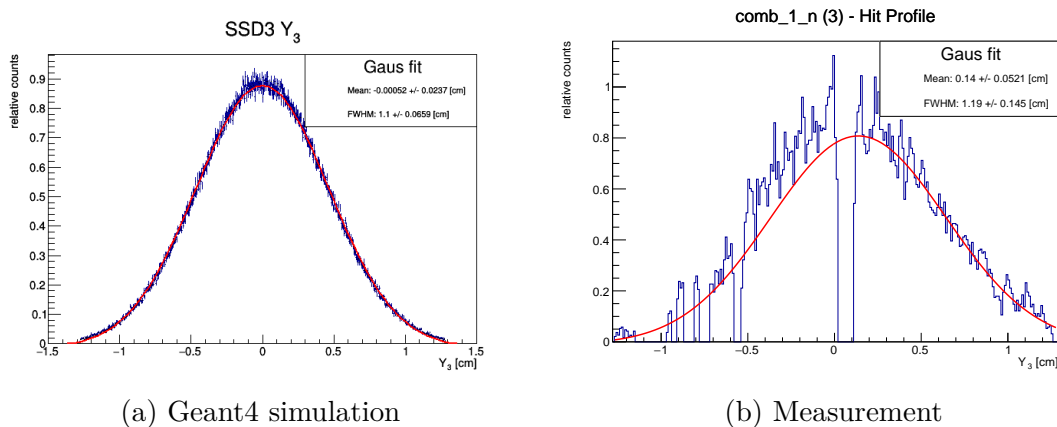


Figure 67: No phantom, y3 SSD3, 145.4 MeV

The results from the other beam telescope measurements are depicted in the Appendix

(Figure 70a- Figure 93b). The broadening of the beam profiles due to MCS seems to be more significant for all measurements in comparison to the simulated simulated beam profiles. This has to be further analyzed and adapted for future pCT simulations using Geant4.

Proton computed radiography simulation

Within the simulation of the beam telescope, a proton computed radiography was simulated in Geant4. This was done by measuring the residual kinetic energy of the proton at SSD3 after it has traversed the phantom.

Figure 68 shows a radiography of the PhanDuc phantom. The edges as well as the hole are clearly visible. Only the second step at the top is not recognizable.

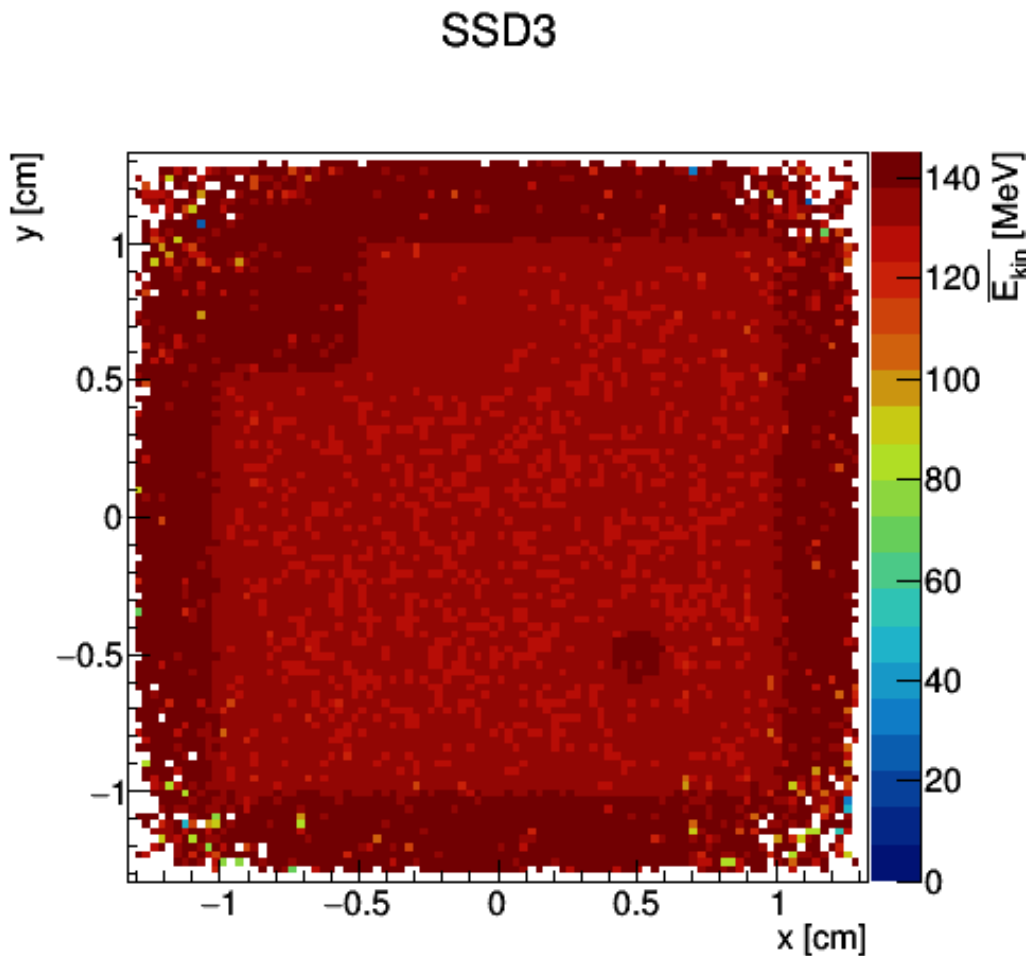


Figure 68: PhanDuc, proton computed radiography, 145.4 MeV

A radiography of the LEGO brick was also simulated. The residual kinetic energy of the proton beam at SSD3 is depicted in Figure 69. The contours of the LEGO brick are clearly visible.

Those radiography plots could be obtained with a calorimeter, which is a crucial part of a pCT setup. Together with the beam telescope a calorimeter would complete a

full pCT setup.

SSD3

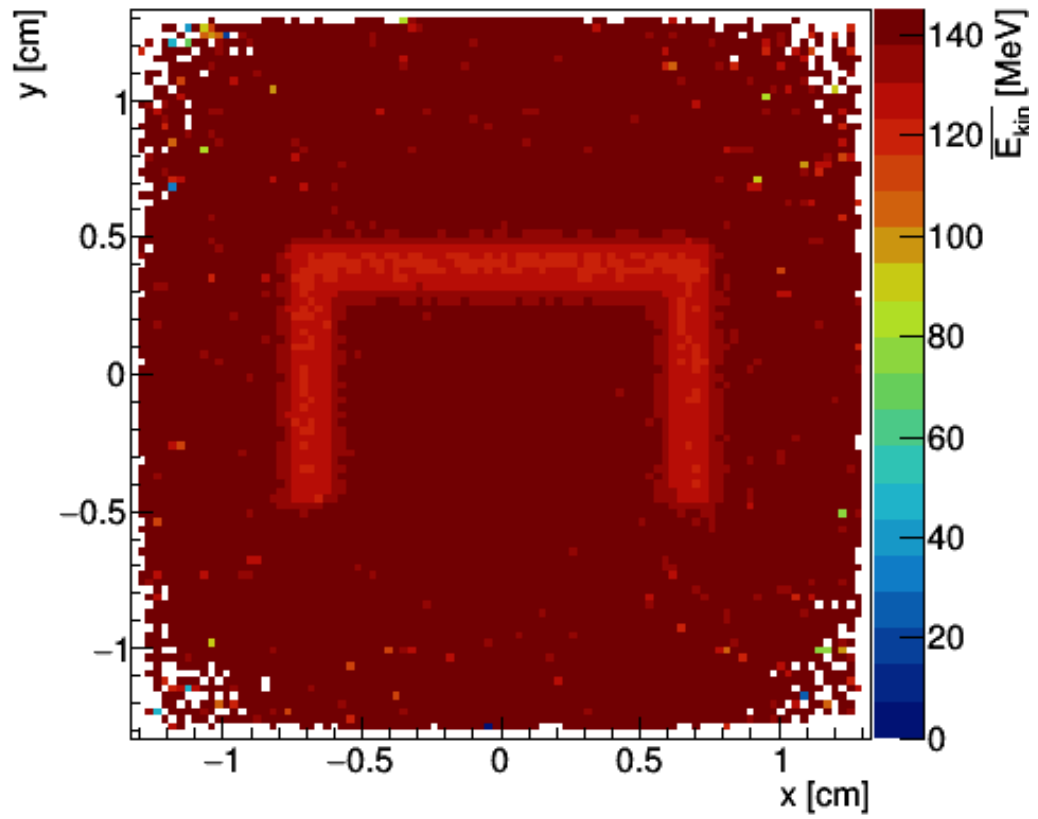


Figure 69: LEGO brick, proton computed radiography, 145.4 MeV

5 Conclusion and outlook

Within the scope of this master thesis a VME based particle counting and trigger system was developed and optimized. This PCTS system allowed to qualitatively analyze three new particle flux reduction methods provided by MedAustron. Particle rates down to 1×10^4 p/s could be observed and are now available at MedAustron for non-clinical research. Those low fluxes are necessary for pCT setups, since they should be able to manage single particle counting. Even the PCTS setup, with fast plastic scintillators, encountered problems with the high fluxes which are used for medical applications. Those problems were not observed with the low fluxes.

However, it has to be mentioned that those low fluxes are not perfectly stable, but stay constant in the order of one magnitude. Those fluctuations need to be further analyzed to improve the stability. An energy dependence on those fluctuations could also be observed with the PCTS.

Also the effect on the beam geometry was studied with the OCATVIUS ionization chamber array for all three particle flux reduction methods. Independent of the flux reduction method, the beam was always centered, straight and entailed a Gaussian beam profile. A similar beam geometry, in comparison to the normal extraction method, was obtained at the isocentre of the beam.

In addition, it was shown that the PCTS could successfully be used as a trigger unit for other detectors. So, it can be said that the new low particle fluxes and the PCTS setup form a good basis for future pCT setups.

Furthermore a beam telescope, consisting of four double-sided Silicon strip detectors, provided by HEPHY, was simulated, developed, optimized and tested experimentally. Within the preparatory calculations, it was demonstrated that the influence of the electric field of the SSDs on the protons trajectory can be neglected.

The results of the Geant4 simulations showed that the scintillators should be placed behind the silicon strip detectors in order to obtain a good detection efficiency. Also the length of the beam telescope was optimized.

Since a pCT setup needs to capture proton beams going through a phantom under various angles, a remotely controllable rotary table, controlled via a Raspberry Pi, was developed. The stepping motor and developed control software allow a stepsize of 0.703125° .

The functionality of this extended beam telescope setup for pCT was tested at MedAustron. Two different phantoms were irradiated and the proton beam was recorded at every SSD. The distorted beam profile, due to the material composition of the phantom, was compared to a Geant4 simulation of the beam telescope. The experimentally obtained distorted beam profiles showed similarities to the simulated beam profiles. However, for a better comparison, much more events per configuration need to be recorded in the future. It also has to be mentioned that the simulated beam profiles seemed narrower than the experimentally obtained beam profiles. Therefore the beam geometry and the multiple coulomb scattering algorithm in Geant4 have to be better understood. Also the used beam model is not optimal and has to be adapted to experimental data.

The simulations of a proton computed radiography offer a preview for future pCT images. Those simulated experiments could be recreated with a calorimeter, which would complete the pCT setup. Therefore, a calorimeter suitable for pCT at MedAus-

tron (it should be able to stop protons up to 800 MeV) has to be developed. With a complete pCT setup at MedAustron many other aspects of pCT could be analyzed in the future. The spatial resolution of pCT and its influencing processes, such as MCS, as well as the reconstruction algorithms should be studied and optimized. Also an optimal balance between the number of particles needed for pCT and the dose to patient has to be found.

6 Acknowledgements

First I would like to thank my colleague DI Alexander Burkner, whose programming expertise, hard work and chillies were essential for the success of the pCT project. He invested many hours into this project to write the control software for the PCTS setup and to provide the main framework for the VHDL gateware.

I also owe a lot of gratitude to Dr. Albert Hirtl, who has always been a driving force behind this project and always had our backs.

Furthermore I would like to thank all the staff members from HEPHY, without whom we would have never achieved that much. They provided us with their detectors, electronics and expertise and supported us in any possible way. Especially I need to thank Dr. Thomas Bergauer, who is another big driving force behind this project. He helped us with his deep understanding of particle detectors and provided us with an armada of experts.

I also like to thank DI Christian Irmeler, who patiently introduced us to the APVDAQ system. I am also very grateful for the help and enthusiasm from DI Peter Paulitsch, Dr. Manfred Valentan, Dr. Markus Friedl, DI Johannes Grossmann, DI Stefan Schultschik and all the other HEPHY members.

I also like to especially thank Dr. Andrea De Franco and Dr. Claus Schmitzer from MedAustron who provided us with their excellent expertise in accelerator physics.

Finally I would like to thank my family, my parents, my girlfriend Esther, for their patience and their loving support.

Appendix

List of Figures

1	Depth-dose profile of photons vs. ions [1]	4
2	Total stopping power for protons in plastic scintillators [7]	7
3	Geant4 Simulation of 100 MeV protons travelling through water [6]	8
4	Setup of a proton computed tomography	11
5	Interaction of protons with matter	11
6	Zig-zag path of a proton through a material of thickness x , undergoing multiple Coulomb scattering with a total scattering angle θ	12
7	Electron configuration of a plastic scintillator	15
8	Stokes Shift	15
9	Scintillator setup	16
10	Photomultiplier	16
11	Operation principle of a gaseous detector	17
12	Different operational modes of a gaseous detector [20]	18
13	pn-junction diode [21]	19
14	Diode Operating Modes [21]	19
15	Cross section of a single-sided Si-strip detector [21]	20
16	Double sided silicon strip detector [21]	20
17	proton passing a homogeneous electric field	21
18	MedAustron facility	25
19	Betatron oscillation	26
20	4 chopper magnets (blue) with a beam dump (grey)	27
21	Schematic drawing of a betatron	28
22	Schematic drawing of a FPGA with configurabel logic blocks (CLB), interconnect wires, I/O blocks (IOB) and a flash memory for the circuit design.	29
23	Particle counting and trigger setup	30
24	Scintillator	31
25	Leading edge discriminator	31
26	COSCAT FPGA design, G0, G1 are LEMO I/O ports	32
27	Example of a ModelSim-simulation of the Event Generator, Event Trigger and FIFO module	32
28	Asynchronous coincidence [31]	33
29	Coincidence PMT1 + PMT2 + PMT3 [31]	33
30	State machine of the Event Generator block	34
31	Plateau curve of a PMT	35
32	Plateau curve measurement setup [38]	36
33	Alignment of all four scintillators [38]	37
34	Octavius ionization chamber array [39]	37
35	Octavius measurement [38]	38
36	Particle flux measurement [38]	39
37	Double sided Silicon strip detector [38]	39
38	Mapping of the grid	41
39	Beam profile at MedAustron	43
40	Geant4 simulation of a pCT setup	44
41	Module testing with Sr-90	45
42	Telescope testing with cosmic myons	45
43	Beam telescope setup at MedAustron [31]	46

44	PhanDuc phantom	46
45	Plateau curve of all 4 PMTs	49
46	Plateau curve of the bigger PMTs	50
47	Plateau curve of the smaller PMTs	50
48	Beam profile at 252.7 MeV	51
49	Beam profile at 62.4 MeV	51
50	ROOT 2D Gaussian fit	51
51	Energy dependence of the Betatron+EFE method	53
52	Calculated potential of the whole detector, p-side	54
53	p-side zoom	55
54	n-side zoom	55
55	Beam telescope length without a scintillator in front	56
56	Beam telescope length with a scintillator in front	57
57	ATOLL-1 hitmap	57
58	ATOLL-2 hitmap	58
59	COMB-1 hitmap	58
60	COMB-2 hitmap	58
61	COMM-1 hitmap	58
62	COMM-2 hitmap	59
63	Track of a cosmic myon	59
64	Fitted beam profiles for different phantoms at SSD1	60
65	Fitted beam profiles for different phantoms at SSD4	60
66	LEGO brick, y3 SSD3, 145.4 MeV	61
67	No phantom, y3 SSD3, 145.4 MeV	61
68	PhanDuc, proton computed radiography, 145.4 MeV	62
69	LEGO brick, proton computed radiography, 145.4 MeV	63
70	LEGO brick, x1 SSD1, 145.4 MeV	78
71	LEGO brick, x2 SSD2, 145.4 MeV	78
72	LEGO brick, x3 SSD3, 145.4 MeV	78
73	LEGO brick, x4 SSD4, 145.4 MeV	79
74	LEGO brick, y1 SSD1, 145.4 MeV	79
75	LEGO brick, y2 SSD2, 145.4 MeV	79
76	LEGO brick, y3 SSD3, 145.4 MeV	80
77	LEGO brick, y4 SSD4, 145.4 MeV	80
78	PhanDuc, x1 SSD1, 145.4 MeV	80
79	PhanDuc, x2 SSD2, 145.4 MeV	81
80	PhanDuc, x3 SSD3, 145.4 MeV	81
81	PhanDuc, x4 SSD4, 145.4 MeV	81
82	PhanDuc, y1 SSD1, 145.4 MeV	82
83	PhanDuc, y2 SSD2, 145.4 MeV	82
84	PhanDuc, y3 SSD3, 145.4 MeV	82
85	PhanDuc, y4 SSD4, 145.4 MeV	83
86	No phantom, x1 SSD1, 145.4 MeV	83
87	No phantom, x2 SSD2, 145.4 MeV	83
88	No phantom, x3 SSD3, 145.4 MeV	84
89	No phantom, x4 SSD4, 145.4 MeV	84
90	No phantom, y1 SSD1, 145.4 MeV	84
91	No phantom, y2 SSD2, 145.4 MeV	85
92	No phantom, y3 SSD3, 145.4 MeV	85

93	No phantom, y4 SSD4, 145.4 MeV	85
----	--	----

List of Tables

1	Isocentre, no flux reduction [48]	52
2	Isocentre at 252.7 MeV	52
3	Back Position at 252.7 MeV	52
4	Isocentre at 62.4 MeV	52
5	Back Position at 62.4 MeV	52
6	Particle flux reduction methods	53

List of Abbreviations

ART	Algebraic Reconstruction Technique
COSCAT	Coincidence Scaler and Trigger
CSDA	Continuous Slowing Down Approximation
CT	Computed Tomography
FIFO	First In First Out
FPGA	Field programmable gate array
FWHM	Full Width at Half Maximum
HDL	Hardware description language
HEPHY	Institut für Hochenergiephysik, Vienna
HEBT	High energy beam transfer
HU	Hounsfield Unit
IR1	Irradiation Room 1
LEBT	Low energy beam transfer
LHC	Large Hardron Collider
LINAC	Linear accelerator
MAPTA	MedAustron particle therapy acclerator
MEBT	Medium energy beam transfer
MCS	Multiple Coulomb scattering
MEB	Multi Event Buffer
MLP	Most Likeliest Path
NIM	Nuclear Instrument Standard
pCT	Proton Computed Tomography
PCTS	Particle counting and trigger system
PMT	Photomultiplier
SSD	Silicon Strip Detector
VHDL	Very High Speed Integrated Circuit Hardware Description Language
VME	Versa Module Europa-bus

References

- [1] MedAustron, Depth dose distribution of ion beams, <https://www.medaustron.at/de/ionentherapie>, date accessed: 2018-05-30 (2018).
- [2] H. Tsujii, T. Kamada, M. Baba, H. Tsuji, H. Kato, S. Kato, S. Yamada, S. Yasuda, T. Yanagi, H. Kato, R. Hara, N. Yamamoto, J. Mizoe, Clinical advantages of carbon-ion radiotherapy, *New Journal of Physics* 10, (2008). doi:10.1088/1367-2630/10/7/075009.
- [3] G. Poludniowski, N. M. Allinson, P. M. Evans, Proton radiography and tomography with application to proton therapy, *British Journal of Radiology* 88 (1053) (2015) 1–14. doi:10.1259/bjr.20150134.
- [4] D. C. Williams, The most likely path of an energetic charged particle through a uniform medium, *Physics in Medicine and Biology* 49 (13) (2004) 2899–2911. doi:10.1088/0031-9155/49/13/010.
- [5] C. Civinini, M. Scaringella, D. Bonanno, M. Brianzi, M. Carpinelli, G. A. Cirrone, G. Cuttone, D. Lo Presti, G. Maccioni, S. Pallotta, N. Randazzo, F. Romano, M. Rovituso, V. Sipala, C. Talamonti, F. Tommasino, E. Vanzi, M. Bruzzi, Proof-of-principle results of proton Computed Tomography, 2016 IEEE Nuclear Science Symposium, Medical Imaging Conference and Room-Temperature Semiconductor Detector Workshop, NSS/MIC/RTSD 2016 2017-Janua. doi:10.1109/NSSMIC.2016.8069620.
- [6] H. Kolanoski, N. Wermes, *Teilchendetektoren*, 1st Edition, Berlin, 2016, <http://link.springer.com/10.1007/978-3-662-45350-6>, date accessed: 2018-01-01. doi:10.1007/978-3-662-45350-6.
- [7] J. Berger, M.J., Coursey, J.S., Zucker, M.A., and Chang, ESTAR, PSTAR, and ASTAR: Computer Programs for Calculating Stopping-Power and Range Tables for Electrons, Protons, and Helium Ions (version 1.2.3), <http://physics.nist.gov/Star>, date accessed: 2017-10-01 (2017).
- [8] D. O. Robert Fosbinder, *Essentials of Radiologic Science*, Lippincott Williams & Wilkins(2011).
- [9] A. Schneider, Uwe, Pedroni, Eros, Lomax, The calibration of CT Hounsfield units for radiotherapy treatment planning, *Physics in medicine and biology* 41 (1) (1996) 111–124.
- [10] M. Yang, X. R. Zhu, P. C. Park, U. Titt, R. Mohan, G. Virshup, J. E. Clayton, L. Dong, Comprehensive analysis of proton range uncertainties related to patient stopping-power-ratio estimation using the stoichiometric calibration., *Physics in medicine and biology* 57 (13) (2012) 4095–1115, <http://www.ncbi.nlm.nih.gov/pubmed/22367888><http://www.pubmedcentral.nih.gov/articlerender.fcgi?artid=PMC3601187><http://www.ncbi.nlm.nih.gov/pubmed/22678123><http://www.pubmedcentral.nih.gov/articlerender.fcgi?artid=PMC3396587>, date accessed: 2018-02-01. arXiv:NIHMS150003, doi:10.1088/0031-9155/57/13/4095.

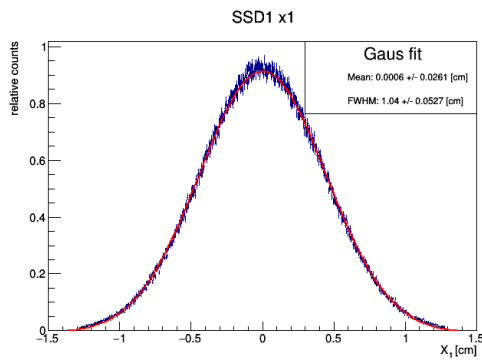
- [11] C. Civinini, D. Bonanno, M. Brianzi, M. Carpinelli, G. A. Cirrone, G. Cuttone, D. L. Presti, G. Maccioni, S. Pallotta, N. Randazzo, M. Scaringella, F. Romano, V. Sipala, C. Talamonti, E. Vanzi, M. Bruzzi, Proton Computed Tomography: Iterative image reconstruction and dose evaluation, in: *Journal of Instrumentation*, Vol. 12, 2017. doi:10.1088/1748-0221/12/01/C01034.
- [12] PSTAR database, <https://physics.nist.gov/PhysRefData/Star/Text/PSTAR.html>, date accessed: 2018-02-01.
- [13] G. T. Herman, *Fundamentals of Computerized Tomography*, Springer, 2009.
- [14] W. Leo, *Techniques for Nuclear and Particle Physics Experiments*, 1990, <http://link.springer.com/10.1007/978-3-642-57920-2>, date accessed: 2018-01-01. arXiv:arXiv:1011.1669v3, doi:10.1007/978-3-642-57920-2.
- [15] E. Keil, E. Zeitler, W. Zinn, Zur einfach- und mehrfachstreuung geladener teilchen, *Zeitschrift fur Naturforschung - Section A Journal of Physical Sciences* 15 (12) (1960) 1031–1038. doi:10.1515/zna-1960-1202.
- [16] G. Moliere, Theory of the scattering of fast charged particles. 2. Repeated and multiple scattering, *Z. Naturforsch. A3* (1948) 78–97.
- [17] V. L. Highland, Some practical remarks on multiple scattering, *Nuclear Instruments and Methods* 129 (2) (1975) 497–499. doi:10.1016/0029-554X(75)90743-0.
- [18] H. W. Lewis, Multiple scattering in an infinite medium, *Physical Review* 78 (5) (1950) 526–529. doi:10.1103/PhysRev.78.526.
- [19] S. Agostinelli, J. Allison, K. Amako, J. Apostolakis, H. Araujo, P. Arce, M. Asai, D. Axen, S. Banerjee, G. Barrand, F. Behner, L. Bellagamba, J. Boudreau, L. Broglia, A. Brunengo, H. Burkhardt, S. Chauvie, J. Chuma, R. Chytracsek, G. Cooperman, G. Cosmo, P. Degtyarenko, A. Dell’Acqua, G. Depaola, D. Dietrich, R. Enami, A. Feliciello, C. Ferguson, H. Fesefeldt, G. Folger, F. Foppiano, A. Forti, S. Garelli, S. Giani, R. Giannitrapani, D. Gibin, J. J. Gomez Cadenas, I. Gonzalez, G. Gracia Abril, G. Greeniaus, W. Greiner, V. Grichine, A. Grossheim, S. Guatelli, P. Gumplinger, R. Hamatsu, K. Hashimoto, H. Hasui, A. Heikkinen, A. Howard, V. Ivanchenko, A. Johnson, F. W. Jones, J. Kallenbach, N. Kanaya, M. Kawabata, Y. Kawabata, M. Kawaguti, S. Kelner, P. Kent, A. Kimura, T. Kodama, R. Kokoulin, M. Kossov, H. Kurashige, E. Lamanna, T. Lampen, V. Lara, V. Lefebure, F. Lei, M. Liendl, W. Lockman, F. Longo, S. Magni, M. Maire, E. Medernach, K. Minamimoto, P. Mora de Freitas, Y. Morita, K. Murakami, M. Nagamatu, R. Nartallo, P. Nieminen, T. Nishimura, K. Ohtsubo, M. Okamura, S. O’Neale, Y. Oohata, K. Paech, J. Perl, A. Pfeiffer, M. G. Pia, F. Ranjard, A. Rybin, S. Sadilov, E. di Salvo, G. Santin, T. Sasaki, N. Savvas, Y. Sawada, S. Scherer, S. Sei, V. Sirotenko, D. Smith, N. Starkov, H. Stoecker, J. Sulkimo, M. Takahata, S. Tanaka, E. Tcherniaev, E. Safai Tehrani, M. Tropeano, P. Truscott, H. Uno, L. Urban, P. Urban, M. Verderi, A. Walkden, W. Wander, H. Weber, J. P. Wellisch, T. Wenaus, D. C. Williams, D. Wright, T. Yamada, H. Yoshida, D. Zschesche, GEANT4 - A simulation toolkit, *Nuclear Instruments and Methods in Physics Research, Section A: Accelerators, Spectrometers, Detectors and Associated Equipment* 506 (3) (2003) 250–303. arXiv:1005.0727v1, doi:10.1016/S0168-9002(03)01368-8.

- [20] B. Grupen, Claus, Shwartz, Particle Detectors, Cambridge University Press, 2008.
- [21] T. Bergauer, Halbleiterdetektoren, <http://www.hephy.at/bildung/studierendelehre/unterlagen/multicontent/teilchendetektoren-bergauer/>, date accessed: 2017-12-01 (2017).
- [22] L. Carter, Cashwell. E. D., Particle-transport simulation with the Monte Carlo method, Tech. rep. (1975). doi:10.2172/4167844.
- [23] M. Benedikt, A. Wrulich, Medaustron-project overview and status, European Physical Journal Plus 126 (7) (2011) 1–11. doi:10.1140/epjp/i2011-11069-9.
- [24] F. Osmic, M. Feurstein, A. Gyorgy, A. Kerschbaum, M. Repovz, S. Schwarz, E. B. G. Medaustron, G. Burtin, Overview of the Beam Diagnostics in the Medaustron Accelerator : Design Choices and Test Beam Commissioning, in: MOPPR002, 2012, pp. 774–776.
- [25] R. J. Steinhagen, Tune and chromaticity diagnostics, CAS - CERN Accelerator School: Course on Beam Diagnostics (2009) 317 <http://cds.cern.ch/record/1213281>, date accessed: 2018-02-01. doi:10.5170/CERN-2009-005.317.
- [26] A. De Franco, C. Schmitzer, Particle flux reduction methods for non-clinical research provided by MedAustron, private communication (2017).
- [27] J. Borburgh, T. Fowler, A. Prost, T. Kramer, T. Stadlbauer, DESIGN OF ELECTROSTATIC SEPTA AND FAST DEFLECTOR FOR MEDAUSTRON, in: THPS048, 2011, pp. 3532–3534.
- [28] L. Badano, S. Rossi, Characteristics of a betatron core for extraction in a proton-ion medical synchrotron.
- [29] A. Biere, D. Kroening, G. Weissenbacher, C. M. Wintersteiger, Digitaltechnik — Eine praxisnahe Einführung, 2008, <http://www.springerlink.com/index/10.1007/978-3-540-77729-8> <http://link.springer.com/10.1007/978-3-540-77729-8>, date accessed: 2017-12-01. arXiv:arXiv:1011.1669v3, doi:10.1007/978-3-540-77729-8.
- [30] W. Gehrke Marco Winzker Klaus Urbanski Roland Voitowitz Grundlagen, Digitaltechnik, 7th Edition, Berlin, 2016.
- [31] A. Burker, COSCAT_GUI, private communications (2017).
- [32] E. Technology, FAST TIMING EJ-228, EJ-230, <http://www.eljentechnology.com/products/plastic-scintillators/ej-228-ej-230>, date accessed: 2017-12-01 (2017).
- [33] HAMATSU, HAMATSU photosensor module H10721-210, <https://www.hamamatsu.com/us/en/product/alpha/C/3044/H10721-210/index.html>, date accessed: 2017-12-01 (2017).
- [34] CAEN, <http://www.caen.it/jsp/Template2/HomePage.jsp>, date accessed: 2018-01-01.
- [35] ModelSim, https://www.mentor.com/company/higher_ed/modelsim-student-edition, date accessed: 2017-08-01.

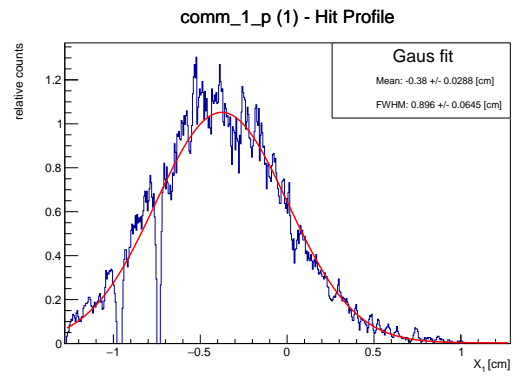
- [36] U.S Department of Energy, Standard NIM Instrumentation System, Tech. rep. (1990).
- [37] R. Brun, F. Rademakers, ROOT - An Object Oriented Data Analysis Framework, in: AIHENP'96 Workshop, Nucl. Inst. & Meth. in Phys., 1997, pp. 81–86, <https://root.cern.ch/>, date accessed: 2017-12-01.
- [38] A. Burkner, private communications (2017).
- [39] PTW Freiburg, Manual: OCTAVIUS Detector 729 XDR (T10042) and Detector Interface 4000 (T16039 from SN1000) (2014).
- [40] A. Hofer, DIPLOMARBEIT Dose distribution measurements with Octavius 729, Master's thesis, TU Wien (2018).
- [41] P. Paulitsch, Performance Studies of Silicon Strip Sensors for the Phase-II Upgrade of the CMS Tracker, Master's thesis, TU Wien (2018).
- [42] C. Irmeler, Upgrade Studies for the Belle Silicon Vertex Detector, Diploma Thesis (9126972).
- [43] M. Valentan, The Silicon Vertex Detector for b-tagging at Belle II, Ph.D. thesis, TU Wien (2013).
- [44] Raspberry Pi Foundation, Raspberry Pi 3 Model B+, <https://www.raspberrypi.org/products/raspberry-pi-3-model-b-plus/>, date accessed: 2018-01-01.
- [45] W. H. Press, S. A. Teukolsky, W. T. Vetterling, B. P. Flannery, Numerical Recipes 3rd Edition: The Art of Scientific Computing, Cambridge University Press, New York, 2007.
- [46] S. Teukolsky, W. Press, Numerical Recipes, Cambridge University Press, 1986.
- [47] Geant4Collaboration, GEANT4.10.4: Physics Reference Manual (2017) 1–434 <http://geant4.web.cern.ch/geant4/UserDocumentation/UsersGuides/PhysicsReferenceManual/fo/PhysicsReferenceManual.pdf>, date accessed: 2017-12-12.
- [48] MedAustron, internal report, Tech. rep. (2017).
- [49] G. E. P. Box, M. E. Muller, A Note on the Generation of Random Normal Deviates, Ann. Math. Statist. 29 (1958) 610–611.
- [50] LEGO, LEGO, <https://www.lego.com/en-us/>, date accessed: 2018-04-01 (2018).

Beam telescope measurements

LEGO brick, 145.4 MeV

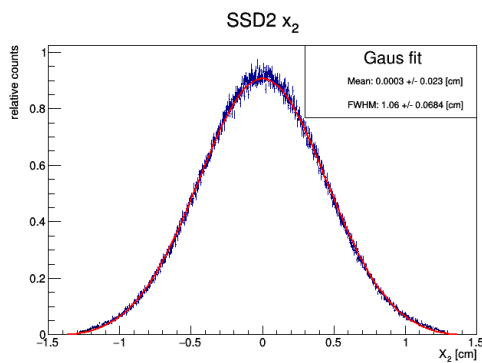


(a) Geant4 simulation

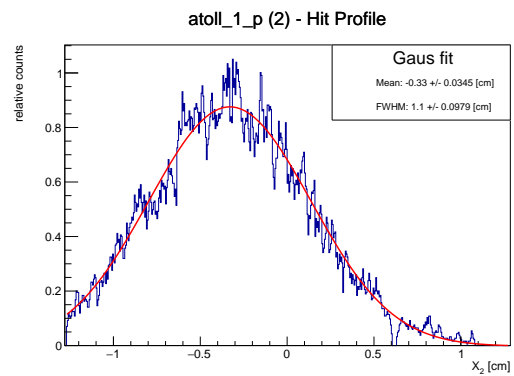


(b) Measurement

Figure 70: LEGO brick, x1 SSD1, 145.4 MeV

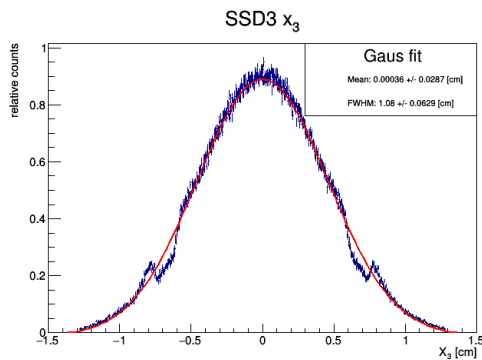


(a) Geant4 simulation

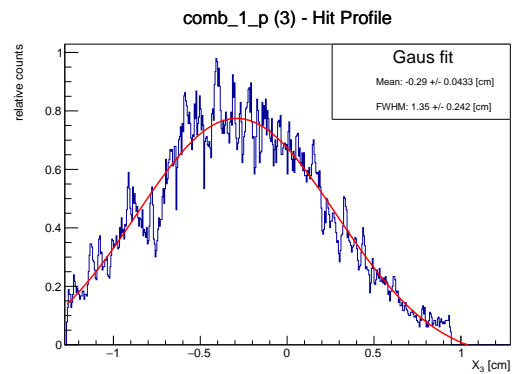


(b) Measurement

Figure 71: LEGO brick, x2 SSD2, 145.4 MeV

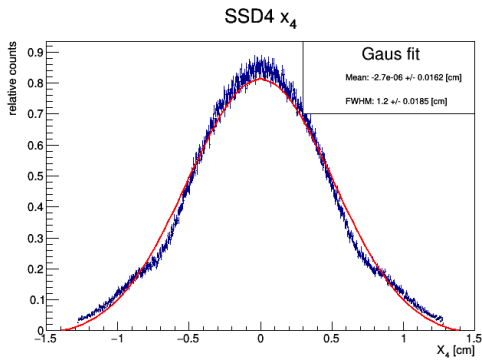


(a) Geant4 simulation

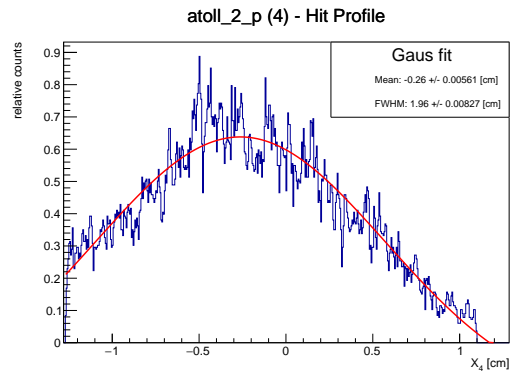


(b) Measurement

Figure 72: LEGO brick, x3 SSD3, 145.4 MeV

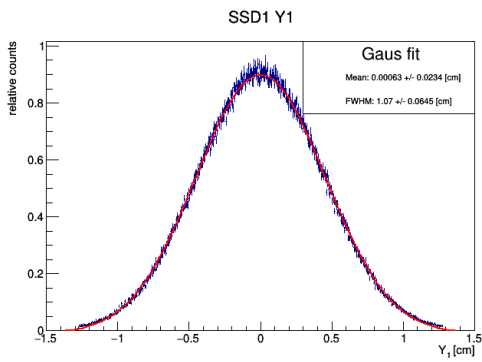


(a) Geant4 simulation

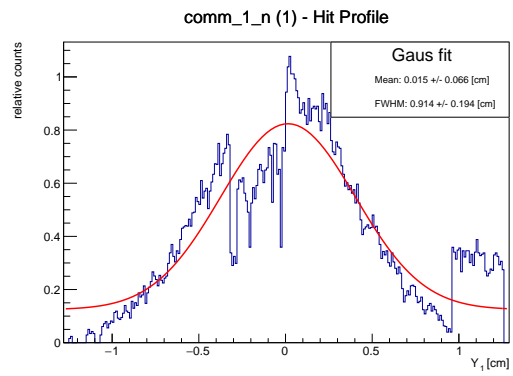


(b) Measurement

Figure 73: LEGO brick, x4 SSD4, 145.4 MeV

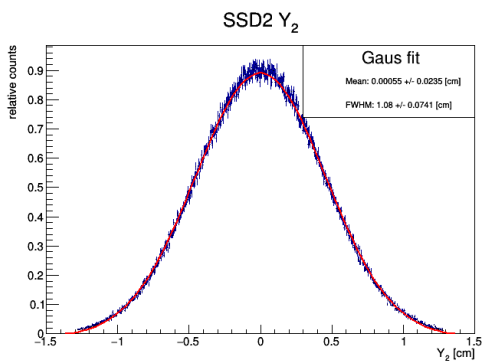


(a) Geant4 simulation

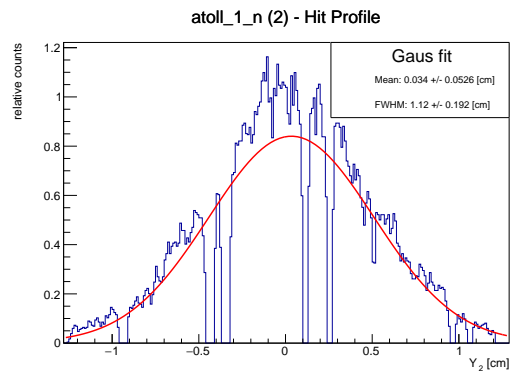


(b) Measurement

Figure 74: LEGO brick, y1 SSD1, 145.4 MeV

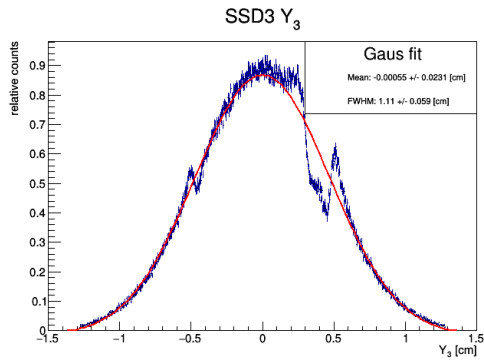


(a) Geant4 simulation

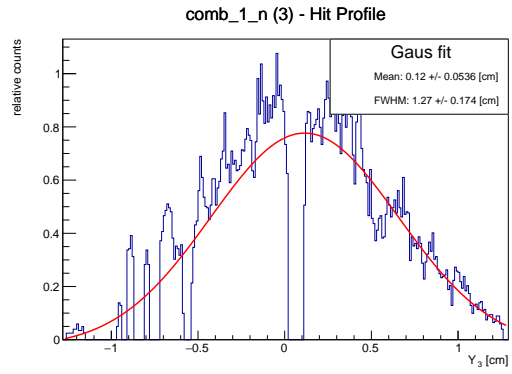


(b) Measurement

Figure 75: LEGO brick, y2 SSD2, 145.4 MeV

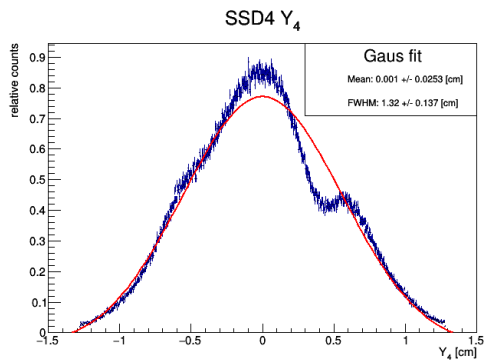


(a) Geant4 simulation

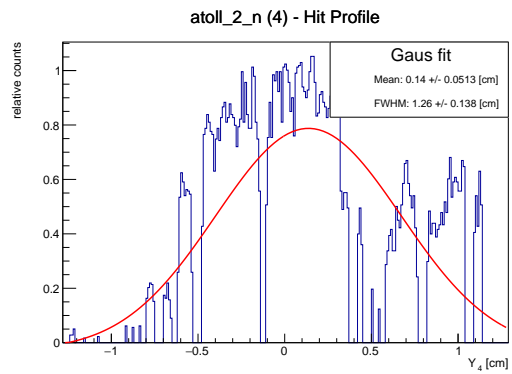


(b) Measurement

Figure 76: LEGO brick, y3 SSD3, 145.4 MeV



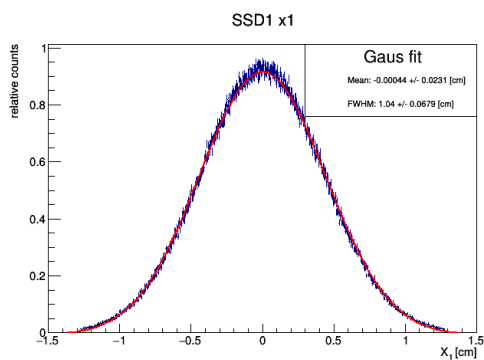
(a) Geant4 simulation



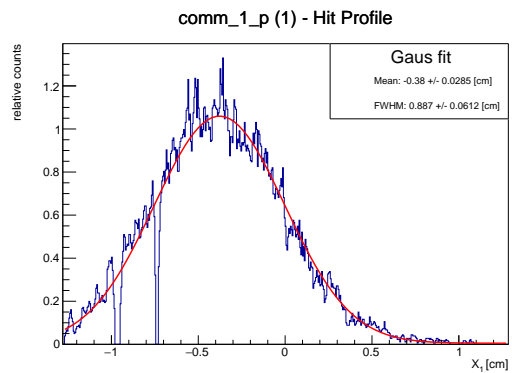
(b) Measurement

Figure 77: LEGO brick, y4 SSD4, 145.4 MeV

PhanDuc, 145.4 MeV

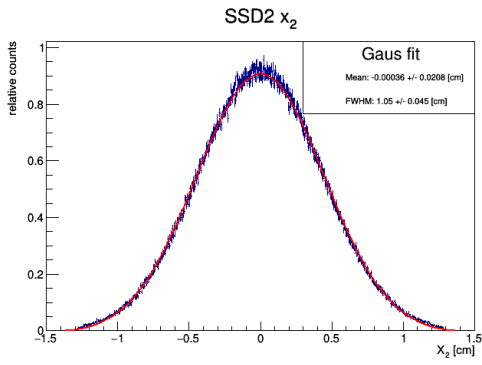


(a) Geant4 simulation

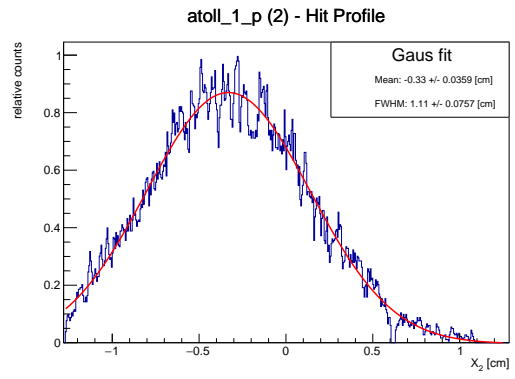


(b) Measurement

Figure 78: PhanDuc, x1 SSD1, 145.4 MeV

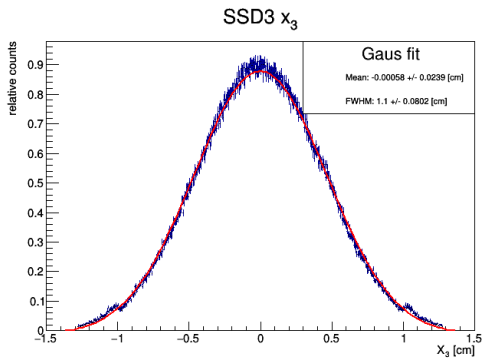


(a) Geant4 simulation

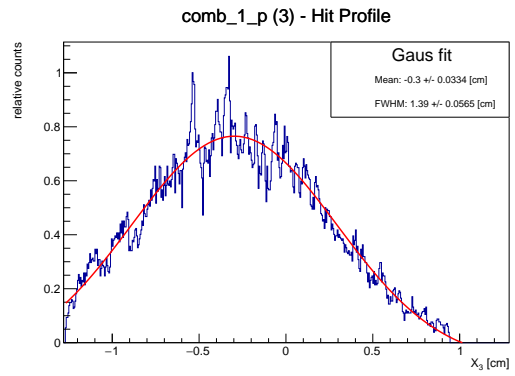


(b) Measurement

Figure 79: PhanDuc, x2 SSD2, 145.4 MeV

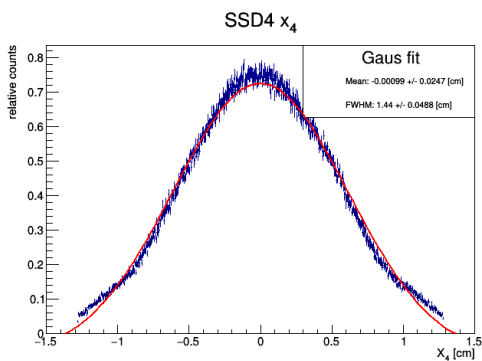


(a) Geant4 simulation

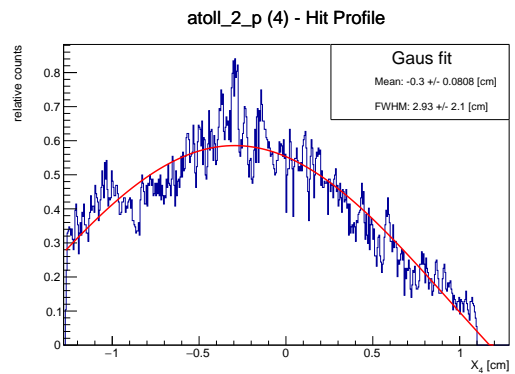


(b) Measurement

Figure 80: PhanDuc, x3 SSD3, 145.4 MeV

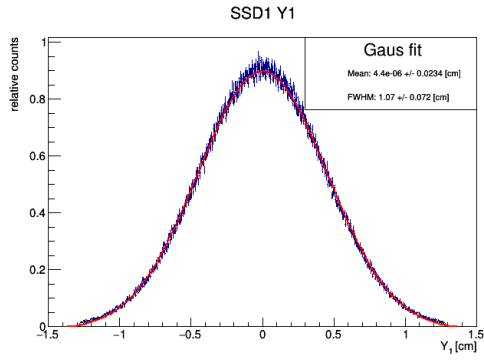


(a) Geant4 simulation

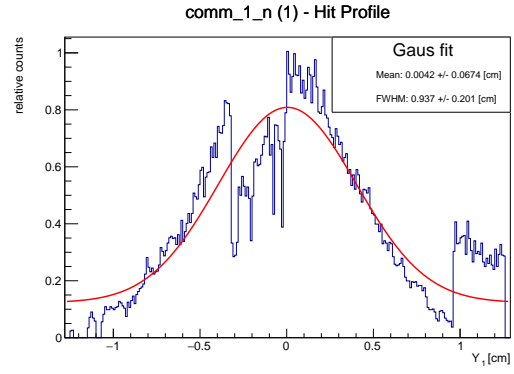


(b) Measurement

Figure 81: PhanDuc, x4 SSD4, 145.4 MeV

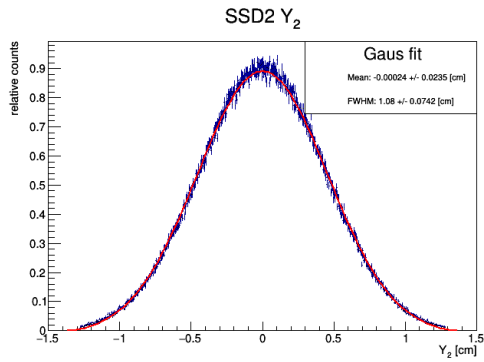


(a) Geant4 simulation

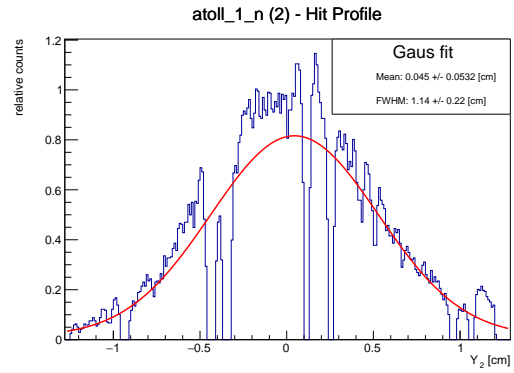


(b) Measurement

Figure 82: PhanDuc, y1 SSD1, 145.4 MeV

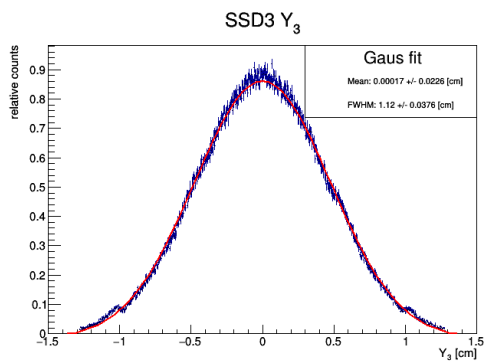


(a) Geant4 simulation

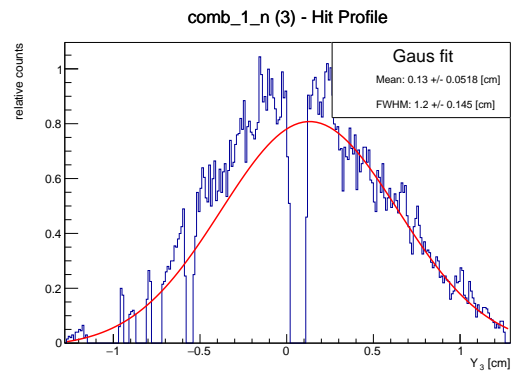


(b) Measurement

Figure 83: PhanDuc, y2 SSD2, 145.4 MeV

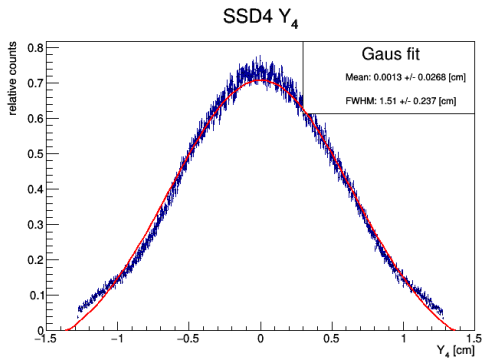


(a) Geant4 simulation

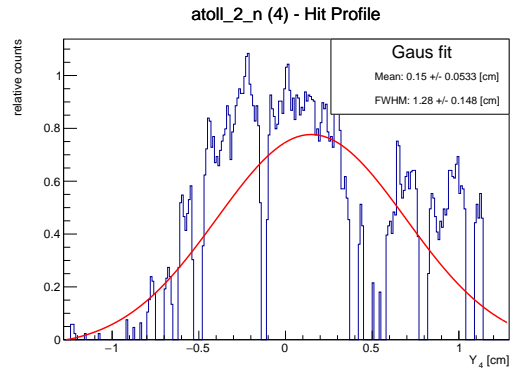


(b) Measurement

Figure 84: PhanDuc, y3 SSD3, 145.4 MeV



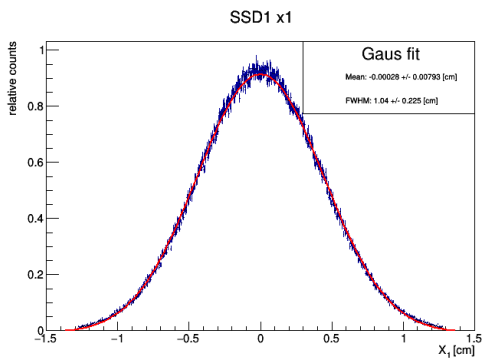
(a) Geant4 simulation



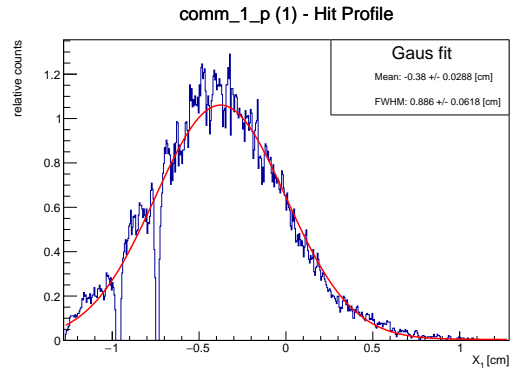
(b) Measurement

Figure 85: PhanDuc, y4 SSD4, 145.4 MeV

no phantom, 145.4 MeV

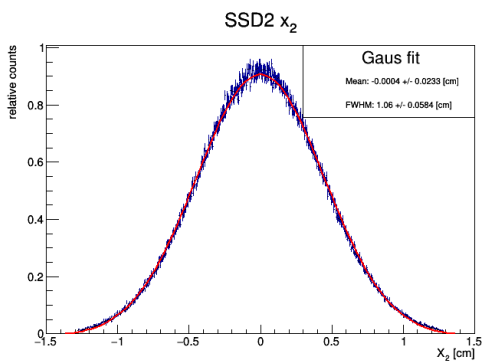


(a) Geant4 simulation

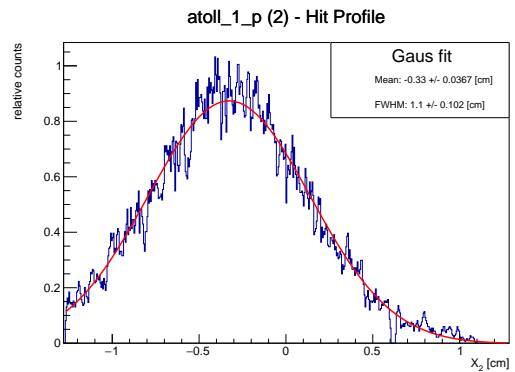


(b) Measurement

Figure 86: No phantom, x1 SSD1, 145.4 MeV

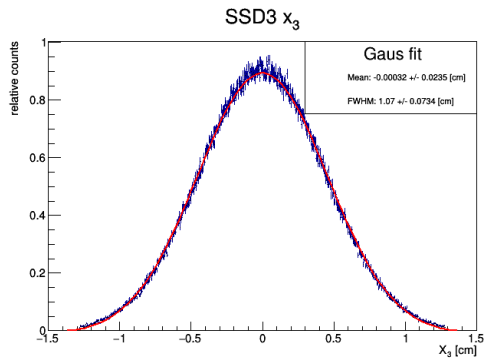


(a) Geant4 simulation

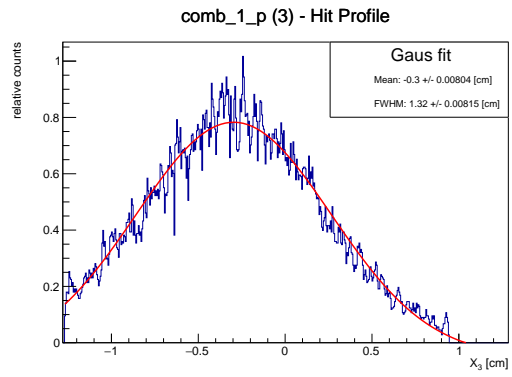


(b) Measurement

Figure 87: No phantom, x2 SSD2, 145.4 MeV

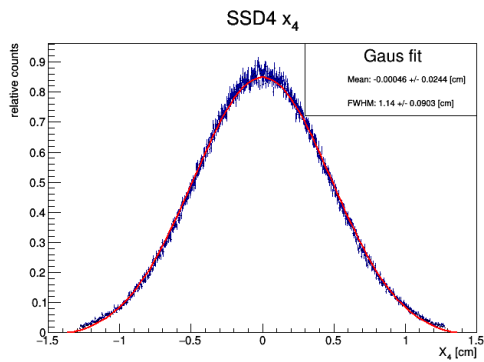


(a) Geant4 simulation

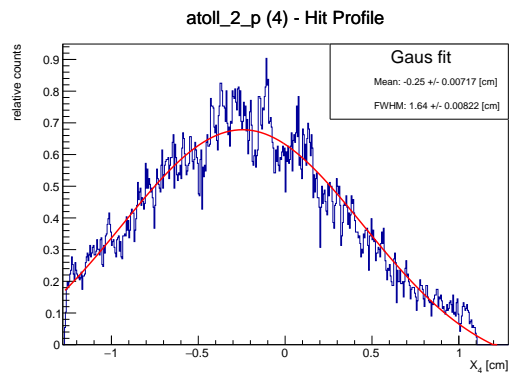


(b) Measurement

Figure 88: No phantom, x3 SSD3, 145.4 MeV

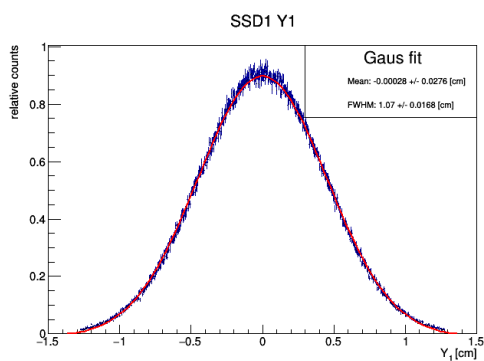


(a) Geant4 simulation

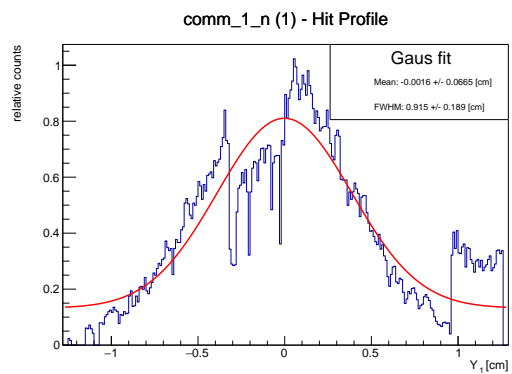


(b) Measurement

Figure 89: No phantom, x4 SSD4, 145.4 MeV

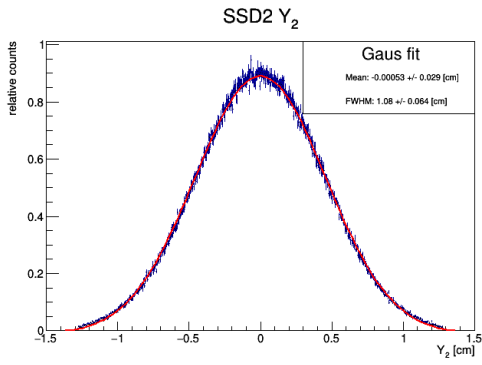


(a) Geant4 simulation

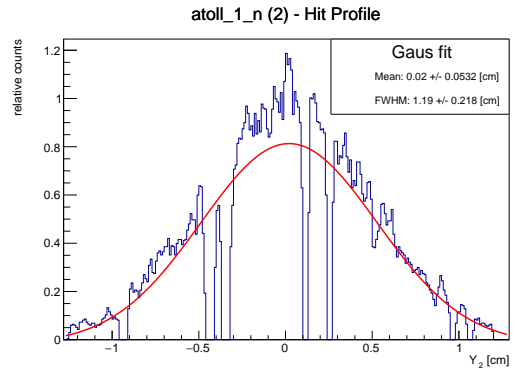


(b) Measurement

Figure 90: No phantom, y1 SSD1, 145.4 MeV

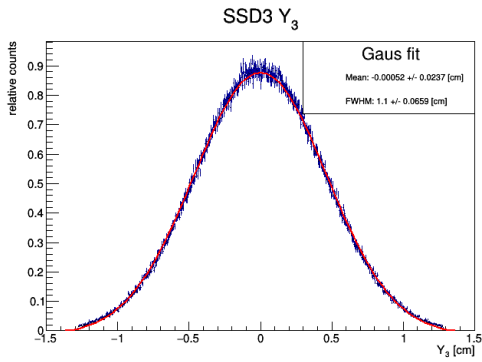


(a) Geant4 simulation

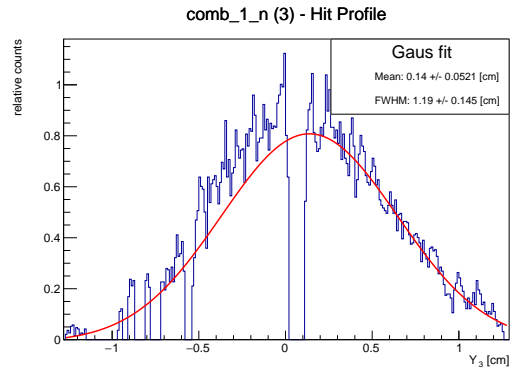


(b) Measurement

Figure 91: No phantom, y2 SSD2, 145.4 MeV

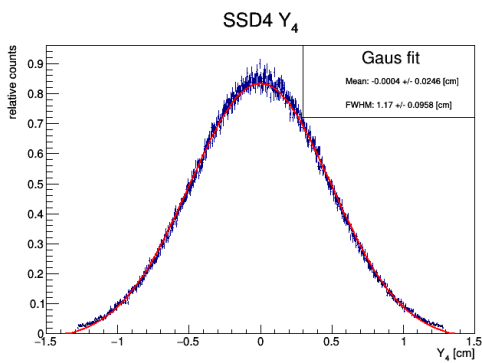


(a) Geant4 simulation

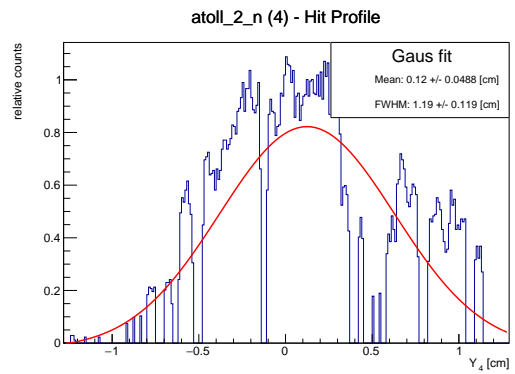


(b) Measurement

Figure 92: No phantom, y3 SSD3, 145.4 MeV



(a) Geant4 simulation



(b) Measurement

Figure 93: No phantom, y4 SSD4, 145.4 MeV